Implementing of a Variable Geometry Burner Testrig

Roman Proebster

Institute for Thermal Turbomachinery and Machine Dynamics

Supervisor 1: Thomas Leitgeb

Supervisor 2: Fabrice Giuliani

June 2011

Acknowledgements

Die vorliegende Diplomarbeit wurde am Institut für Thermische Turbomaschinen und Maschinendynamik an der Technischen Universität Graz im Rahmen des EU-Projektes NEWAC (New Aero Engine Core Concepts) durchgeführt.

Herrn Univ.-Prof. Dr.-Ing. Franz Heitmeir möchte ich dafür danken, dass er es mir ermöglichte am Institut für Thermische Turbomaschinen und Maschinendynamik diese Diplomarbeit zu verfassen.

Herrn Univ.-Doz. Dr. Fabrice Giuliani möchte ich für die Einbindung in die Verbrennungsabteilung und für die Unterstützung während der Arbeit danken.

Herrn Ao. Univ.-Prof. Dipl.-Ing. Dr. techn. Jakob Woisetschläger möchte ich ganz herzlich danken für die Wissensvermittlung und Unterstützung in der optischen Messtechnik und zudem für die Hilfe während der gesamten Arbeit.

Ganz besonderen Dank möchte ich meinem Betreuer Dipl.-Ing. Thomas Leitgeb widmen der stets mit Rat und Tat zur Seite stand und von dessen umfassenden Ingenieurswissen ich viel lernen konnte.

Dem gesamten Team des Instituts möchte ich einen herzlichen Dank äußern für die Zeit die ich mit Ihnen am Institut verbringen durfte.

Vor allem aber möchte ich meiner Unterstützung aus der Heimat danken, meinen Eltern und meiner ganzen Familie, die mir den nötigen Rückhalt während des gesamten Studiums gegeben haben.

Roman Proebster

Abstract

A variable geometry burner concept was investigated at the Institute for Thermal Turbomachinery and Machine Dynamics at Graz University of Technology within the research project New Aero Engine Core Concepts (NEWAC). The aim was to enlarge the operational envelope of a 10 kW model combustor by altering swirl strength and exit nozzle area as new low-emission concepts of gas turbines drastically reduce the core mass flow, which has a direct impact on the flow field within the combustor and may lead to flame transition, flashback or flame extinction. Therefore, in the present thesis, a modular burner test rig was established for extensive investigations under atmospheric conditions, mainly employing optical measurement techniques such as Schlieren visualization, light emission measurements, differential interferometry, and Particle Image Velocimetry (PIV). The corresponding measurement fundamentals and the respective test setup are described in detail. The data acquisition was programmed in LabVIEW 8.6 to ensure the operating conditions for the measurement points together with an adequate measurement storage.

Kurzfassung

Am Institut für Thermische Turbomaschinen und Maschinendynamik wurde im Rahmen des europäischen Forschungsprogramms New Aero Engine Core Concepts (NEWAC) ein neuer Ansatz einer variablen Brennergeometrie untersucht. Zielsetzung dabei war die Betriebsbereichserweiterung eines 10 kW Modellbrenners durch Veränderung der Drallstärke am Austritt aus der Düse und des Düsenquerschnitts selbst. Dies ist notwendig geworden, da neue Niedrigemissionskonzepte von Gasturbinen einen drastisch reduzierten Kernmassenstrom durch den Brenner während des Betriebes bedingen. Diese Reduktion hat einen direkten Einfluss auf die Strömung innerhalb der Brennkammer, welche mit Flammentransition, Flammenrückschlag oder dem Erlöschen der Flamme verbunden ist. Ziel dieser Arbeit war es, einen möglichst modularen Prüfstand für umfangreiche Untersuchungen, wie Schlieren Visualisierung, Messung der natürlichen Intensität der Flamme, Differentialinterferometrie und Particle Image Velocimetry (PIV), zur Verfügung zu stellen. Die Aufbauten für die einzelnen Messmethoden und die zugrunde liegende Theorie werden im Detail beschrieben. Um die Betriebsbedingungen für die zu untersuchenden Betriebspunkte zu gewährleisten wurde ein Datenerfassungsprogramm in LabVIEW 8.6 geschrieben, das es erlaubte die erhaltenen Daten in geeigneter Weise abzulegen.

Statutory Declaration

I declare that I have authored this thesis independently, that I have not used other than the declared sources / resources, and that I have explicitly marked all material which has been quoted either literally or by content from the used sources.

Place	Date	Signature

Eidesstattliche Erklärung

Ich erkläre an Eides statt, dass ich die vorliegende Arbeit selbstständig verfasst, andere als die angegebenen Quellen/Hilfsmittel nicht benutzt, und die den benutzten Quellen wörtlich und inhaltlich entnommene Stellen als solche kenntlich gemacht habe.

Ort	Datum	Unterschrift

Contents

Chapter 1

Introduction

1.1 Newac

In todays society resource efficiency and environmental issues are paramount. In this direction the european Advisory Council of Aeronautic Research in Europe (ACARE) has set demanding goals for air traffic concerning less fuel consumption and the reduction of emissions of gas turbines. In view of these targets the integrated project Newac, funded by the european commission, was started in May 2006 by 40 partners active in engine manufactoring, universities, and research centers. NEWAC stands for New Aero Engine Core Concepts.

Following former projects Newac has tackled the task, beside fuel consumption reduction, to reduce CO_2 emissions by 6% (Fig. 1.1) and NO_x emissions by 16% (Fig. 1.2) for aero engines. Four extensive conceptional studies were initiated. The four concepts for gasturbines are shown in Fig. 1.3.

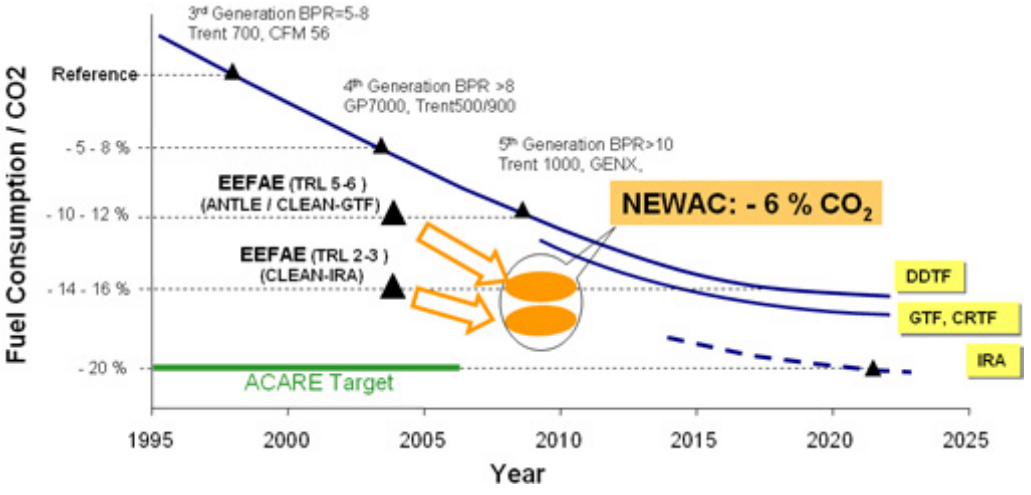

Figure 1.1: Target of the project NEWAC for CO_2 reduction [1]

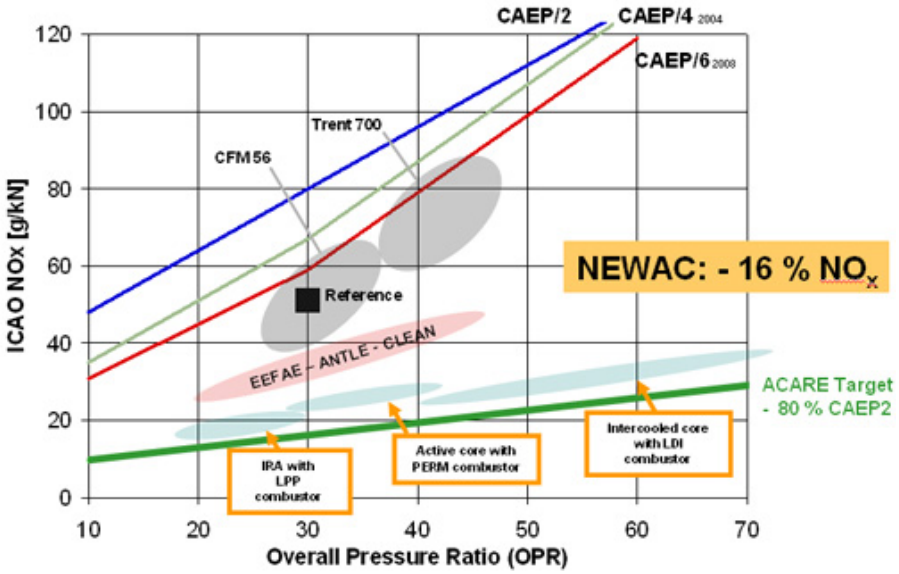

Figure 1.2: Target of the project NEWAC for NO_x reduction [1]

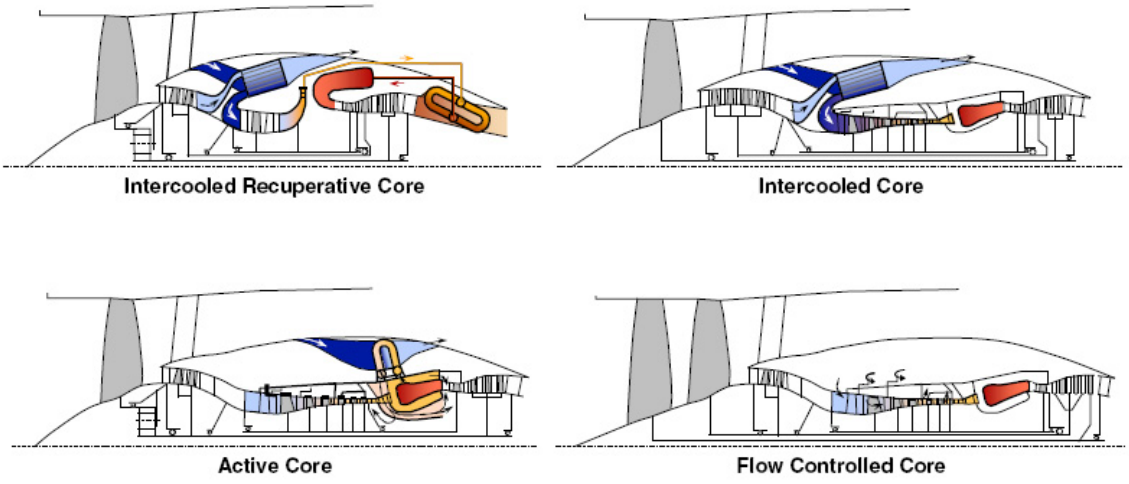

Figure 1.3: Core concepts in the project NEWAC [1]

The four concepts are:

1. **Intercooled Recuperative Core**
2. **Intercooled Core**
3. **Active Core**
4. **Flow Controlled Core**

Intercooled Recuperative Core feeds the energy of the jet blast back to the core. A heat exchanger, placed between the compressor modules, improves the efficiency, which leads to a convenient overall pressure ratio (OPR) of 20:1 to 25:1. This justifies the insertion of a radial compressor, which delivers the

required pressure for the Lean Premixed Prevaporisation (LP(P)) module of the combustion chamber. A LPP module consists of an injection system for air blast followed by a premixing tube where the injected kerosine is mixed and diffused with the entrainment air.

Intercooled Core Concept is employing the technique of cooling the air between the compressor modules with a heat exchanger. In this case a lean direct injection (LDI) module combustion chamber technique is used. In the LDI modules the fuel is directly injected. The fuel supply is controlled through a pilot flame, for stability, and low NO_x emissions of the main stage. This core concept features, in comparison with the Intercooled Recuperative Core, a higher OPR from 30:1 to over 50:1.

Active Core propulsion is adjusted in order to obtain an optimal operation of the entire engine in all ranges. The cooling air of the combustion chamber is additionally cooled down. In this way less air supply from the high pressure compressor is needed. For the combustion chamber, beside the LDI injection system, the partial evaporation rapid mixing (PERM) is considered as a variant. Swirl atomizer vaporize the fuel partially and achieve rapid mixing with air. This type of module is able to obtain OPR from 20:1 to 35:1.

Flow Controlled Core concept is employing elements like the contra rotating turbofan, the active regulation against pumping through airblast. Similar to the concept of the active core the LDI and the PERM injection systems were named according to the technique for combustion chamber.

A summary of the concepts of the used injection systems in the combustion chambers are shown in Fig. 1.4.

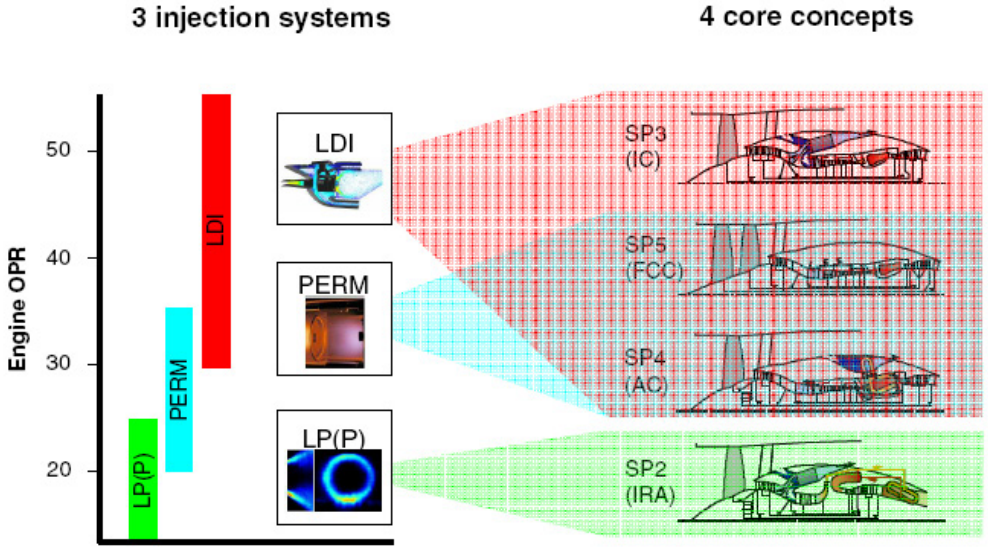

Figure 1.4: Innovative combustor technologies applications from project NEWAC (SP_x, IC,FCC,AC, and IRA are organisational nomenclatures of project NEWAC) [1]

To verify these new and innovative concepts new studies had to be investigated in detail (Fig. 1.5). Within these series of studies the investigation of the variable geometry burner, including variable swirler, is a research project of the Institute for Thermal Turbomachinery and Machine Dynamics at Graz University of Technology. For this project implementing a test rig and investigating appropriate test methods was the topic of this work.

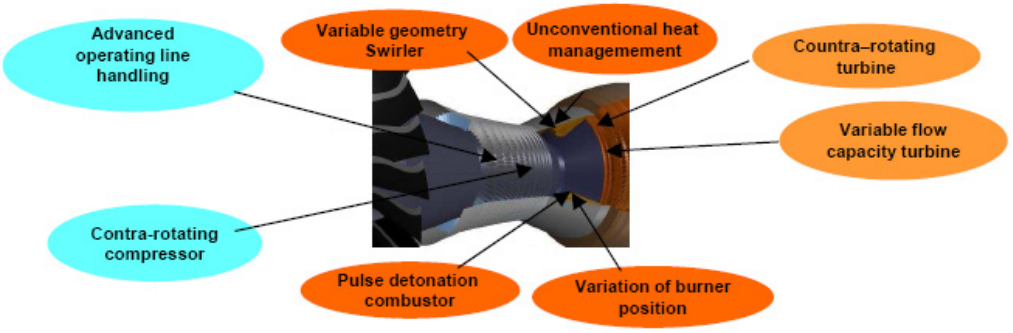

Figure 1.5: Future innovative core configurations from project NEWAC [2]

1.2 Objectives

The new concept of a variable geometry burner, which addresses low-emission concepts for gas turbines with drastically reduced core mass flow in the lower power operational range, is realized in the research project NEWAC at the Institute for Thermal Turbomachinery and Machine Dynamics at Graz University of Technology (T.Leitgeb [3]). To verify this new concept extensive testing of a model burner implemented within this project needs to be accomplished. Thereby, the target of this work consists in establishing a modular test rig together with a set of measurement sequences to characterize this new variable geometry burner. The test rig needs to adapt the variable geometry burner with appropriate operational fixtures to corresponding measurement instrumentation for determination of performance and according parameter setting. Important parameters are the essential figure of core mass flow and injection area together with swirl angle , adjustable as a function of operation points. These parameters require appropriate setting and control. For the measurements a flame tube environment for the burner needs to be provided to achieve combustion confinement. Non intrusive optical measurements shall be employed like Schlieren visualization for characterization of density gradients in the combustion zone, differential interferometry to determine absolute values for local density distribution, intensity measurement for the identification of flame shapes as well as two dimensional and three component Particle Image Velocity (PIV) measurements to detect the velocity fields in the combustion zone. A data acquisition was additionally programmed in LabVIEW 8.6 to ensure the operating conditions for the measurement points together with an adequate measurement storage.

Chapter 2

Variable geometry

Conventional burner design for gas turbines provides a compromise for the operational range between idle power and full power considering requirements concerning air mass flow and the adjustment of the flame to achieve a high efficiency. The operating range of a conventional combustor allows only a variation of a few hundred degrees Kelvin of flame temperature for a sustained stable combustion. Thereby, the corresponding range for fuel/air ratio is of around 1.4 to 1 [4]. In contrast to this, a combustor with variable geometry parameters provides an approach for an extended lean combustion range. Main influence parameters for the variable geometry burner are the swirl and the variable exit area, which are explained in the following. Furthermore, a literature research may provide an insight to available variable geometry concepts.

2.1 Parameters

2.1.1 Swirl

A swirl stabilized flame is a common concept for a combustor. The features are reduction of combustor length because of higher rate (degree) of entrainment, improvement of flame stability because of the inner recirculation zone that recirculates hot combustion products, impingement of the flame on the boundary surfaces is minimized, Giuliani [5]. Swirl can be generated mainly by three methods. These are tangential inlet slots (radial swirler), guided vanes (axial swirler) and direct rotation(co- or contra rotative). These can be seen in Fig. 2.1.

Fig. 2.2 shows a typical velocity profile of the injection zone activated by a swirler. The recirculation zone with typical circulating velocity characteristics, around the center axis stabilizes the flame in axial position.

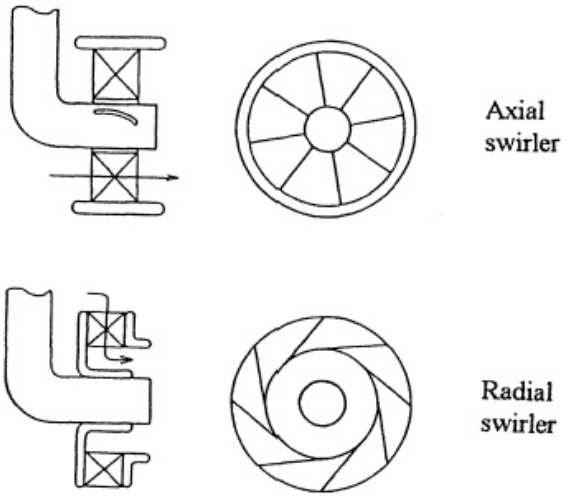

Figure 2.1: Axial swirler (above) and radial swirler (below) [4]

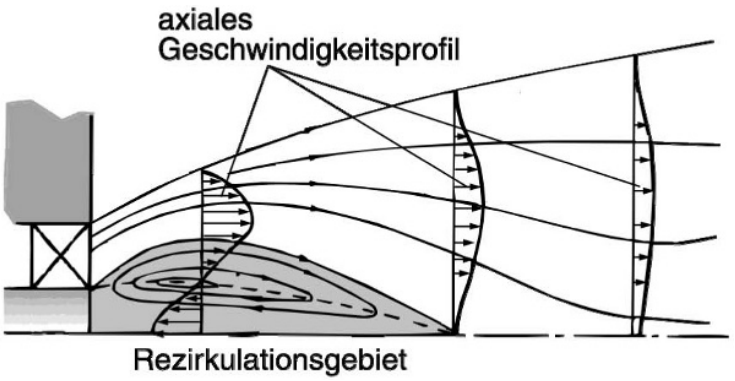

Figure 2.2: Typical profiles of axial- and swirl- velocity components in a strongly swirling flow [6]

Classification parameter of a swirler is the swirl number S (by Beer and Chigier [4]). It is defined as the ratio between the tangential and the axial mass flow under atmospheric conditions (terms related to the static pressure are neglected). Further description of the swirl number S is given in [4].

A weak swirl number is representative of an axial jet (S<0,6) whereas a strong swirl number (S>0,6) is representative of a radial swirled jet, where the flow is centrifuged along the walls of the chamber. S=0,6 is a good compromise regarding the generation of a centrical recirculation zone (Fig. 2.3) and acceptable flame position in relation to the walls [5].

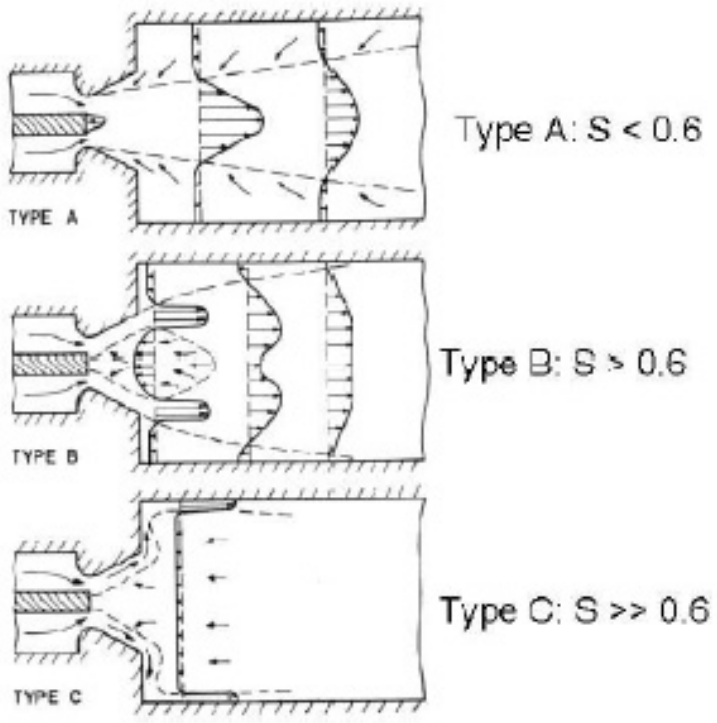

Figure 2.3: Characterization of the swirl strength with the help of the swirl number S [5]

2.1.2 Variable exit area

Variable nozzle area can be realized through orifices or through an obstacle which blocks the exit. An example is shown in Fig. 2.4. By decreasing the exit area for lower mass flow the flow velocity can be increased which stabilizes the lifting of the flame.

2.2 Literature research

Already in the 1970's a number of patents existed including a variable geometry concept for a gas turbine combustion chamber. The aim was to reduce the emissions through an efficient combustion by an appropriate adjustment of mechanic parameters depending on operating conditions, improving efficiency, and thereby reducing fuel consumption. Interest in this concept of variable geometry arose again recently as can be seen by new patents which were submitted on this topic in the last years.

2.2.1 Variable geometry air swirler with axial positioning

The patent from ALSTOM invented by Dittmann et al. in 2000 provides the air swirler (Fig. 2.4) with a moveable rod, positioned in coaxial arrangement at the entry slots to the burner for varying the annular gap to adjust the exit air velocity in order to optimize the swirl of the flame. The outer bushing body of the burner and inner flow entity are arranged in such manner that they can be rotated and/or axially displaced against each other.

The fuel is injected into the primary chamber, to the combined axial and tangential air flow. Other concepts, like the burner studied at Institute for Thermal Turbomachinery and Machine Dynamics at Graz University of Technology (Thomas Leitgeb [3]), use the approach where the fuel is mixed with the tangential air in a separate chamber before merging with the axial air.

Further information of the patent is given in Ref. [7]. Other patents which address an axially movable arrangement are US 5664412 [8] and EP 1524469A1 [9].

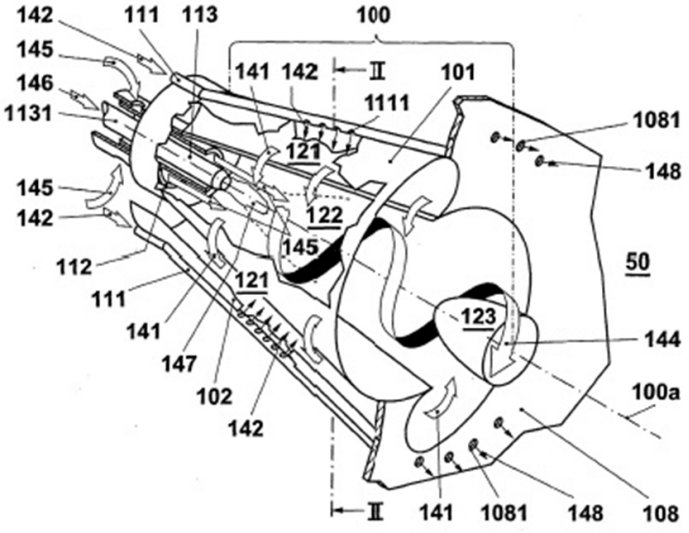

Figure 2.4: Air swirler with a moveable rod (1131), patent from Alstom [7]

2.2.2 Variable geometry air swirler with rotatable sleeve

The patent from General Motors (GM) invented by John M.Vaught in 1976 (Fig. 2.5) describes the adjustment of the swirl by varying the diameter of the entry slots of the prechamber for the primary flow by means of a rotatable sleeve changing the alignment with the primary air passages embedded in the inner bushing. The positioning of the rotatable sleeve is realized with an externally placed hydraulic actuator.

The detailed patent information is given in Ref. [10]. Other patents realize this technique (US 3899881 [11], US 3490230 [12]) also in a combustor.

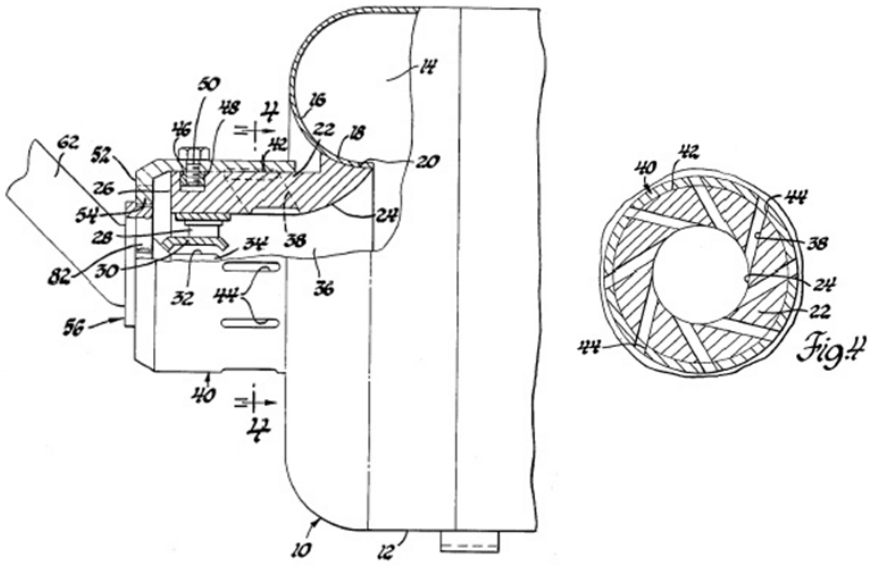

Figure 2.5: Air swirler with rotatable sleeve (40), primary air passages (44), inner bushing (42), patent from General Motors [10]

2.2.3 Variable geometry air swirler with self actuated variable geometry features

The patent from General Electric (GE) invented by Jack Rogers Taylor et al. [13] in 1991 is about a variable geometry air swirler (Fig. 2.6) equipped with a self actuating variable vane system. The vanes consist of bimetallic stripes (blades) acting according to temperature. With this, a self-justification appropriate to operating conditions is achieved by modifying the swirl through positioning of the blades. The vane system operates in a range from 204 °C at closed vanes to 315 °C at opened vanes open, thereby adjusting the swirl between low power and high power operating conditions. These two end positions for each vane are defined through attached pins.

The concept of the self actuating variable vane system requires no externally actuated mechanism and therefore provides high weight efficiency.

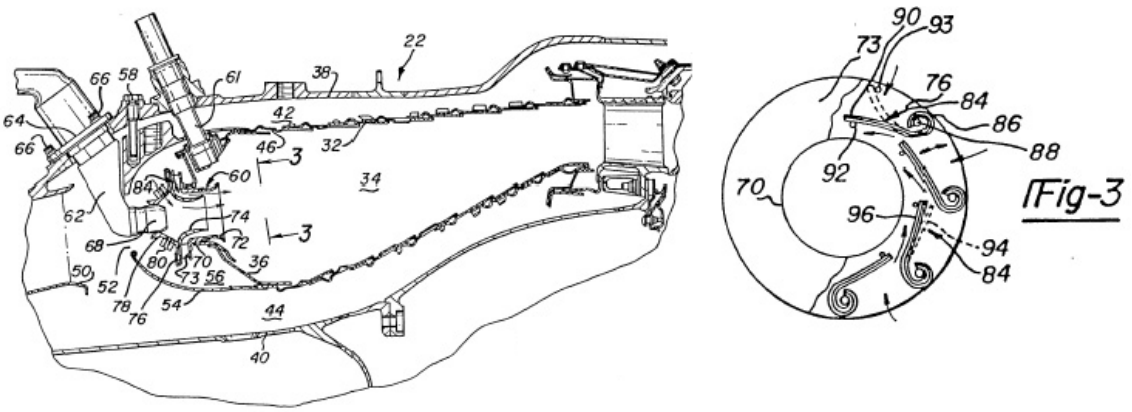

Figure 2.6: Air swirler with self actuating blades (76), attached pins (92 and 93), patent from General Electric [13]

2.2.4 Variable volume combustion chamber for a gas turbine engine

The patent applied by Xavier M.Bardey in 1993 provides a variable volume combustion chamber in a gas turbine. The aim of this invention is to adjust the volume of the combustion chamber according to the operating condition. Therefore the arrangement of maximum volume (Fig. 2.7a) is designed for full power and the minimum volume (Fig. 2.7b) is adjusted for idle power. Moreover, through the moveable walls of the combustion chamber supply of higher volume of oxygen for full power (a high rate of secondary air is required) is provided and vice versa only a reduced portion of oxygen in the position for minimum volume is supplied as required (idle power). The movement of the combustion chamber walls is realized with a telescoping collar segment portion driven by an extendible and retractable piston rod guided in a control cylinder. For further details see [14].

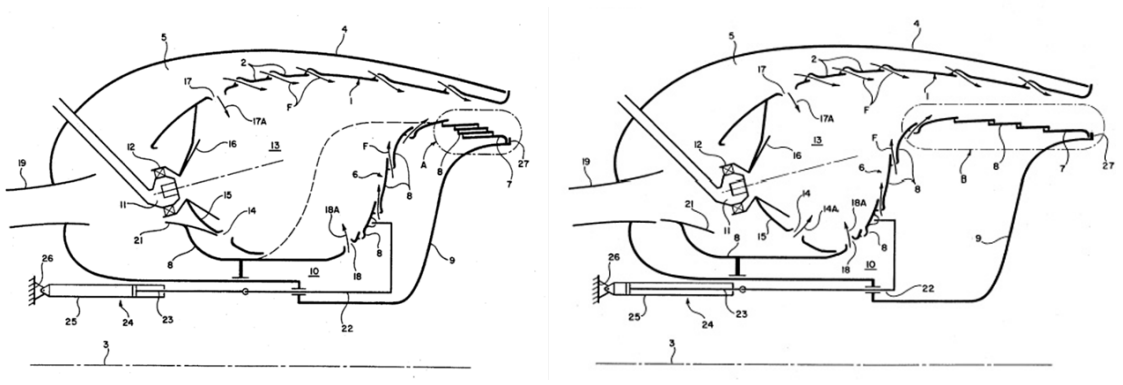

(a) (b)

Figure 2.7: Position of combustion chamber with maximum volume (a), and with minimum volume (b) [14]

Chapter 3

Variable geometry burner

3.1 Setup

The variable geometry burner was designed by T.Leitgeb. A brief overview of the variable geometry burner concept is provided. Detailed Information is given in [3].

In the following three variable parameters are described:

- The amount of axially injected air
- The amount of tangentially injected air
- The outlet surface area of the nozzle

The variable geometry burner (Fig. 3.1), designed by Thomas Leitgeb, basically consists of three main parts. A movable rod (1), an inner bushing (2), and an outer bushing (3). It has separate connectors for axial and tangential air as well as for the fuel supply. The inner bushing has four tangential inlet slots (4) for introducing the swirl to the flow. Mixing between air and fuel is performed in the cavity (5) of the outer bushing. The exit area of the injector nozzle (6) is changed by the rod [3]. The design parameters can be seen in Tab. 3.1.

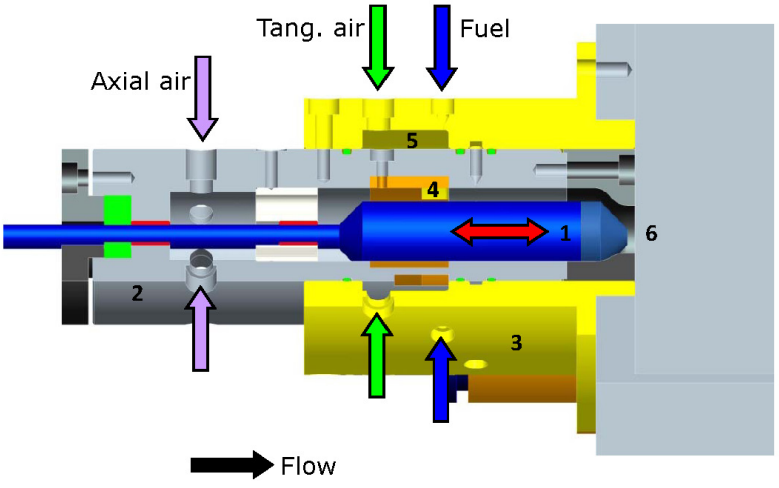

Figure 3.1: Cut of the variable geometry burner [3]

Table 3.1: Technical data of the variable geometry burner [3]

Description	Value
Power	up to 10 kW
Fuel	lean air/methane mixture
Pressure level	up to 5 bar
Nozzle Diameter	18mm

This variable geometry burner applies a movable rod with a conical tip which facilitates different exit areas depending on the axial position. An area ratio (A/A_o) describes the variable exit area as a relation. The maximum position of the rod was +3 mm and vice versa -2 mm. Additionally, the wake of the rod supports the stabilization of the flame [3].

The swirl was generated in the variable geometry burner through tangential entry slots. The swirl strength can be set by the split of axial and tangential air (split = $\dot{m}_{\mathrm{tan}}/\dot{m}_{\mathrm{ax}}$) [3].

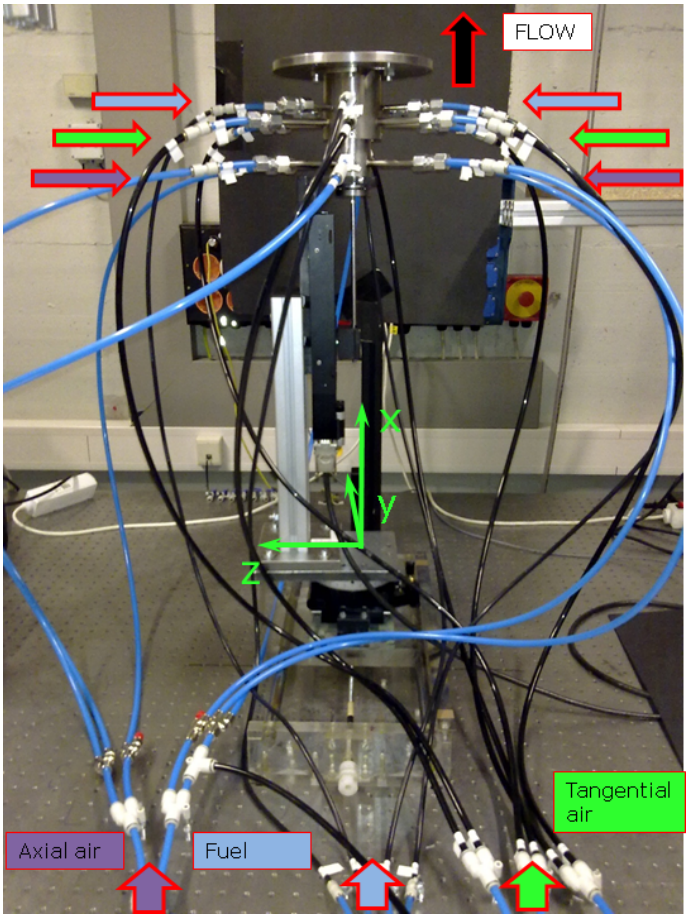

Figure 3.2: Variable geometry burner on the test rig with fuel and air supply

Fig. 3.2 shows the variable geometry burner on the pneumatically damped support (Newport Stabilizer I-2000 Series). The axial and tangential air was fed to the burner with six symmetrically arranged entries. Therefore, the air was equally split to provide a symmetrical air support. The four fuel supplies were arranged at 90 ° to each other. According to a common use of a burner in a gas turbine the x-axis was aligned with the center axis of the variable geometry burner.

3.2 Flame tube

The operation of the burner in a confined environment was realized with the flame tube, providing access to non intrusive measurement. The measurement under confined conditions is a next step in the development and analysis of a burner concept providing also pressurized operating conditions. With the flame zone under confined conditions, including defined supply of secondary air (cooling air), it is also possible to determine the equivalence ratio ϕ (Sec. 4.5.2).

An important criteria for the design of the flame tube was the visibility of the full field of the flame. In case of an attached flame the field of view needs to begin at the exit area of the burner. The dimensioning of the secondary air, for supplying the flame zone with secondary air and also for cooling the flame tube sufficiently (Fig. 3.3b), required on the one hand a sufficient mass flow of secondary air for combustion and on the other hand at the same time a limited entry velocity of cooling air, to avoid a blow out of the flame. For a complete spatial air supply a symmetrical arrangement of the cooling air supplies was needed. For the measurement window in the flame tube the cooling of the glass needed to be paid attention to.

The dimensioning of the cooling air supply of the flame tube was based on the resulting mass flow range under unconfined conditions (about 20 m/s to 5 m/s). A ideal distribution of the total mass flow to the mass flow per exit area was assumed (for example a total mass flow of cooling air supply of 20 g/s would lead to a mass flow of 0.65 g/s per exit area for 32 supplies). Assuming ambient conditions in the flame tube (density ρ = 1,2 kg/m^3) and a velocity direction normal to the supply exit area (A) the velocity v can be obtained by the law of continuity:

$$\mathrm{v} = \frac{\dot{m}}{\rho \cdot A} \tag{3.1}$$

The variable parameters were the diameter of the secondary air supply tube and the number of secondary air feed lines to the flame tube. The validation for the optimal mass flow and velocity in the exit area of the secondary air showed that acceptable results could be achieved with 32 supplies of secondary air, with supply tubes of 4 mm in diameter (Tab. 3.2).

Fig. 3.3a shows the components of the flame tube. The basis of the flame tube was a hollow profile with dimension of 140x140x250 mm, made of S275JOH steel, from the firm Grosschaedel. The company Dornauer-Grillitsch laser cutted the required field

of view. All other manufacturing processes were carried out in the work shop of the Institute for Thermal Turbomachinery and Machine Dynamics. The flame tube was firmly connected with the headplate via a welded joint. The headplate was connected with a removable screw connection to the burner. The secondary air supplying tubes were adapted with the fittings of SMC made of stainless steel featuring a low space requirement and a heat resistance of about 250°C. The quartz glass, made of silux, resistant to high temperatures, was attached with a surrounding frame to the flame tube. A teflon material between quartz glass and flame tube provided sealing and damping. A covering plate, added with a removable connection to the flame tube, offered provision for further adaption to the test rig. Thereby, for instance, with the reduction of the exit area of the flame tube, a flame behaviour under back pressure could be additionally investigated. The drawings of the components of the flame tube are given in Appendix A.

Fig. 3.4a shows the burner in operation with the flame tube. A thermal image (Fig. 3.4b) shows the temperature distribution of the flame tube structure in operation, depicting that the flame tube reaches a temperature of around 600°C in operation.

Table 3.2: Mass flow and velocity of cooling air for flame tube

Mass flow (total) (g/s)	Mass flow (per exit area) (g/s)	Velocity at exit area (g/s)
20	0.65	41.3
15	0.47	31
10	0.31	20.6
5	0.16	10,3

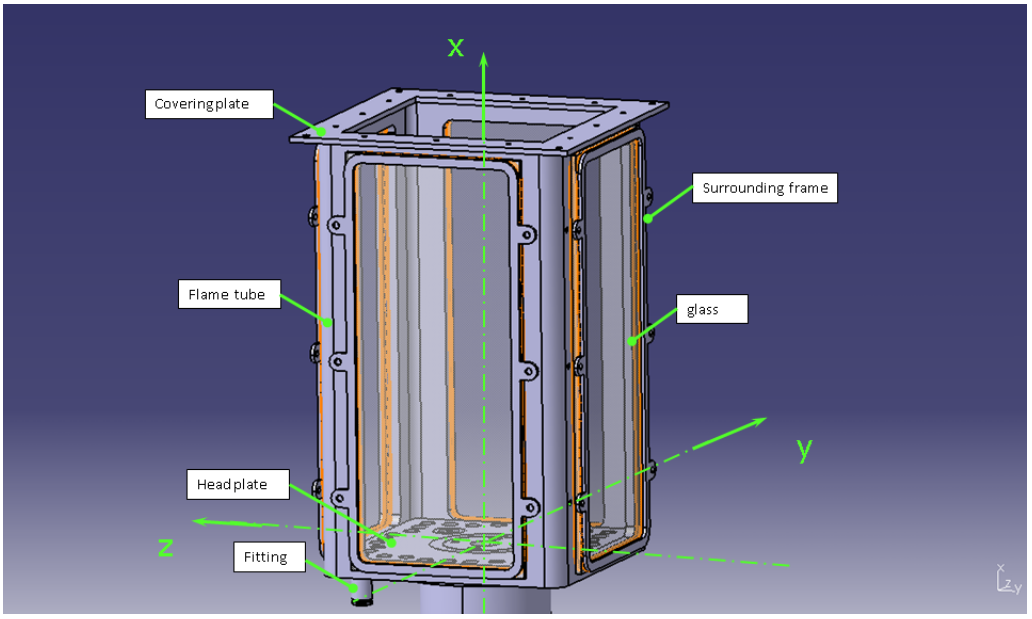

(a) Flame tube side view

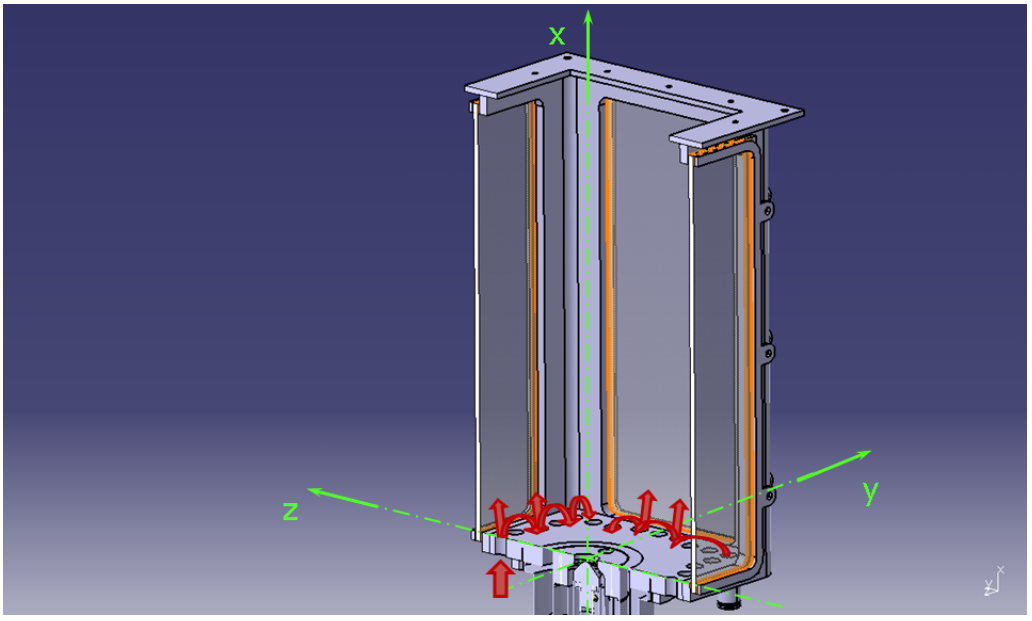

(b) Flame tube cut view - function of secondary air flow (cooling and air supply)

Figure 3.3: Flame tube side view and cut view

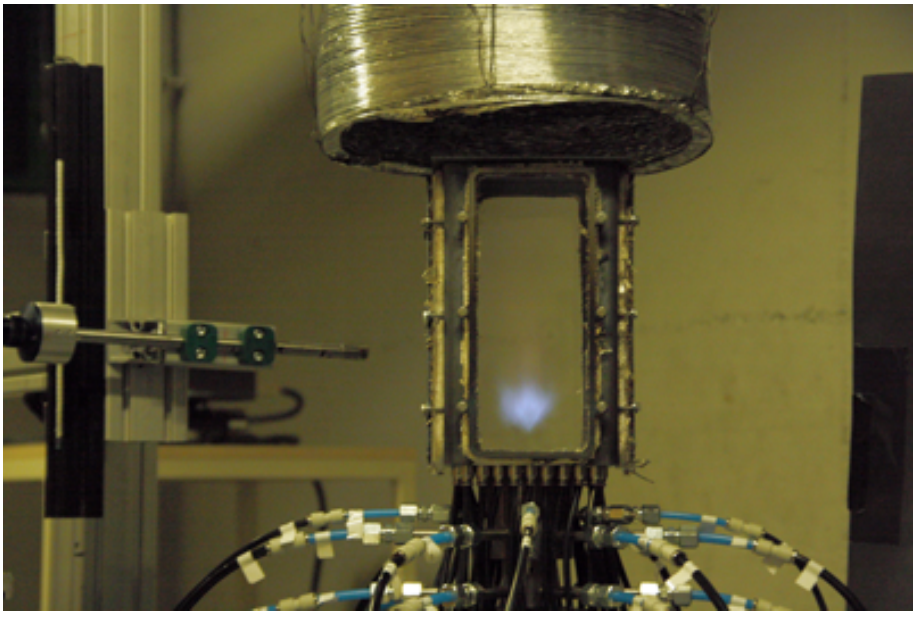

(a) The burner in operation with the flame tube [3]

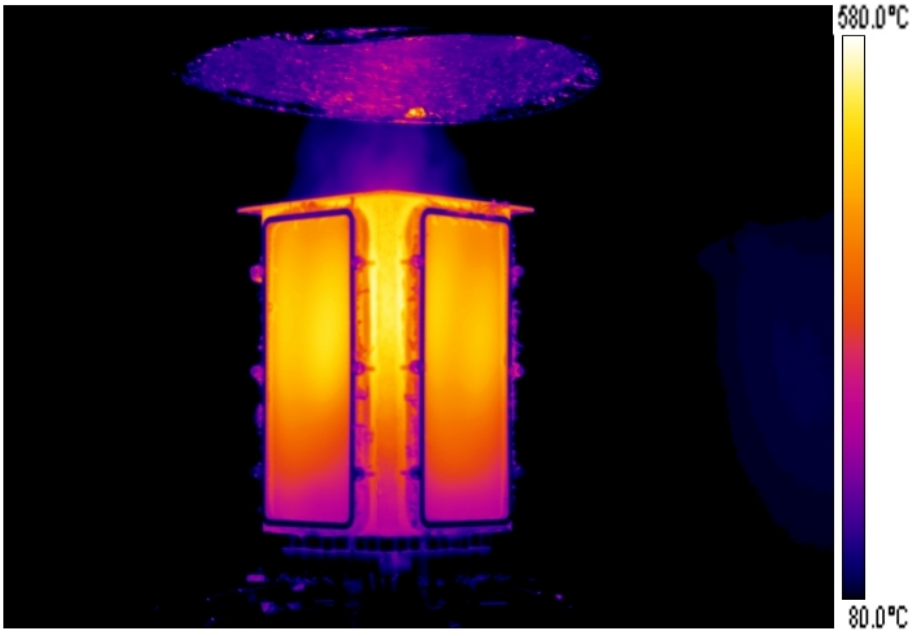

(b) Infrared picture of the burner with the flame tube in operation

Figure 3.4: Burner in operation with flame tube (a) and a infrared picture of the burner with the flame tube (b)

Chapter 4

Experimental setup

4.1 Test rig

Within the test rig the burner was placed vertically on a pneumatically damped support (NEWPORT Stabilizer I-2000 Series) together with the associated diagnostics.

Fig. 4.1 shows the test rig setup for confined measurements, for the example of the PIV measurements as described in detail in Chap. 5.4. The PIV camera detected the flame of the burner. The direction of the light sheet of the PIV measurement is defined by the optical head. The supports provided fuel and air supply. An exhaust suction unit was placed above the burner, which was equipped with a ventilator at the exit.

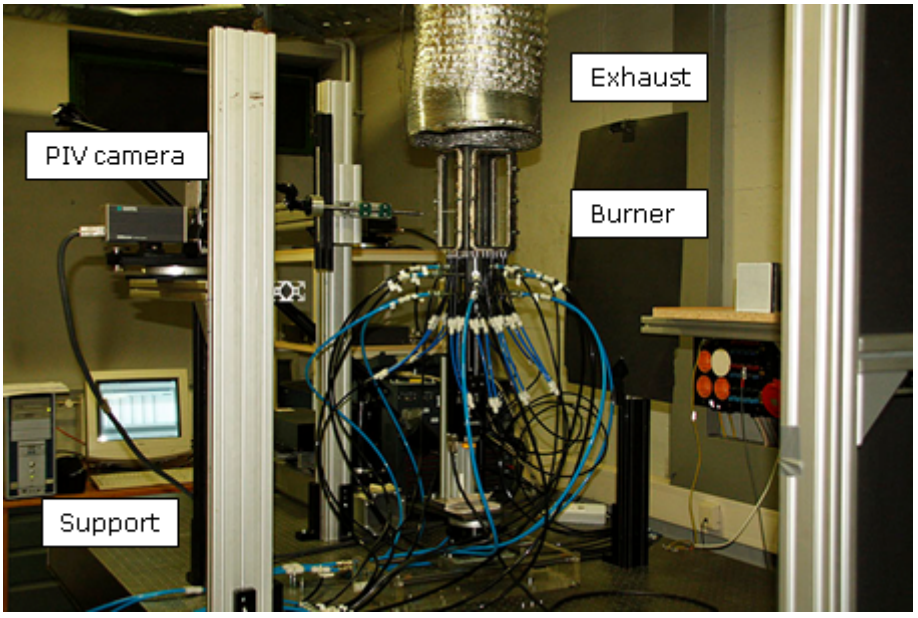

Figure 4.1: Test rig setup for confined PIV measurements [3]

A schematic of the test assembly with the used components can be seen in Fig. 4.2.

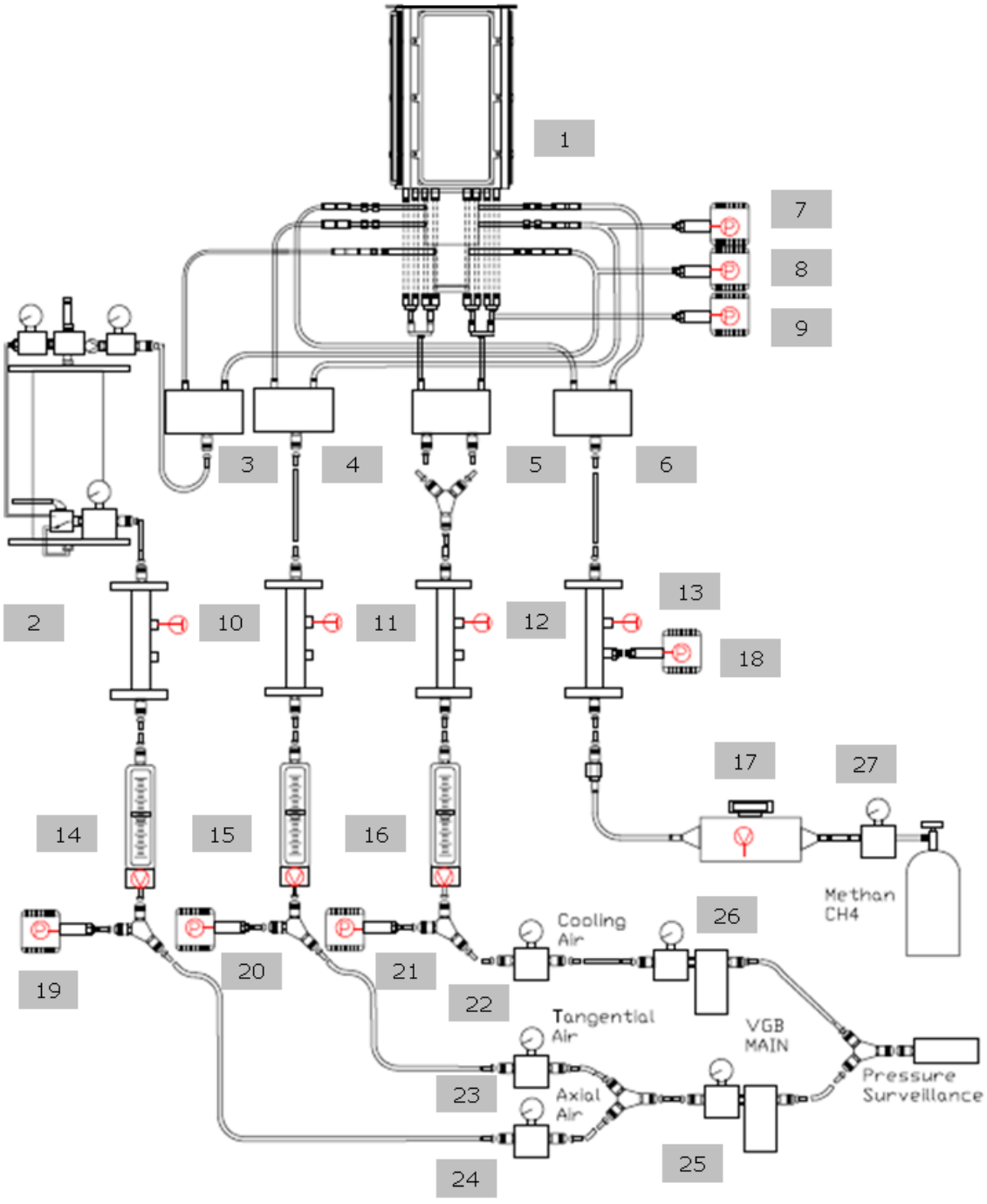

Figure 4.2: Test assembly with instrumentation

Table 4.1: Component description of the test rig

Pos.	Description
1	burner
2	seeding generator
3-6	distribution boxes
7-9	pressure transducers
10-13	temperature sensors
14-16	air mass flow meters
17	fuel mass flow meter
18-21	pressure transducers
22-26	control valves main air
27	control valve fuel

4.1.1 Air supply

The air supply was provided through the air pressure supply of the university. The air was led to the burner with tubes of sizes of 9 mm, 6 mm, 4 mm depending on the required mass flow. The tubes were connected through fittings, which allow a quick change within the test rig. Distribution boxes were included in the test rig, placed right before the air was split up into the required tubes, which in turn were directly connected to the burner (Fig. 4.2). The distribution boxes provided a minimal loss of pressure and ensured a uniform distribution, which was required for a uniform air supply to the burner (symmetry of air supply). The mass flow rates of air were adjusted by manually actuated valves. The inlet pressure of the air was set to 2 bar leading to ambient pressure at the burner.

4.1.2 Fuel supply

Methane CH_4 (fuel) from the firm Air Liquide (specification of the employed methane see [15]) supplied from a gas cylinder was also fed to the burner with tubes connected with fittings for ease of handling. The control valve, which was adjusted manually was placed at the gas cylinder. A distribution box also ensured a uniform distribution for a symmetrical supply of the burner.

4.1.3 Rotation and linear moving unit

The measurements required a rotation of the burner (for tomographic reconstruction). Therefore, a rotation unit, rotating around the x-axis (Fig. 4.3) was employed, providing 360° rotation, a scale with a reference marking for alignment, and means for moving and rotating the attached burner for adjustment to the center axis. The

justification for the placement in the center axis was achieved with a camera focussing on the rod of the burner. While rotating the burner in both directions, the parameters of the rotating unit were adjusted until the shift of the referenced rod was minimal and therefore a correct alignment of the burner in the center axis was accomplished. The rotation unit was mounted onto a linear moving unit, moving in y direction, (Fig. 4.3). This was necessary for a better alignment of the burner and the PIV lasersheet. It allowed investigation of other planes parallel to the center plane. The moving unit also provided a measurement scale and a reference marking on the sledge. Both units were actuated manually.

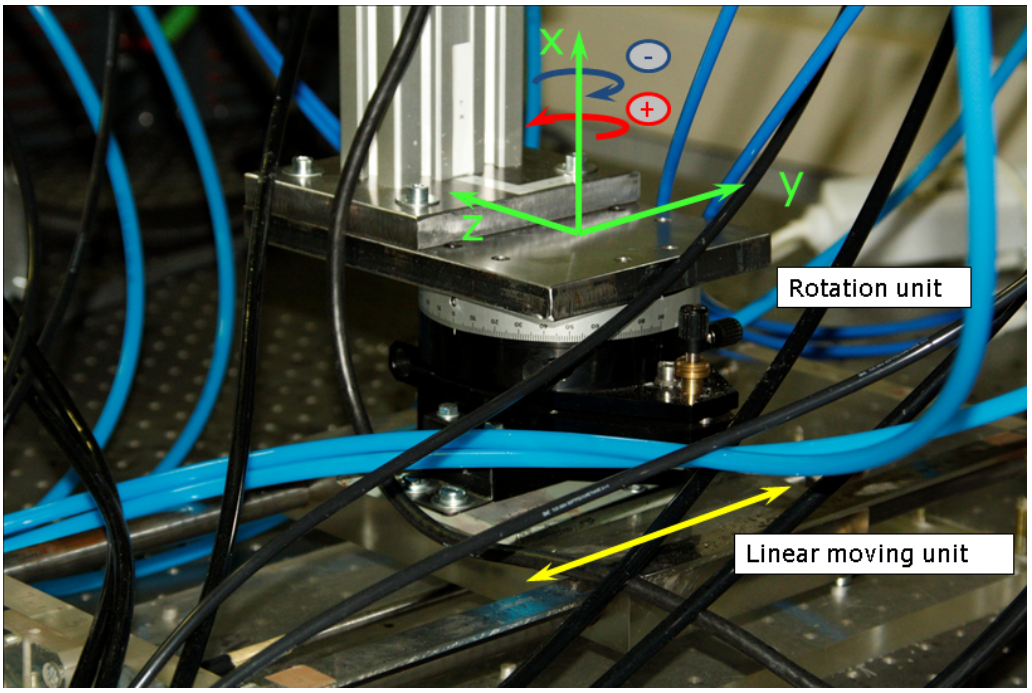

Figure 4.3: Rotation and linear moving unit [3]

4.1.4 Actuator for adjusting the variable area nozzle

One of the influence parameters of the variable geometry burner was the variable exit area. This variable geometry burner applies a movable rod with a conical tip which facilitates different exit areas depending on the axial position [3]. Therefore a mechanical actuating was realized. The movable rod was controlled by a linear motor actuator (Fig. 4.4).

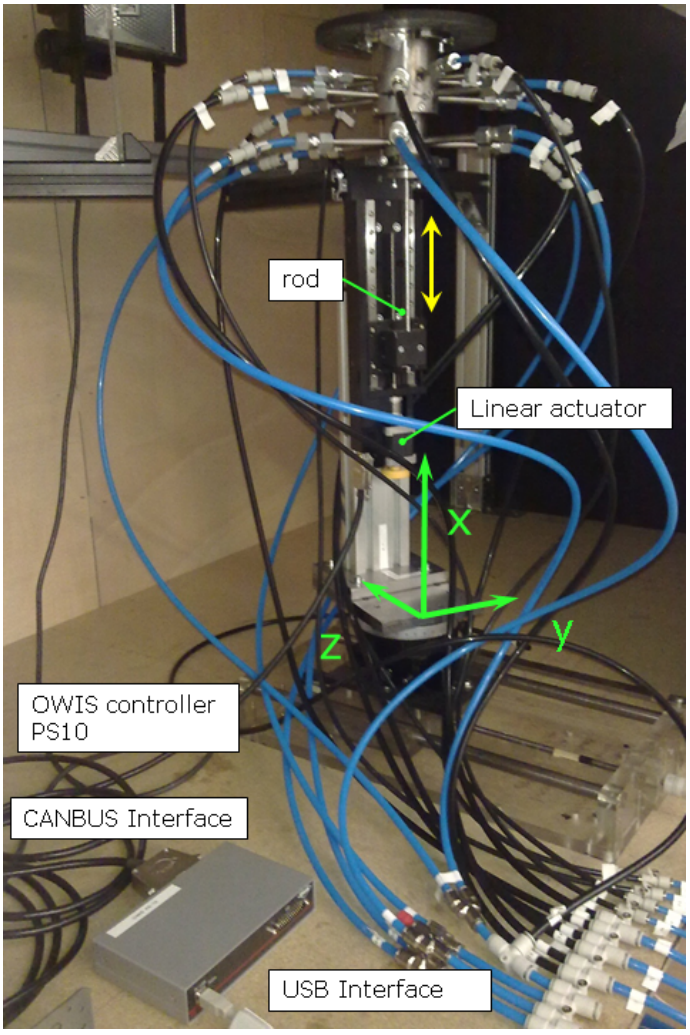

Figure 4.4: Linear actuator for rod with controller of OWIS type PS10

The features of the actuator were the transmission ratio of 1 to 10000 and the electronical or manual control of the actuator. A regulating mechanism provided a non-scaling manually setting of the rod. For the electronically controlling hardware, OWIS PS10 (Fig. 4.4) [16] and software, OWIS v.260, from OWIS was employed. The actuator moved the rod on the x-axis of the variable geometry burner coordinate system in positive and negative direction. The positioning range of the rod was between +3 mm and -2 mm.

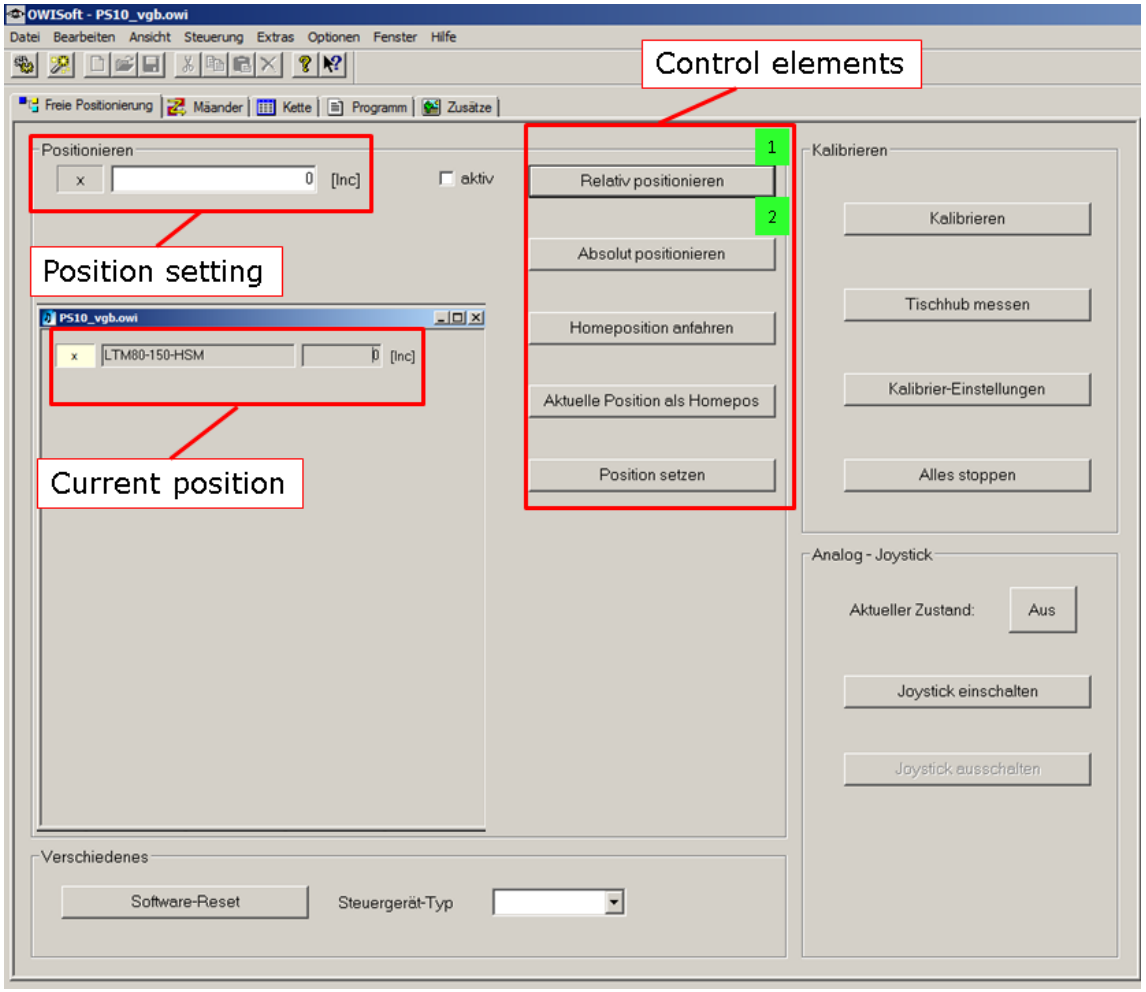

Figure 4.5: User interface (control panel) of the OWIS software

Fig. 4.5 shows the control panel of the OWIS software. The data value for the position was set in increments. One increment corresponds to 1/10000 mm. Absolute (1) or relative (2) position could be selected. The current position was additionally displayed.

4.2 Instrumentation

To obtain the required operating data the following sensors were used. Their application allowed data acquisition as well as monitoring of the process parameters (Fig. 4.6).

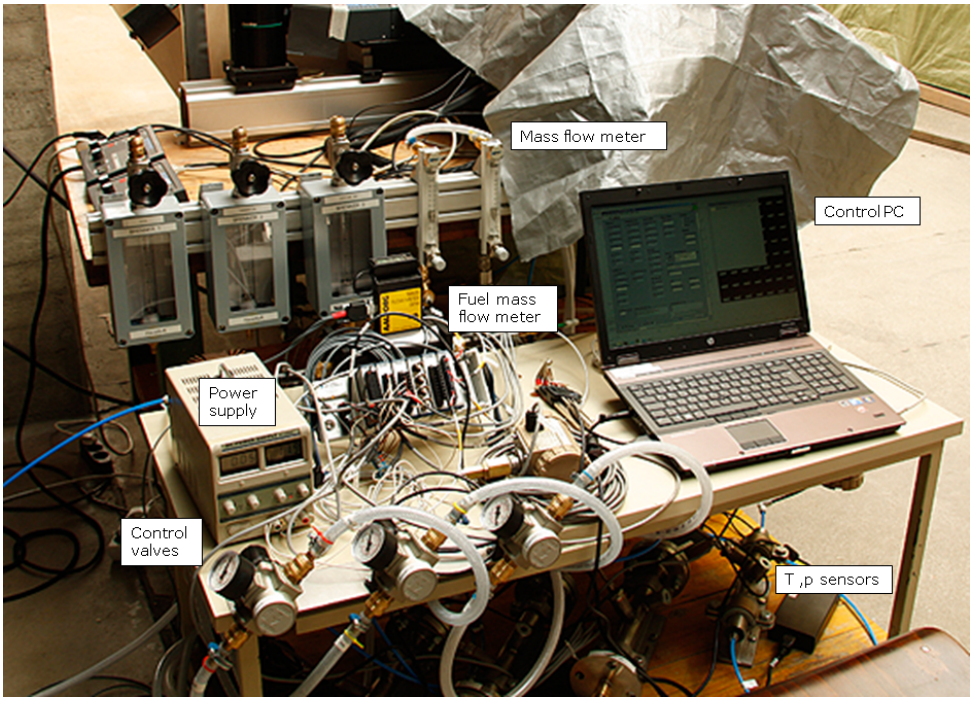

Figure 4.6: Instrumentation and measurement locations

4.2.1 Pressure sensors

The pressure transducers, type 6051 from Samsomatic (Fig. 4.7), were adjusted from 0 to 9 bar absolute pressure. The electrical transmitter converts the measured pressure into an output signal from 4 to 20 mA [17]. The block diagram of transmitting the measurement signal into an electric signal is shown in Fig. 4.8. The block diagram shows also the four wire application of the pressure transducer.

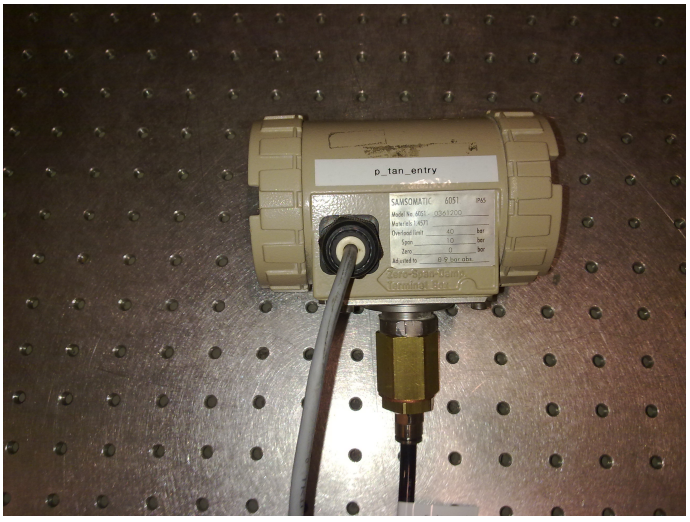

Figure 4.7: Pressure transducers type 6051 from Samsomatic

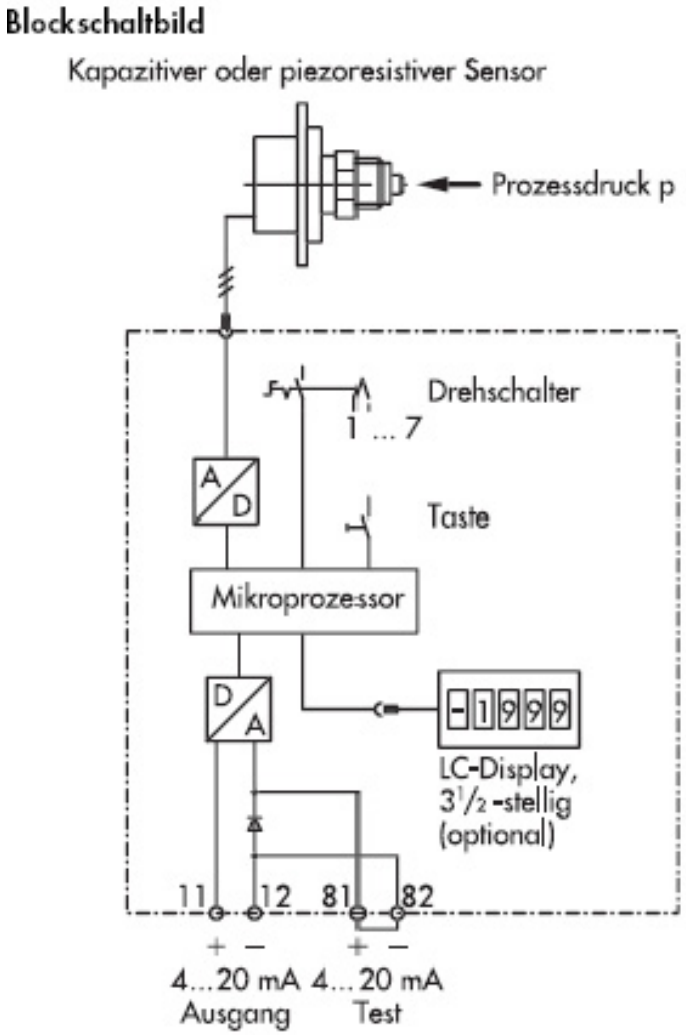

Figure 4.8: Block diagram of the pressure transducers of type 6051 [17]

4.2.2 Temperature sensors

Temperature was measured in the test rig for the variable geometry burner with resistive thermal devices of type P-MTF-A-6-300-0-T-5M. The resistive thermal sensor derives the sensed object temperature value through the calibrated temperature characteristic resistance (Fig. 4.9) of the measurement head.

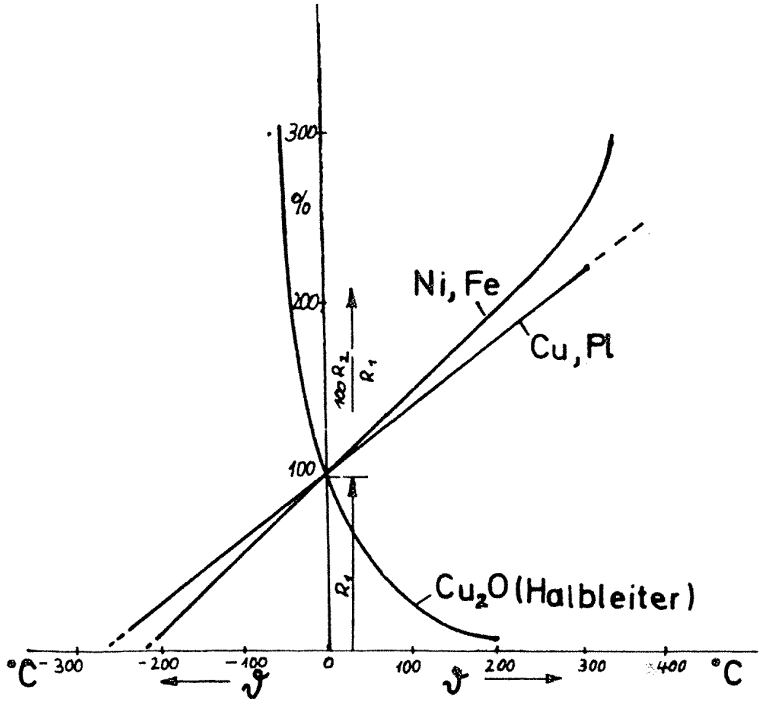

Figure 4.9: Resistance temperature characteristic of important conductors and semiconductors [18]

The resistance is measured through current feed and voltage measurement. The detected voltage is related to the temperature according to the resistance characteristic with material defined parameters. The resistance material of the devices used was Platin with a provided temperature measurement range up to 600 °C. For the resistance R_1 at the temperature ϑ_1 and the resistance R_2 at the temperature ϑ_2 the following relationship is provided up to a temperature of 100 ° (with the temperature constant α) [18]:

$$R_2 = R_1[1 + \alpha(\vartheta_2 - \vartheta_1)] \tag{4.1}$$

$$\alpha = 3,85 \cdot 10^{-}3/°\text{C (Platin)}$$

Hence, the difference in resistance ΔR is proportional to the difference in temperature $\Delta\vartheta$. Furthermore, the employed resistive thermal devices provided a four wire configuration for separate current feed and voltage detection in order to keep the measurement error minimal especially in a long access line. Fig. 4.10 shows the circuit layout of the connection of a four wire resistive thermal device to the analog input module NI-9217 for data acquisition (Sec. 4.3). The circuit layouts of the instruments of the variable geometry burner test rig are given in Appendix B.

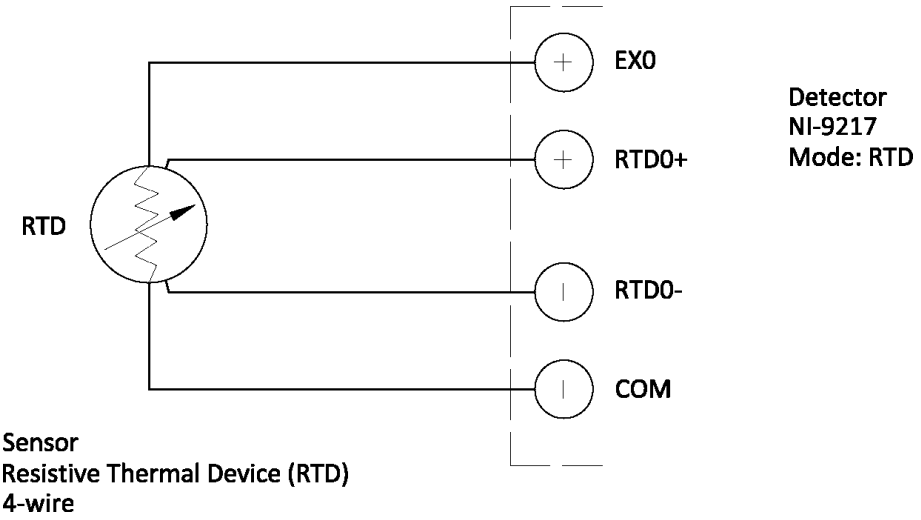

Figure 4.10: Circuit layout of the connection of a four wire resistive thermal device with the analog input module NI-9217

Fig. 4.11 shows the arrangement of the temperature sensors in the test rig. A connecting pipe was positioned on the Mobile test rig VGB control (Fig. 5.37). This connecting pipe provided an adjustment for a temperature sensor in order that the measurement head detected the flow temperature properly.

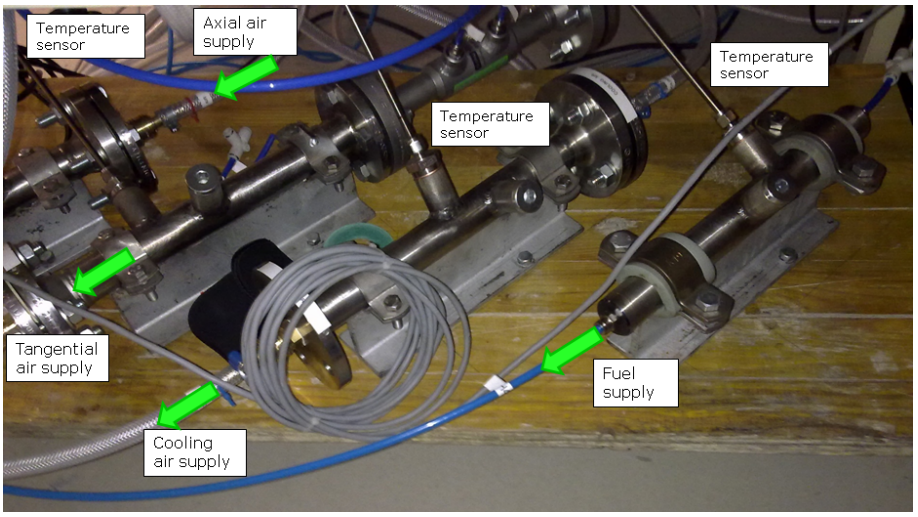

Figure 4.11: Settings of the temperature sensors in the burner test rig

4.2.3 Fuel mass flow meter

For the determination of the fuel (methane CH_4) volume mass flow, the mass flow meter type GFM77 with the series number 1-800-866-3837, Aalborg, shown in Fig. 4.12, was employed.

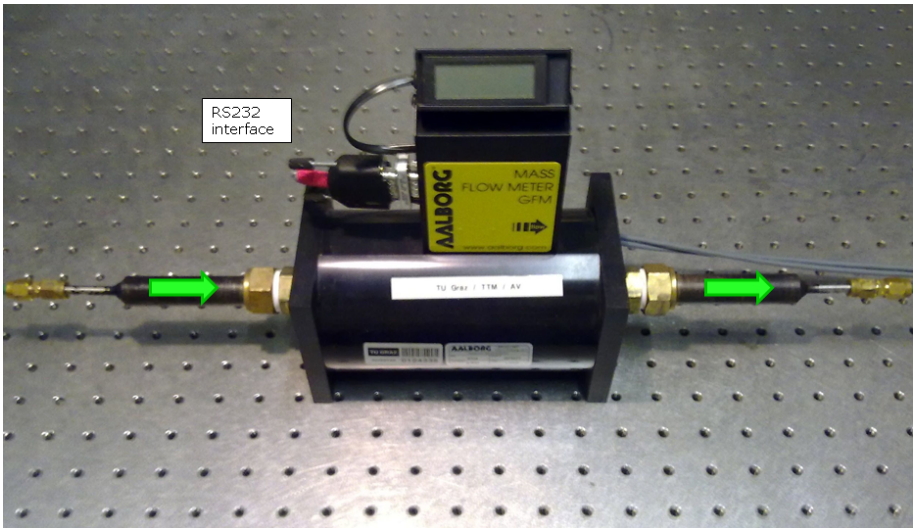

Figure 4.12: Mass flow meter of type GFM77 from Aalborg

The mass flow meter is specified for a flow range from 0-500 liters/min and able to handle a maximum pressure of 500 psi or 34 bar. The value of mass flow is displayed on a liquide crystal display (LCD). Furthermore, output signals are in the range of 0 to 5 VDC and 4 to 20 mA, representative of the metered gas mass molecular flow rates, were readout through an RS232 connector [19]. The mass flow meter requires a power supply of 12 VDC.The measurement signal of the mass flow meter indicates liters/minute referred to standard conditions [19]. The standard density provides conversion of the measurement signal. Thereby, the mass flow of methane CH_4 was obtained by multiplying the resulting volume flow with the density of methane ρ_{CH_4} at standard conditions (ρ_{CH_4} = 0,6645 kg/m^3 for p_o = 1,014 bar and T_o = 21,1 °C = 294,1 K [19]).

In the mass flow meter the flow path gets split into a primary flow conduit and a capillary sensor tube. To maintain a constant ratio of these flow rates a laminar flow is adjusted. On the sensor tube two precision temperature windings are heated. The active gas flow transports the heat from the upstream winding to the downstream winding. The change in the resistance of the sensor windings is proportional to the temperature differential. A Wheatstone bridge design is used to monitor the temperature dependent resistance gradient on the sensor windings which is linearly proportional to the instantaneous rate of flow [19].

4.2.4 Air mass flow meter

In a first test step the differential pressure was detected with a venturi cone measurement instrument, V-Cone from McCrometer, in order to quantify the mass flow $\dot{m}$. A lasting differential pressure Δp was generated by a constricted area in the pipe. The higher pressure p_1 was measured slightly upstream of the cone and the lower pressure p_2 in the downstream face of the cone itself [20] (Fig. 4.13). Beside the used venturi cone, other differential pressure flowmeters employ a variety of

standardized orifice plates. Furthermore, by the detection of absolute pressure and the temperature in the flow field, the mass flow $\dot{m}$ (Eq. 4.4) can be determined by the law of continuity (Eq. 4.2) and Bernoulli's law (Eq. 4.3). A constant, *const* in Eq. 4.4, considers figures of unity, flow losses, operating conditions, gas expansion values, and Reynolds number.

$$\rho_1 A_1 w_1 = \rho_2 A_2 w_2 \tag{4.2}$$

$$p_1 + \rho_1 g h_1 + \frac{\rho_1 w_1^2}{2} = p_2 + \rho_2 g h_2 + \frac{\rho_2 w_2^2}{2} \tag{4.3}$$

$$\dot{m} = const \sqrt{\frac{\Delta p}{\rho_{ref}}} \tag{4.4}$$

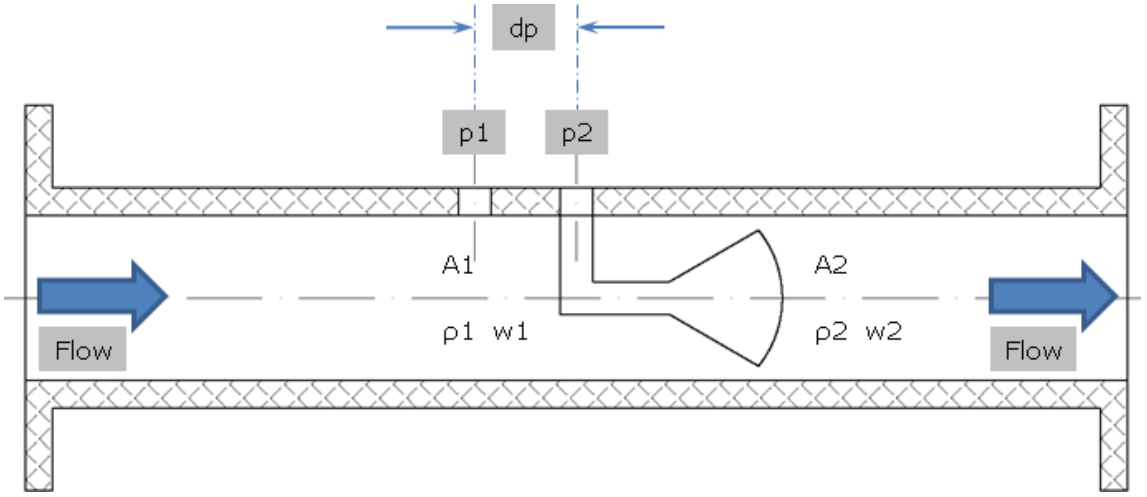

Figure 4.13: Principle of a venturi cone [20]

The operating region of the burner lied in a range of mass flow which was too low for V-Cones differential pressure flowmeters. Therefore, rotameters with an operating range from 10 liters/min to 100 liters/min were applied. Additionally, rotameters with a range from 30 liters/min to 200 liters/min could have been connected.

In a rotameter (Fig. 4.14) the measured media enters through the bottom and pushes a float, which is placed in a conically enlarged tube (ρ_L = Density of the fluid, w = Flow velocity, A = inflow area of the float, D_K = diameter of the tube m = mass of the float, V = volume of the float, D_S = diameter of the float, ρ_S = density of the float, c_w = drag coefficient of the float in the measuring tube).

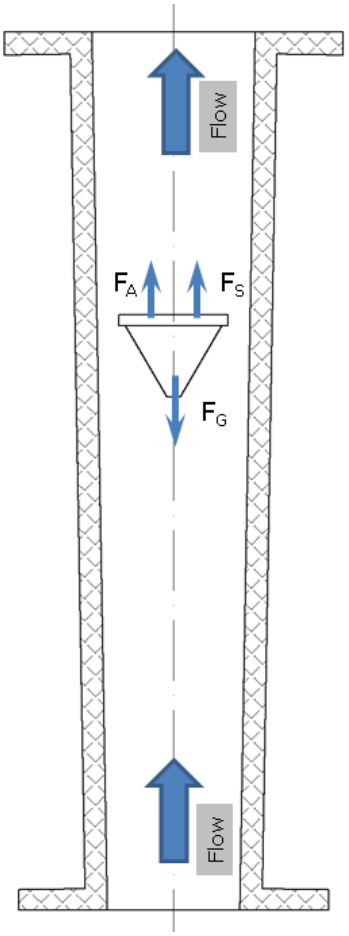

Figure 4.14: Principle of a Rotameter (VDE/VDI 3513)

Three forces act on the float

- gravitation $F_G = m \cdot g$
- buoyancy $F_A = m \cdot g \cdot \dfrac{\rho_L}{\rho_s}$
- flow force $F_S = A \cdot \rho_L \cdot \dfrac{w^2}{2} \cdot c_w$

The balance (Eq. 4.5) between gravitation (F_G), buoyancy (F_A), and flow force (F_S) defines the height level of the float, which can be read from a scale, which is a measure for the volume mass flow.

$$\underbrace{F_A}_{m \cdot g \cdot \frac{\rho_L}{\rho_s}} - \underbrace{F_G}_{m \cdot g} - \underbrace{F_S}_{A \cdot \rho_L \cdot \frac{w^2}{2} \cdot c_w} = 0 \tag{4.5}$$

The mass flow q_m and the volume mass flow q_v in a rotameter is defined as follows (calculation method for mass flow in a rotameter based on VDE/VDI 3513 on CD):

$$\text{Mass flow:} \qquad q_m = \alpha \cdot D_S \cdot \sqrt{m \cdot g \cdot \rho_L (1 - \rho_L/\rho_S)} \tag{4.6}$$

$$\text{Volume Mass flow:} \qquad q_v = \frac{\alpha}{\rho_L} \cdot D_S \cdot \sqrt{m \cdot g \cdot \rho_L (1 - \rho_L/\rho_S)} \tag{4.7}$$

The flow number α is a function of the diameter ratio $\delta = D_K/D_S$ and the Ruppel-Zahl Ru, with η = dynamical viscosity of the measurement media (VDE/VDI 3513)

$$\text{Ruppel-Zahl Ru:} \qquad Ru = \frac{\eta}{\sqrt{m \cdot g \cdot \rho (1 - \rho/\rho_S)}} \tag{4.8}$$

If operating parameters (T_1, p_1) change over the time (T_2, p_2), the influence on the mass flow (q_M^{New}, q_M^{Before}) and the volume mass flow (q_V^{New}, q_V^{Before}) is considered according to Eq. 4.9 [21]. In scope of the PIV measurements the pressure loss in the axial air supply caused by the seeding generator was considered.

$$\begin{aligned} q_M^{New} &= \sqrt{\tfrac{p_2}{p_1}} \cdot \sqrt{\tfrac{T_2}{T_1}} \cdot q_M^{Before} \\ q_V^{New} &= \sqrt{\tfrac{p_2}{p_1}} \cdot \sqrt{\tfrac{T_2}{T_1}} \cdot q_V^{Before} \end{aligned} \tag{4.9}$$

Similar to the case described above, the rotameters find their application generally in areas of small values of mass flow. Further properties of the rotameters are simple construction, robustness, and linear scale with a high accuracy (error $\sim 2\,\%$). Additionally, it needs to be noticed, that the float produces a small loss of pressure in the flow. The datasheet of the employed rotameter tyoe UNIFLUX is given in Appendix C.

4.3 Measurement control and data acquisition

The test rig for the variable geometry burner additionally included the detection and adjustment of the operating settings by active and passive controlling. In this scope electronical processing of the parameter values of the modular burner test rig included corresponding data storage.

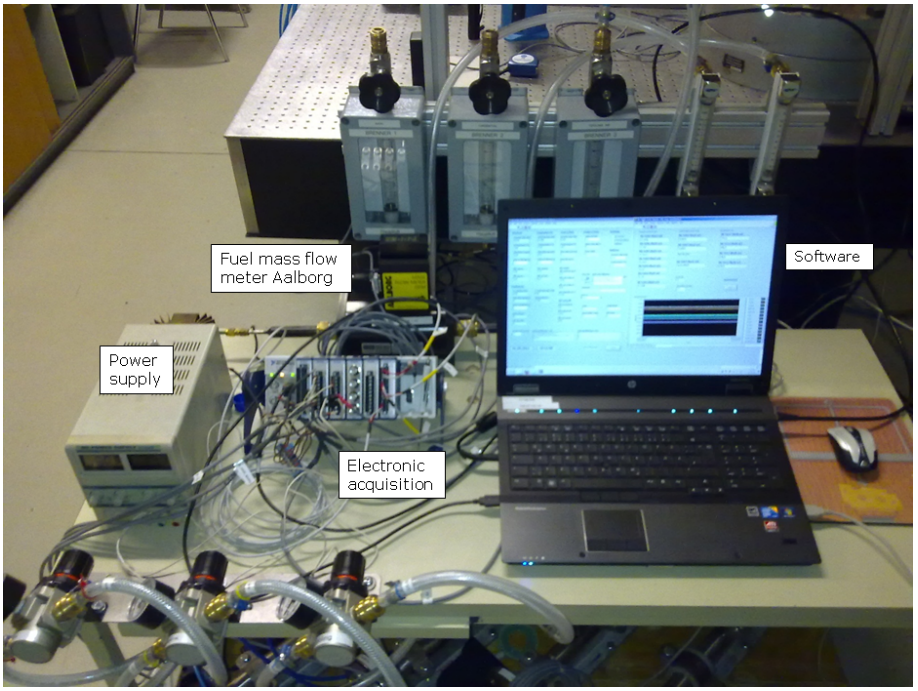

Figure 4.15: Data acquisition setup

An overview of the measurement control and data acquisition is shown in Fig. 4.15. A external power supply fed the pressure transducer for the four wire configuration and the fuel mass flow meter from Aalborg with 12 VDC. The Instrumentations of the burner test rig, explained in detail in Chap. 4.2 were connected to the National Instrument CompactDAQ Chassi (NI cDAQ-9178) including the analog input modules NI-9213, NI9203 and NI-9217 (Fig. 4.16). The pin assignments of the analog input modules to the burner test element is shown in Fig. 4.17. The NI-CompactDAQ-Chassis was connected via USB to the measurement Laptop (HP EliteBook 8540p, Windows 7) in order to display the current measurement values and also to achieve storage of the measurement data for subsequent evaluation.

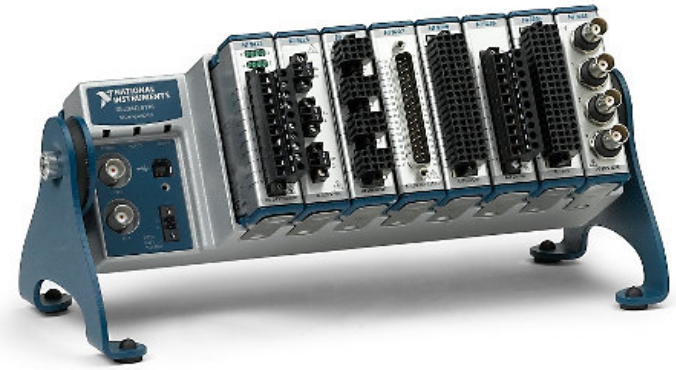

Figure 4.16: National Instruments Chassis type NI cDAQ-9178 with inserted modules [22]

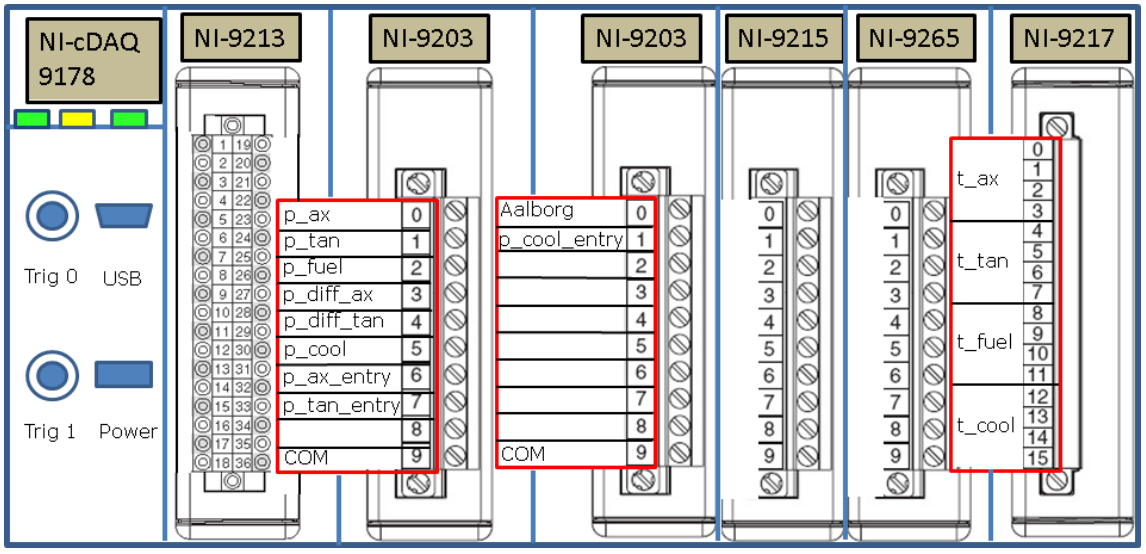

Figure 4.17: PIN assignment of National Instruments chassis of type NI cDAQ-9178 with analog input modules

Fig. 4.18 shows the measurement data flow of a pressure transducer including the NI-CompactDAQ-Chassi (NI cDAQ-9178) with the analog modules to the measurement laptop. With the employed routines, called "Main_Grab_Signals.vi" and "Main_Processing.vi" of the software program LabVIEW the measurement data were monitored and furthermore recorded.

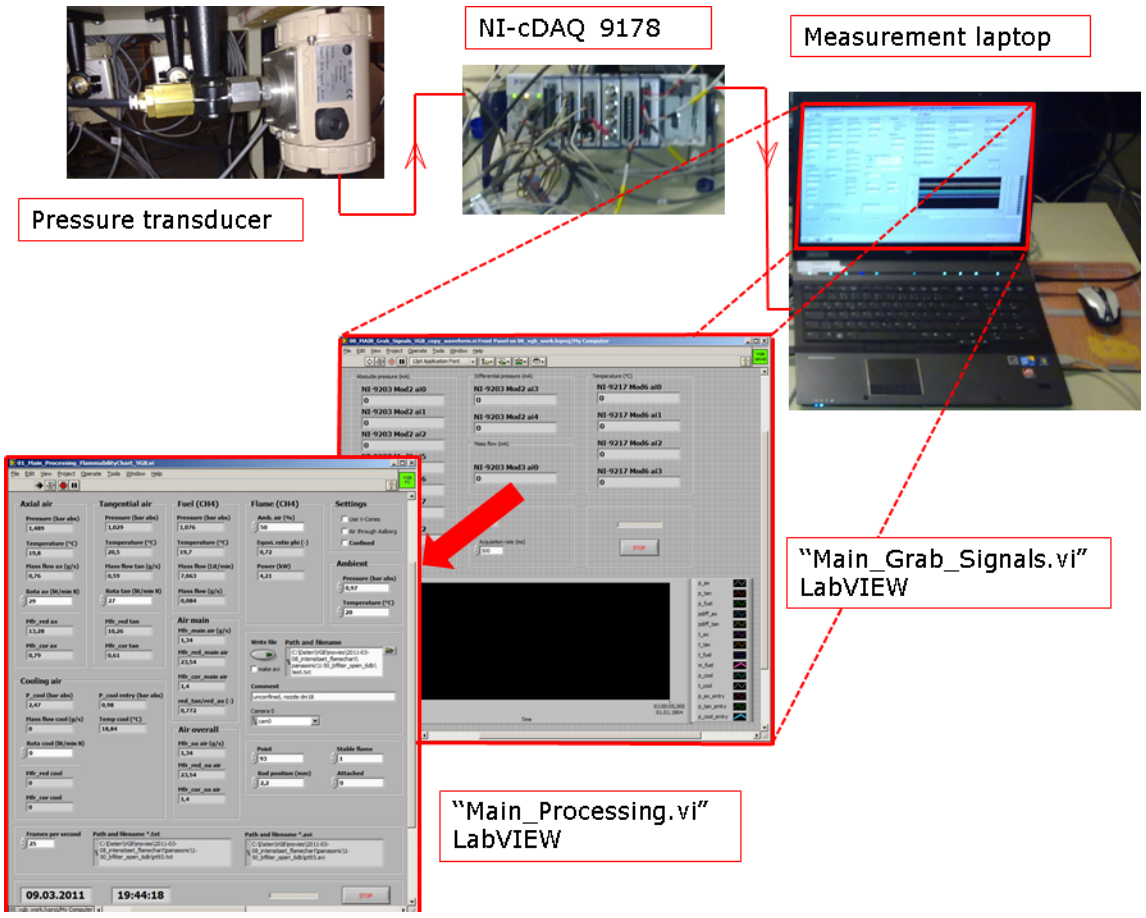

Figure 4.18: Data flow from the sensor to the software program

The processing, monitoring, and the storage of the measurement data was managed with the software **Lab**oratory **V**irtual **I**nstrumentation **E**ngineering **W**orkbench (LabVIEW version 8.6). LabVIEW is a software program providing control routines for measurement- and automation tasks. LabVIEW is a graphical programming environment software. LabVIEW is composed of a user interface (front panel) and a block diagram, describing in a logical manner the relevant measurement process. Examples of these two elements are shown in Fig. 4.19.

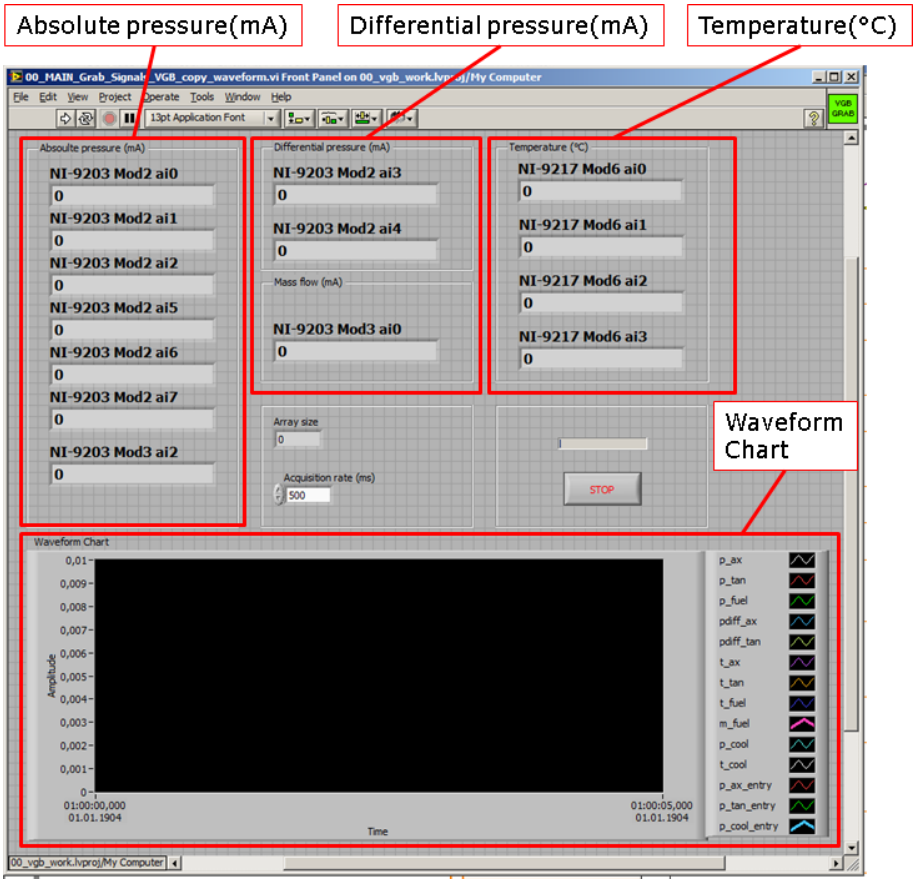

(a) User interface (front panel) of LabVIEW for "Main_Grab_Signals.vi"

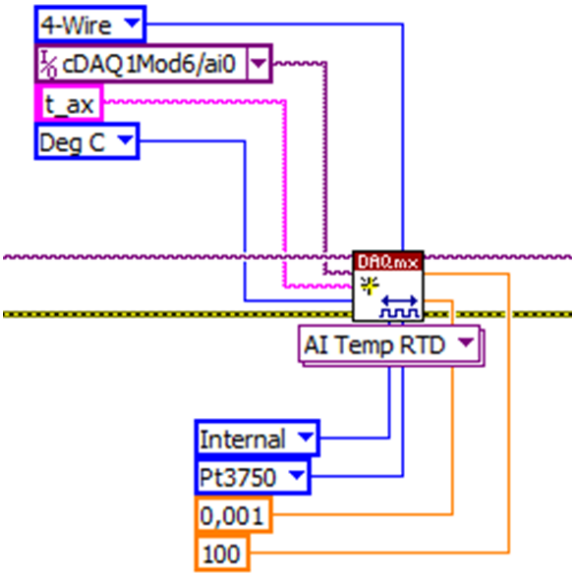

(b) Block diagram of LabVIEW for temperature sensor

Figure 4.19: The two elements of LabVIEW are the frontpanel (a) and the block diagram (b)

The electronically recorded measurement signal is converted into the corresponding physical value in the LabVIEW routine, called "Main_Grab_Signals.vi". The block diagram on Fig. 4.19b shows the acquisition of the electronical signal from PIN aiO (signal from the axial temperature sensor) of the input module NI-9217 in the NI-cDAQ-9178 Chassis (Fig. 4.17) into the LabVIEW routine "Main_Grab_Signals.vi". Appropriate configurations can be set, for instance the four-wire configuration, the temperature unit °C, the type of temperature sensor Pt3750. This component was programmed in modular manner in order to obtain a flexible arrangement for further cases.

Fig. 4.19a shows the structure of the data presentation. The user interface (front panel) of "Main_Grab_Signals.vi" presents the absolute pressure signal in mA, the differential pressure in mA and the temperature in °C. Furthermore a waveform chart displays the received measurement signals. The acquisition rate can be manually adjusted in the Routine "Main_Grab_Signals.vi". The acquisition rate was generally set to 500 ms during the variable geometry burner tests.

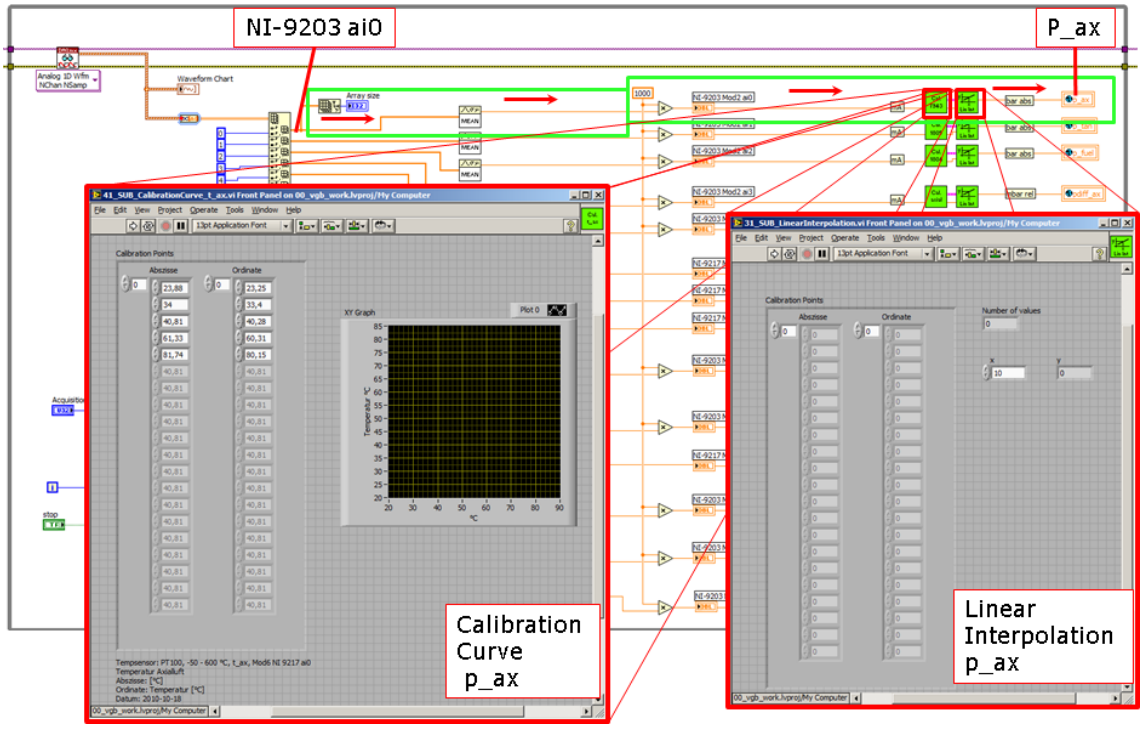

Figure 4.20: Screenshot of the Block Diagram of the "Main_Grab_Signals.vi" routine showing the data acquisition of the measurement signal from the pressure transducer p_ax to the corresponding physical value

A screenshot of the corresponding block diagram of the "Main_Grab_Signals.vi" routine is shown in Fig. 4.20. Out of the full set of data acquisition of the instruments in the test rig of the variable geometry burner performed with the "Main_Grab_Signals.vi" routine, the example shows in detail the conversion of the incoming measurement signal of the pressure transducer for axial air (No.19 in Fig. 4.2) to the physical value. The received electronical signal from the Pin ai0 of the analog module NI9203

(Fig. 4.17) is evaluated according to the calibration curve. The calibration curve was obtained by recording the signals corresponding to interval temperature values, which were adjusted in a calibration device (OMEGA CL-710 A). By means of a linear interpolation the physical value of the pressure in the axial air supply is obtained and displayed on the front panel of the "Main_Grab_Signals.vi" routine.

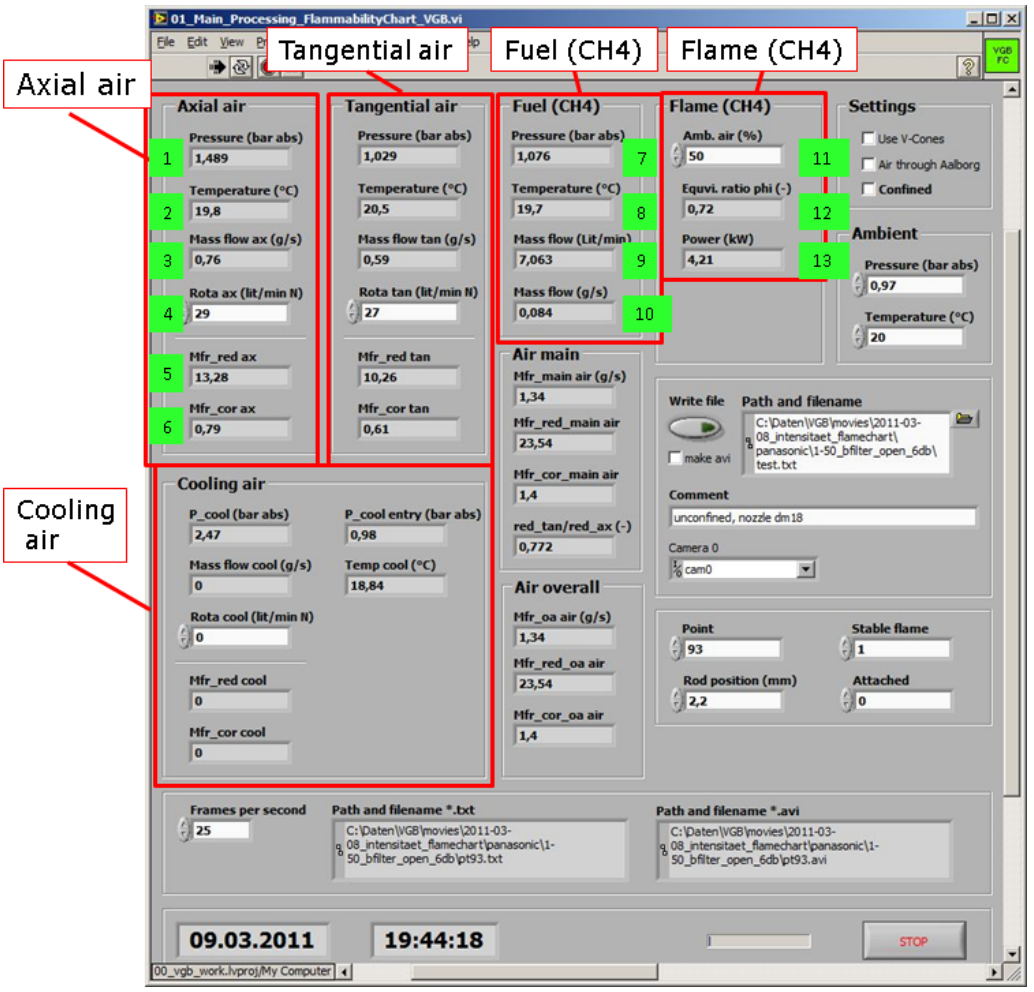

Figure 4.21: "Main_Processing.vi" LabVIEW routine for monitoring the instrumentation values of the test rig and further process parameters

Fig. 4.21 shows the front panel of the LabVEW routine "Main_Processing.vi". This LabVIEW routine provides various features. On the left top parameters of the axial air are displayed. The received pressure (1) in bar, temperature (2) in °C are monitored. With the manual setting of the current volume mass flow (4), according to the displayed value of the rotameter the mass flow of axial air (3) is interactively evaluated and monitored according to the parameters. The reduced (5) and corrected mass flow (6) is evaluated and monitored. Similarly, tangential and cooling air are displayed. The values of the fuel mass flow (CH_4) are obtained directly from the connected fuel mass flow meter (9) and the representative equivalence ratio ϕ (12) and the power (13) is obtained according to the ambient conditions (confined / unconfined) (11). Further settings of the measurement instruments (for example:

settings of the camera) can be adjusted and additionally stored for further evaluation.

4.4 Measurement uncertainties

The measurement error of the pressure transducers is less than 0.2 % of the characteristic curve. The errors of the temperature sensors and the fuel mass flow meter are $\pm 0.5\,K$ and $\pm 1\,\%$ FS respectively. The air mass flow meters meet the requirements for the VDI/VDE 2.5 class. The error of the input module NI 9203 is within $\pm 0.5\,\%$ of the characteristic curve [3].

4.5 Operating conditions

The tests were carried out at atmospheric conditions. The supply temperatures for main and cooling air and also for the fuel were kept at room temperature. Investigations were carried out with and without flame tube. The highest thermal power was 7.5 kW and the largest reduced mass flow was around 100 g/s $K^{0.5}$ / bar.

4.5.1 Reduced mass flow

The necessary operating parameters for determination of the mass flow can be derived from the ideal gas equation Eq. 4.10. Thereby, it can be seen, that with measurement of pressure p, volume flow rate $\dot{V}$, and temperature T (R, the gas constant has a value of 287 J/kgK for air and 518,8 J/kgK for methane)the mass flow $\dot{m}$ can be finally determined.

$$p \cdot \dot{V} = \dot{m} \cdot R_{air} \cdot T \tag{4.10}$$

The reduced mass flow is an important characteristic value. Especially in case of compressors the reduced mass flow is an indespensable setting parameter. The reduced mass flow supports the essential possibility of adjusting the same operating point under different application conditions (variation of temperature and pressure). A compressor map (pressure ratio π over reduced mass flow $\dot{m}_{red}$) provides vital information for operating the compressor in the right operating range, especially to prevent stalling [6].

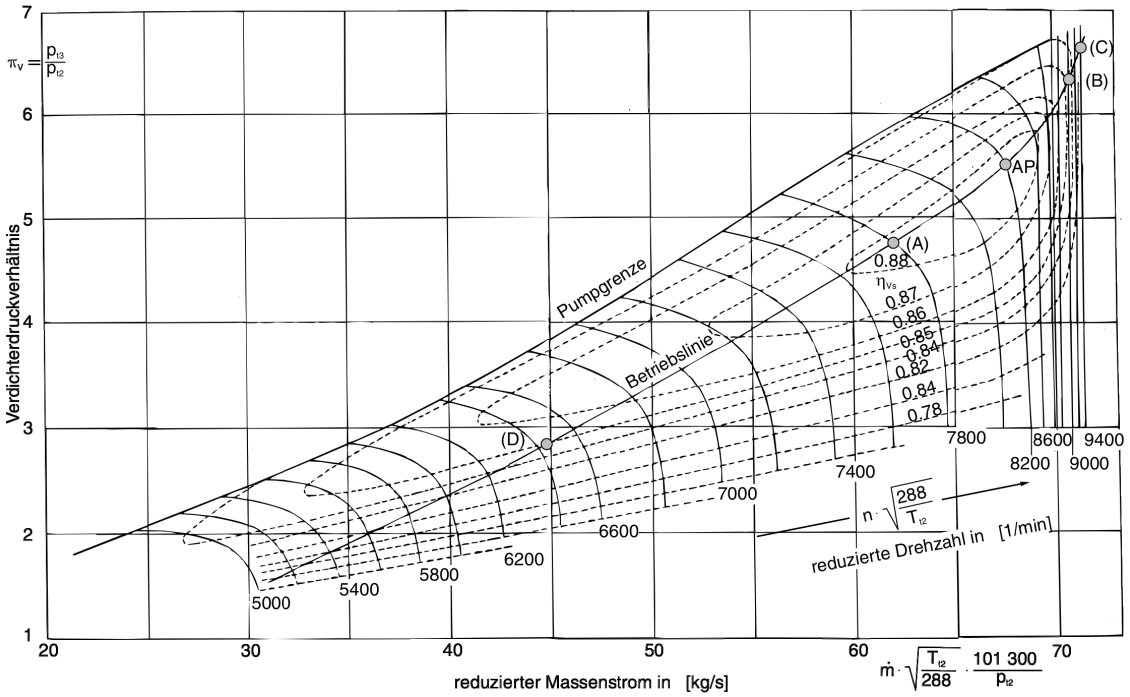

Figure 4.22: Compressor map, pressure ratio π over reduced mass flow $\dot{m}_{red}$ [6]

For the variable geometry burner test rig the same operating points could be adjusted by the reduced mass flow if a pressure loss in the air feed leads to changed settings.

The reduced mass flow, beside the change of the pressure (p_1, p_2) also considers temperature variation (T_1, T_2). The reduced and corrected mass flow is obtained by the Mach similarity (Eq. 4.11). Thereby Ma is the Machzahl, c the velocity and a the sound velocity which is determined with $a = \sqrt{\kappa \cdot R \cdot T}$ ($\kappa = c_p/c_V$ isotropic exponent is the ratio of isobar heat capacity to isochor heat capacity, R gas constant and T the temperature).

$$\text{Mach similarity:} \qquad \text{Ma}_1 = \left(\frac{c}{a}\right)_1 = \left(\frac{c}{a}\right)_2 = \text{Ma}_2 \tag{4.11}$$

With the determination of the velocity v through the general continuity equation, whereby velocity is determined as mass flow divided by density and cross section ($c = \dot{m}/(\rho \cdot A)$) and the ideal gas equation $\rho = p/(R \cdot T)$ the reduced mass flow can be determined (Eq. 4.14). Additionally, the unitless corrected mass flow is obtained according to Eq. 4.15 [23]. The corrected mass flow is referred to standard conditions ($p_o = 1{,}01325\,\text{bar}$, $T_o = 288{,}15\,\text{K}$ [23]).

$$\frac{\dot{m}_1}{\rho \cdot A \cdot \sqrt{\kappa \cdot R \cdot T_1}} = \frac{\dot{m}_2}{\rho \cdot A \cdot \sqrt{\kappa \cdot R \cdot T_2}} \tag{4.12}$$

$$\frac{\dot{m}_1}{\frac{p_1}{R \cdot T_1} \cdot A \cdot \sqrt{\kappa \cdot R \cdot T_1}} = \frac{\dot{m}_2}{\frac{p_2}{R \cdot T_2} \cdot A \cdot \sqrt{\kappa \cdot R \cdot T_2}} \tag{4.13}$$

with: $R, A, \kappa = konst.$

$$\dot{m}_1 \cdot \frac{\sqrt{T_1}}{p_1} = \dot{m}_2 \cdot \frac{\sqrt{T_2}}{p_2}$$

Reduced mass flow: $$\dot{m}_{red} = \dot{m} \frac{\sqrt{T}}{p} \tag{4.14}$$

Corrected mass flow: $$\dot{m}_{cor} = \dot{m} \frac{\sqrt{T/T_o}}{p/p_o} \tag{4.15}$$

Purpose of this operation is to obtain a comparable quantity, because test series were carried out at different times. Accordingly, the ambient conditions could have changed. Especially due to the pressure loss in the seeding generator for the PIV measurements a comparable operation value was required for a proper adjustment of the burner operation settings. The corrected mass flow is a value referred to the normal temperature $T_o = 25\,^{\circ}\mathrm{C} = 273{,}15\,\mathrm{K}$ and the normal pressure $p_o = 1{,}01325\,\mathrm{bar}$ (NTP: **n**ormal **t**emperature and **p**ressure [24]). Hence, a parameter independent of the ambient conditions is obtained. The necessary operating parameters were measured in a supply line right before the entry of air in the variable geometry burner.

4.5.2 Equivalence ratio

The air to fuel ratio (AFR) is defined as the air mass flow entering the combustor in relation to the injected fuel mass flow. The equivalence ratio ϕ is the ratio of AFR_{st} (Air to fuel ratio in a stoichiometric (ideal) combustion) relative to the AFR in the test and was calculated according to Eq. 4.16. For a stable combustion a supply of secondary air was required. Therefore 50% of the ambient air at unconfined or 50% cooling air at confined conditions were defined for reacting in the combustion process.

$$\phi = \frac{AFR_{st}}{AFR} \tag{4.16}$$

4.5.3 Power

The thermal power $\dot{Q}$ is supplied by the fuel. The measured power was determined according to Eq. 4.17. The mass flow of the fuel (CH_4) $\dot{m}_{CH_4}$ was detected by the mass flow meter from Aalborg and the heat value of methane H_{CH_4} is 50,53 MJ/kg.

$$\dot{Q} = \dot{m}_{CH_4} \cdot H_{CH_4} \tag{4.17}$$

Chapter 5

Measurement techniques

Today non-intrusive flow measurement techniques are state of the art. They provide several advantages and new possibilities. The measurement doesn't have an effect on the gas flow. So the results reflect in a appropriate way the actual characteristics of the sensitive gas flow. Especially in a combustion, with it's hot temperatures, it is possible to get a detection without suffering of the measurement material. In the technical combustion, especially for new concepts of combustion chambers, it is important to investigate the stability, the energy spectrum and the fluctuations of the flame, indicative of pulsations and moreover to vibrations in the combustion chamber, which can lead, in worst case, to a breakdown of the turbine. This significant and important facts about a flame can be detected with non-intrusive measurement technique.

In this work some of these measurement techniques have been used in context of the variable geometry burner and are explained in more detail in the following.

5.1 Schlieren visualization

5.1.1 Fundamentals of Schlieren visualization

This optical method is typically employed to get an overview impression of the investigated gas flow. Nevertheless the measurement can be enhanced with additional measurement instrumentations to achieve also a qualitative analysis.

Schlieren are gradient density disturbances of transparent media [25]. The Schlieren method is explained on the basis of the wave character of light, which undergoes propagation delay or deflection through media with different refractive index (Fig. 5.1). Projected on a screen,this leads to the presentation as bright or dark fields for the observer.

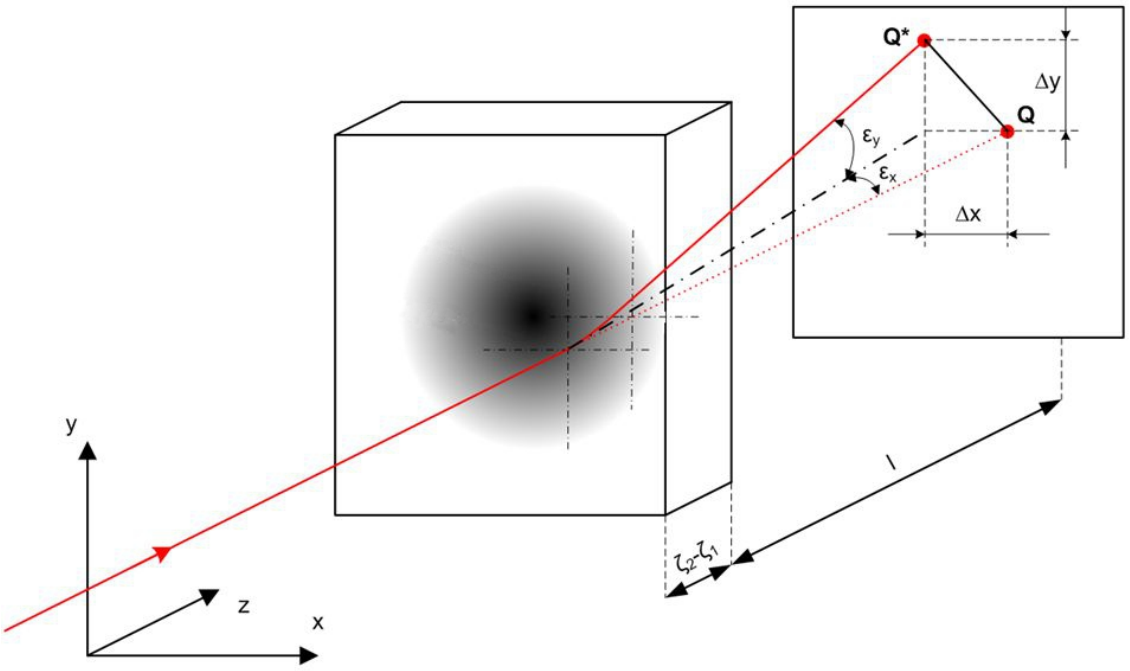

Figure 5.1: Beam deflection in a field with variable refractive index [26]

Light is characterized by the wavelength λ and the frequency f. Wavelength and frequency are related to the speed of light, which has a value of $c_o = 2,998 \cdot 10^8$ m/s in vacuum. In media the propagation of speed of light is slowed down.

$$c_o = f \cdot \lambda \iff c_m = f \cdot \lambda_m \tag{5.1}$$

The refractive index $n_o = \frac{c_o}{c_m}$ is a factor for the reduction of the speed of light. Some values of the refractive indexes for some gases are listed at the site of **National Physical Laboratory** (NPL) [27]. Hence, the refractive index of air, relative to a vacuum is n = 1.000292 at standard conditions. The **s**tandard **t**emperature and **p**ressure (STP) are p = 1,01325 bar at a temperature of T = 0 °C = 273,15 K [24]. The relationship between refractive index n and gas density ρ is defined by:

$$n - 1 = k \cdot \varrho \tag{5.2}$$

The Gladstone Dale coefficient k for air at standard conditions is $0.23 cm^3/g$ [25].

The bending of light rays through inhomogeneous media is proportional to the gradients of the refractive index. The resulting curvature of rays are described by:

$$\frac{\partial^2 x}{\partial z^2} = \frac{1}{n}\frac{\partial n}{\partial x},\ \frac{\partial^2 y}{\partial z^2} = \frac{1}{n}\frac{\partial n}{\partial x} \tag{5.3}$$

The location of the coordinate system in a Schlieren measurement can be seen in Fig. 5.1. So the z-axis is the direction of undisturbed rays. The x- and y- axis build planes perpendicular to the normal z-direction. Once integrated, the components of the angular ray deflection in the x- and y- directions are defined :

$$\varepsilon_x = \frac{1}{n}\int \frac{\partial n}{\partial x}\partial z,\ \varepsilon_y = \frac{1}{n}\int \frac{\partial n}{\partial y}\partial z \tag{5.4}$$

For two dimensional Schlieren of extension L along the optical axis, the result is:

$$\varepsilon_x = \frac{L}{n_o}\frac{\partial n}{\partial x},\ \varepsilon_y = \frac{L}{n_o}\frac{\partial n}{\partial y} \tag{5.5}$$

5.1.2 Setup for Schlieren visualization

The first test performed used the Schlieren visualization to get a qualitative impression of the distribution of the density gradients of the burner flame. The principle of Schlieren visualization, is explained in Sec. 5.1.1. A schematic of the test assembly is shown in Fig. 5.4. The description of the items are listed in Tab. 5.1.

For the light source a slide projector was used. Right in front of the light source a filter was positioned. Two different kind of filters were employed. To achieve better contrast for the camera system used a dark filter was necessary. And to realize visibility of turbulence fluctuations, in order to get a classical Schlieren visualization, a Schlieren filter had to be fixed. In each case the value of the exposure time of the video camera had to be adjusted. So in case of the Schlieren filter 1/8000 s exposure time was chosen and in case of the additional dark filter the value of 1/50 s was set. With the flame the density gradients were so strong that the camera aperture itself acted as Schlieren filter, so no additional Schlieren filter was needed.

In a pinhole aperture the light beam was focused and further on deflected through a plane mirror on to the first parabolic mirror. The parabolic mirror had a focal length of 2032 mm. To achieve a parallel light beam the distance between the pinhole aperture to the parabolic mirror had to equal this focal length. For the first adaptation a flexible measuring tape was used. The pinhole aperture was on a slide for positioning. For the exact adjustment a blank sheet of paper was used as a tool to detect the focal distance and also to assure full exposure of the parabolic mirror.

The parabolic mirrors were fixed above the laboratory desk in a height such that the cone shape of the burner flame was in the center from the parabolic mirror. The second parabolic mirror and further on the second plane mirror were placed

symmetrical to the burner at the same distance to position the image plane to the video camera.

The Panasonic video camera of type NV-DX100EG is shown in Fig. 5.2. The video camera was fixed on a tripod and connected to a monitor. For the horizontal adjustment the cover plate of the burner was used as reference. For fine adjustment the focus of the video camera was set to get a clear Schlieren display picture.

Figure 5.2: Video camera panasonic type NV-DX100EG

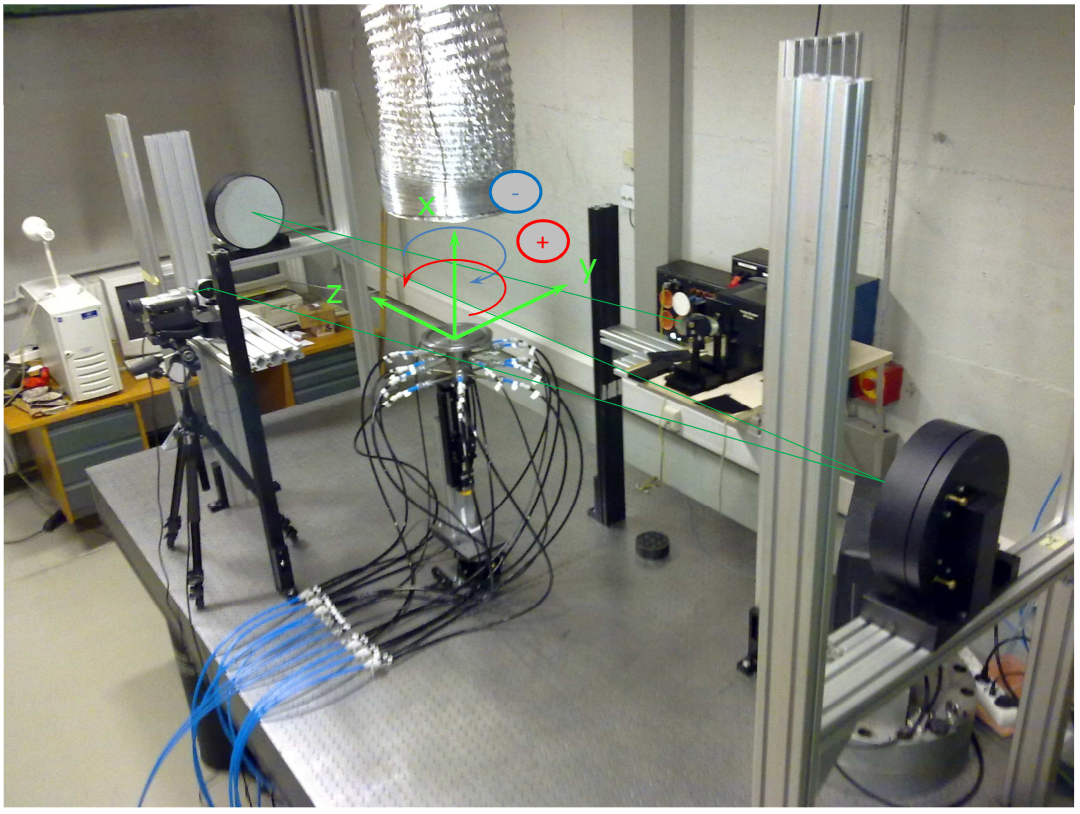

Figure 5.3: Assembly of the Schlieren visualization

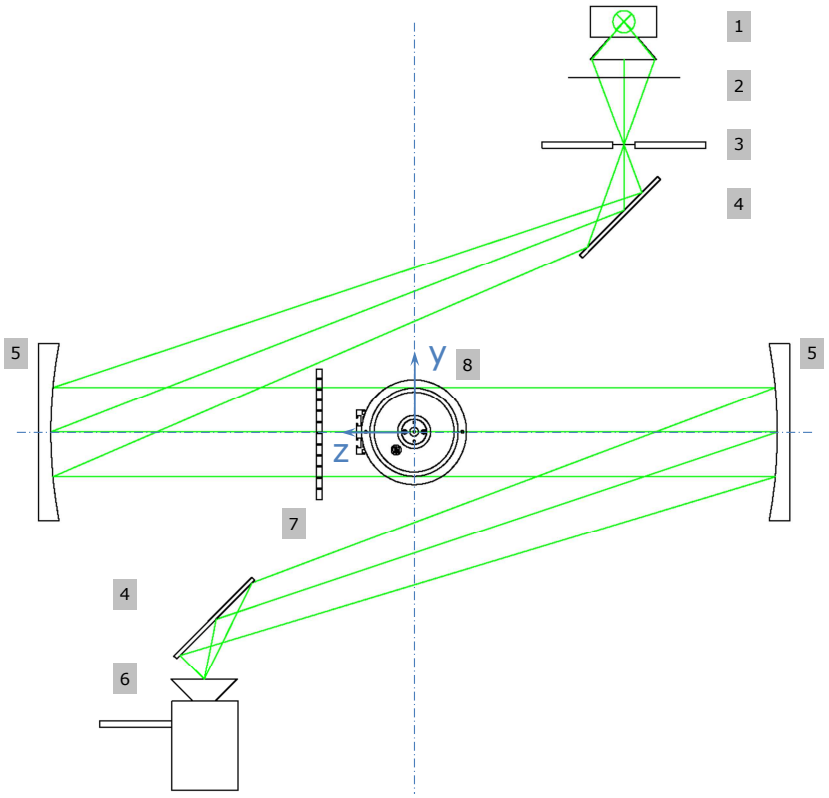

Figure 5.4: Scheme assembly of the Schlieren visualization (bird's eye view)

Table 5.1: Parts list for Schlieren visualization

Pos.	Description
1	light source
2	light filter
3	pinhole aperture
4	plane mirror
5	parabolic mirror
6	video camera
7	stripe pattern unit
8	variable geometry burner

Fig. 5.5 shows the test assembly including fuel and air supply for the measurements of Schlieren visualization and Background Oriented Schlieren method (BOS). The measurements were performed under unconfined conditions. Tab. 5.2 shows the components of the test rig for these measurements.

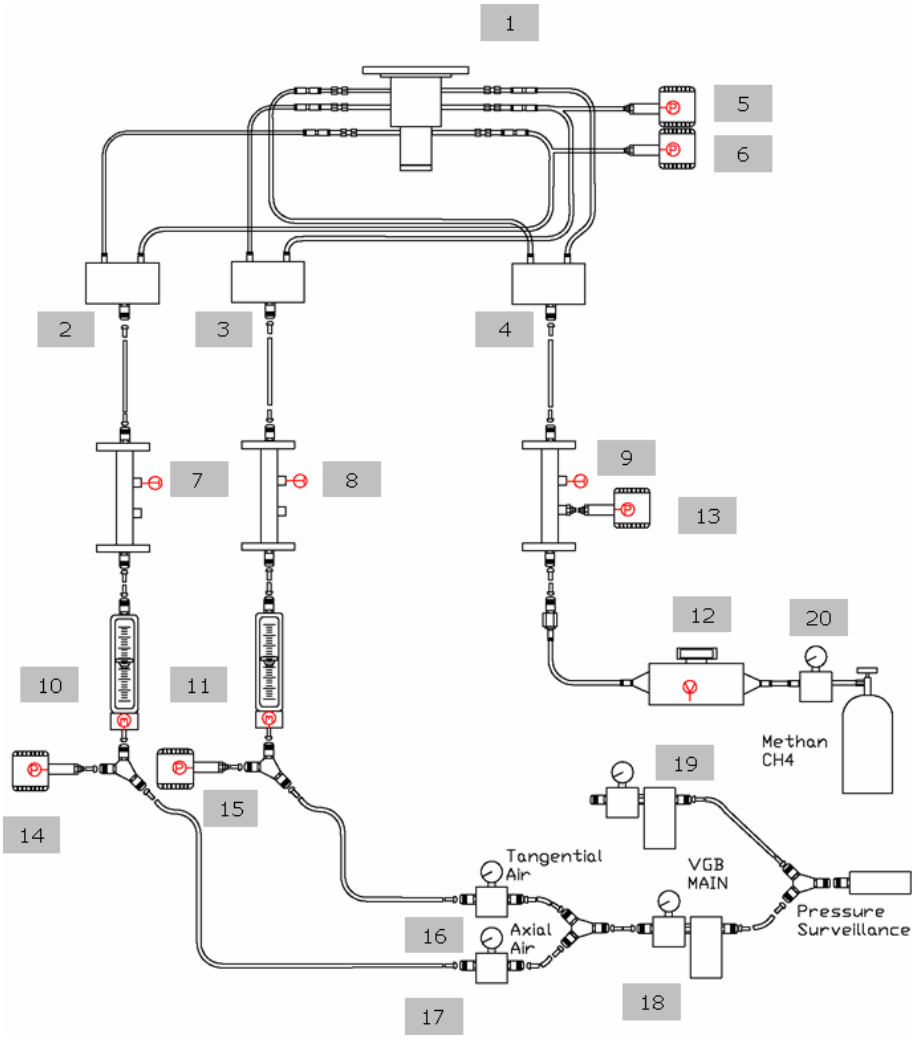

Figure 5.5: Test assembly with instrumentation for Schlieren visualization and Background Oriented Schlieren method (BOS)

Table 5.2: Component description of the test rig for Schlieren visualization and Background Oriented Schlieren method (BOS)

Pos.	Description
1	burner
2-4	distribution boxes
5-6	pressure transducers
7-9	temperature sensors
10-11	air mass flow meters
12	fuel mass flow meter
13-15	pressure transducers
16-19	control valves main air
20	control valve fuel

A resulting example is shown in Fig. 5.6. Fig. 5.6a was recorded with an exposure time of 1/50 sec, which reveals the characteristic blue intensity of the flame together with the density gradients, while Fig. 5.6b shows the density gradients. For further details see [3].

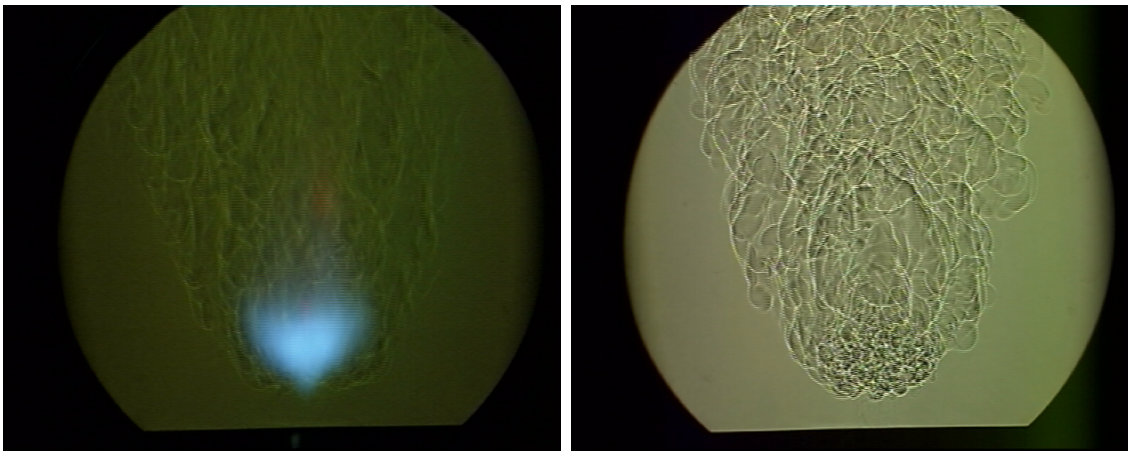

(a) Schlieren visualization (1/50 sec) (b) Schlieren visualization (1/8000 sec)

Figure 5.6: Schlieren visualization

5.1.3 Setup for Background Oriented Schlieren method (BOS)

To obtain a quantitative figure for the distribution of the density gradients the assembly was extended,as shown in Fig. 5.7, by insertion of a transparent frame with a regular grid pattern right in front of the burner which provides a set of fringes for Schlieren evaluation in the image plane. This straightforward extension of the Schlieren visualization setup for the determination of the density gradient distribution provides ease of implementation. In comparison to more elaborate measurements, like differential interferometry, only density gradients are provided since further parameters are necessary for a subsequent integration to determine the density distribution.

The pattern unit consists of a 276x195 mm transparent foil with 1 mm wide vertical stripes separated by 2 mm. In this arrangement the stripes provide a grid pattern deflected by the density gradients of the flame in the image plane. The pattern unit was arranged in vertical position (Fig. 5.7). The pattern was positioned relative to the burner for obtaining a clear image exhibiting the grid deflection with a minimum of disturbance (a local large distortion can lead to loss of information due to grid disruption). For the evaluation a reference picture of the undisturbed measurement target (without flame) is required for deleting optical disturbances due to the measurement platform.

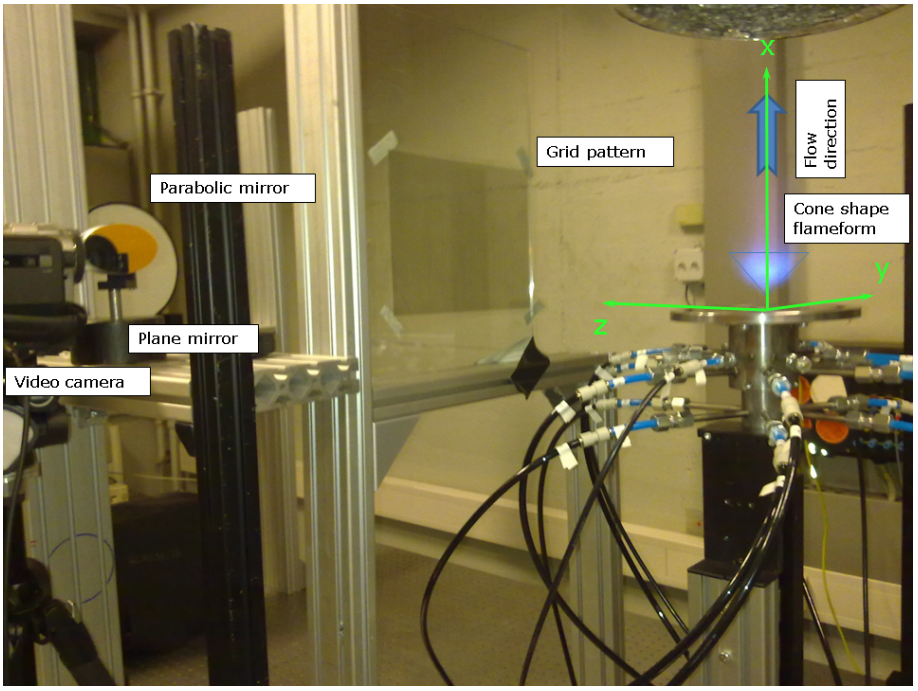

Figure 5.7: Extension of the Schlieren visualization with a grid pattern

5.1.4 Measurement evaluation of Background Oriented Schlieren method (BOS)

The theory of the fringe evaluation is based on the same principals as the differential interferometry (Chap. 5.2.1). So the evaluation followed the same scheme as in case of differential interferometry (Chap. 5.2.3). The deflection provides a representative expression for the density gradients after processing the recorded image information with the software routines on the basis of Matlab and IDEA. For the evaluation the same routines as in the evaluation of the differential interferometry were employed. Thereby the videos were separated into their frames, which were formatted into the size of 512x512 pixel, transformed to the corresponding grayscale components and saved as a bitmap file. From this data the density gradient distribution was evaluated with a processing routine on the basis of software IDEA [28]. The steps of the performed evaluation in the software program IDEA are shown in Fig. 5.8 for records with flame and in Fig. 5.9 without flame. The detailed evaluation in the software IDEA is described in Chap. 5.2.3. A tomographic reconstruction followed, performed also with the software IDEA.

Fig. 5.10 shows the visualized density distribution across the flame field evaluated from one frame. The blue color symbolizes the negative gradient and the red color the positive gradient. It reveals that the correct detection of the information of the flame was not fully provided. The density gradient distribution derived in this manner, was not sufficiently conform to the principles of density distribution. (Fig. 5.11). A possible reason might be found in the observed strong disturbances in the distortions of the deflection image of the interference fringes which leads to a loss of

information or incorrect data for the subsequent processing routines in deriving the density gradient distribution for the measurement target. Remedy can be sought in adjustment of the interference fringes pattern sensitivity by modifying the geometry of the frame stripe structure (stripe width and period). In this case the further work was based on the approach with differential interferometry.

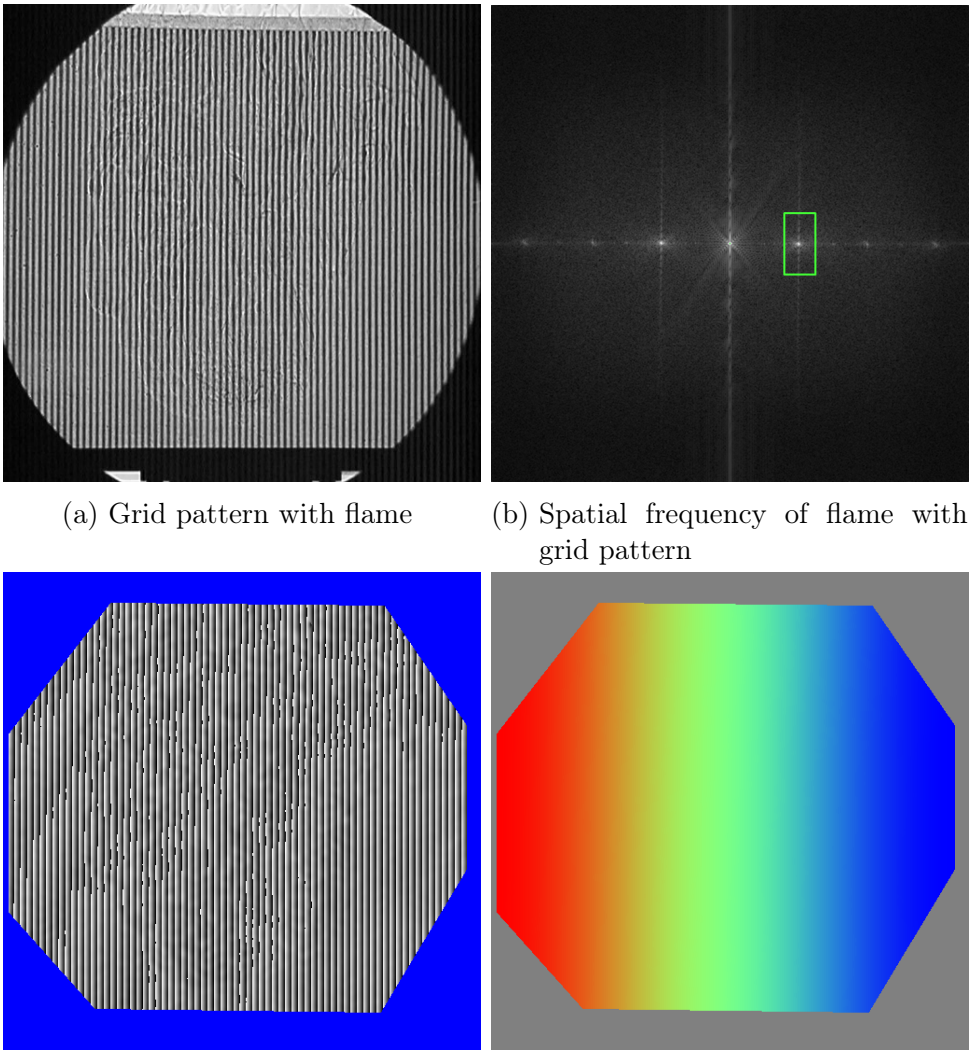

(a) Grid pattern with flame

(b) Spatial frequency of flame with grid pattern

(c) Modulo 2π of flame with grid pattern

(d) Phase gradient distribution of flame with grid pattern

Figure 5.8: IDEA evaluation for records of the flame with the grid pattern (a)-(d)

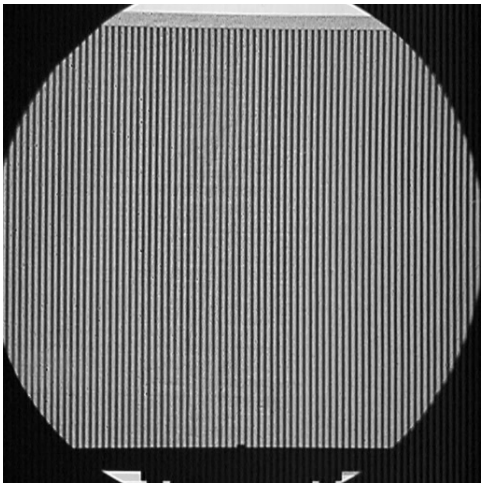

(a) Grid pattern without flame

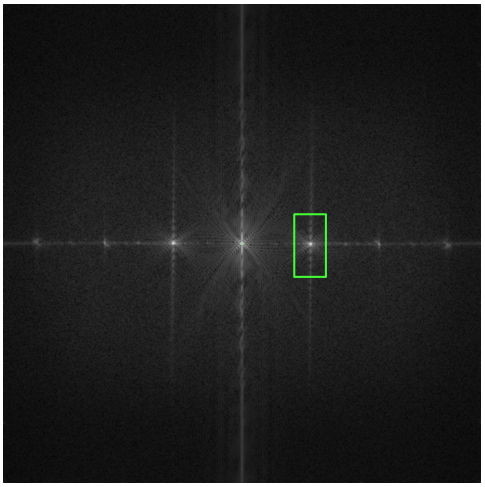

(b) Spatial frequency of reference without flame

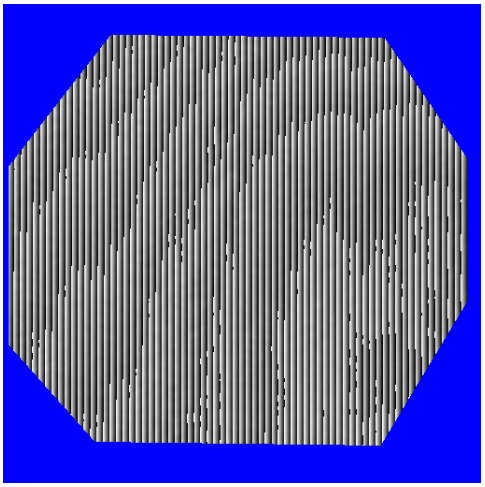

(c) Modulo 2π of reference without flame

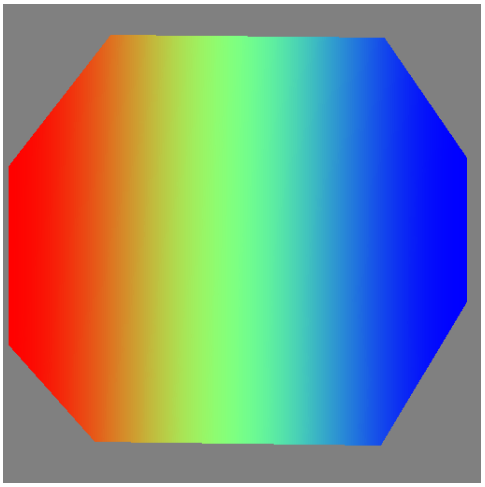

(d) Phase gradient distribution of reference without flame

Figure 5.9: IDEA evaluation for records without flame (a)-(d)

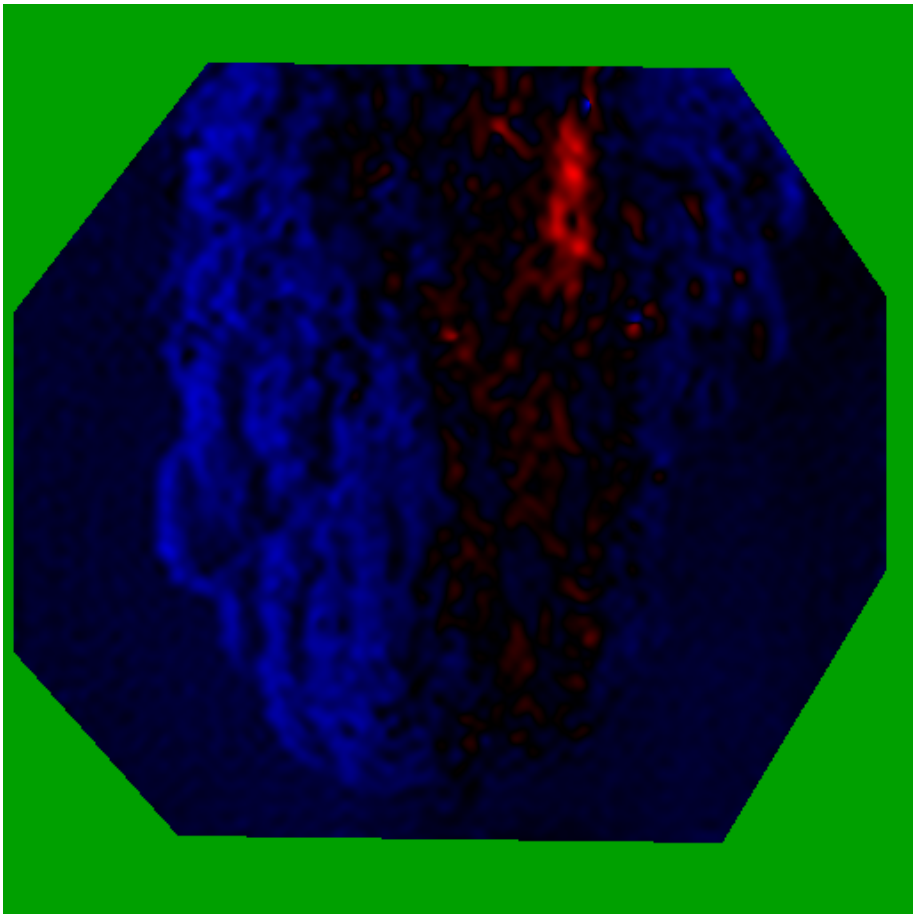

Figure 5.10: Density gradient distribution visualized in IDEA in the flame field (blue symbolizes negative gradients, red symbolizes positive gradients)

5.2 Differential interferometry

5.2.1 Fundamentals of differential interferometry

Differential interferometry is based on the interference of coherent light waves with quantification of delay variation in transparent media. In coherent light the light waves have the same phase relation throughout the light beam cross section. Basic interferometry setups usually employ a coherent light beam emitted by a laser, which is passed through the transparent measurement media, thereafter split into equal halves, shifted against each other (sheared), and finally superimposed again. According to the resulting phase shift an interference arises. The resulting phase shift originates from difference in geometric path as well as varying property of light propagation (differences of density and thereby refractive index). Therefore optical path includes geometrical path (z) as well as the refractive index of the media (n). The relationship between phase distribution and density distribution is given by Eq. 5.6, describing the optical phase according to the effective optical path along propagation direction z. With known wavelength (λ) and refractive index

distribution the phase distribution (Φ) can be derived from Eq. 5.6. The spatial coordinates x and y are normal to the light wave direction z. The Gladstone Dale constant (K) depends on the gas composition, temperature and wavelength. The Gladstone Dale constant (K) is considered to be constant over the operating range. A positive feature of this measurement is that the sensitivity of the interferometry can be individually adjusted appropriate to the property of the measurement object, by adjusting the value of shearing.

$$\Phi(x,y) = \frac{2\pi}{\lambda} \int (K\rho(x,y,z) + 1)dz \tag{5.6}$$

The differential interferometry provides the phase shift $\Delta\Phi$ between two adjacent light beams, slightly sheared, proportional to the density gradient of the propagation media. The direction of the shearing δ defines the gradient measurement direction. As shown in Fig. 5.11 the density curve across the burner flame leads to corresponding phase shift, shown in direction of the coordinate y. The relationship between the resulting phase shift and shearing over the optical path length is given by Eq. 5.7, therefore the shearing δ needs to be identified, to determine density gradient and density thereby.

$$\frac{\Delta\Phi(y)}{\delta} = \frac{2\pi}{\lambda} K \cdot \int \frac{\partial \varrho}{\partial y} dz \qquad for \quad \delta << 1 \tag{5.7}$$

The curves of the phase Φ and the phase derivative $\Delta\Phi$ over the operating field with varying refractive index is shown in Fig. 5.11. The phase curve, directly related to the density $\rho(x,y,z)$, has a maximum in the center. The maxima and the minima of the phase change (derivative $\delta << 1$) $\Delta\Phi$ reveal the localization of the largest density gradient.

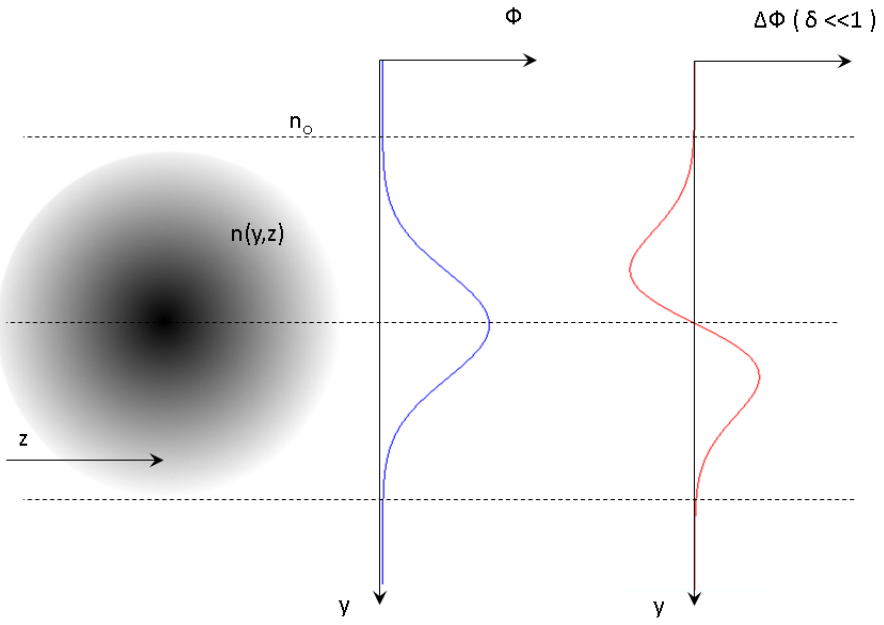

Figure 5.11: Distribution of the phase and the phase gradient

For the detection of the density itself a numerical integration of the density gradient in shearing direction needs to be performed. It needs to be noted that the value of the density gradient needs to be zero at the starting point of the integration. Therefore the measured field requires an undisturbed zone at the boundary.

5.2.2 Setup for differential interferometry

Most parts of the Schlieren setup were adopted for the differential interferometry setup. The light source for the coherent light beam in this case wa a HeNe Laser with a power of 20 mW. The laser beam, with a wavelength of 632 nm, was focussed with a collecting lens (f = 5 mm, 20x microscope objective). Right in the focal point a pinhole with a diameter of 12,5 μm was placed. The position of the following plane mirrors and the parabolic mirrors were adopted from the Schlieren setup.

With consideration of the focal distance of the parabolic mirror (f=2032 mm) the interferometry unit, shown in Fig. 5.12b, was placed after the light waves pass through the burner flame measurement field and are concentrated again with the parabolic mirror onto the plane mirrors of the interferometer. The interferometry unit consists of two prism, which split the light beam into equal halves, and two plane mirrors provided with three calibrating screws, for tilting in all directions to adjust the shear δ value. An object with a sharp edge was placed on the burner in the operating field as a tool for the adjustment of the shearing δ. The shearing direction was positioned

normal to the fringe pattern. With covering alternating one or the other laser beam in the interferometry unit a shift of the contour of the placed object was recognized. This was used as a reference for determination of the shearing value δ adjusted according to the required sensitivity of the interference pattern (Fig. 5.12a). In the case of a large density gradient a low shearing was set and vice versa to prevent a too large deflection of the interference fringes. A loss of information due to a discontinuity in the interference fringes would lead to disturbance in the evaluation. Furthermore by tilting the prism combining the two beams a fringe pattern was superimposed as a reference for determination of the required phase information.

The differential interferometry setup was placed on a pneumatically damped support.

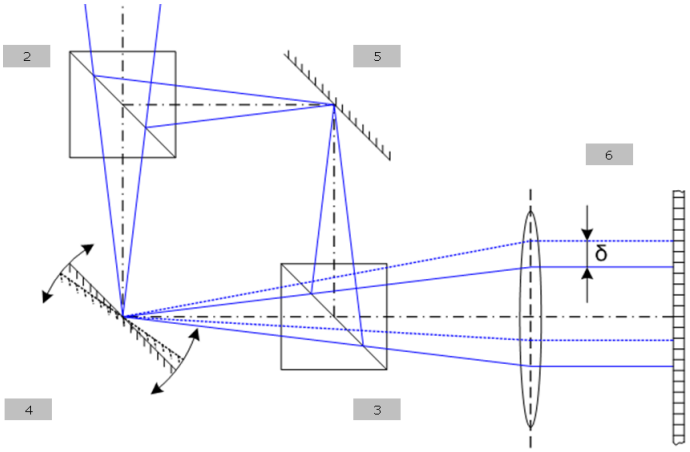

(a) Layout of interferometry unit with shearing δ [26]

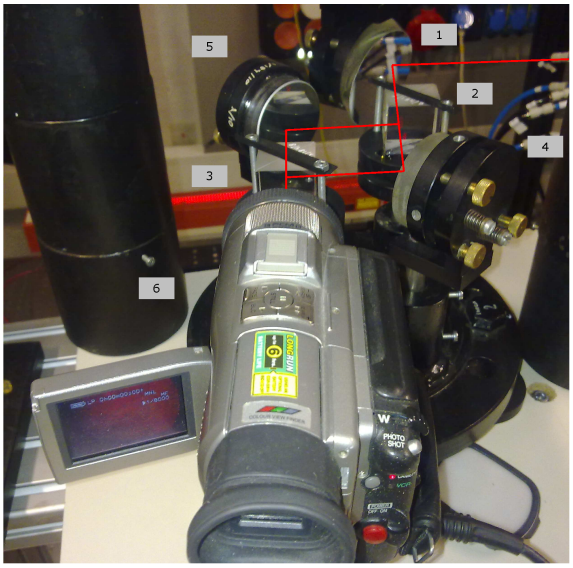

(b) Interferometry unit with video camera Panasonic NV-DX100EG

Figure 5.12: Interferometry unit

Table 5.3: Component description of interferometry unit

Pos.	Description
1	plane mirror
2-3	prism
4-5	plane mirror
6	video camera – Panasonic NV-DX100EG

For recording a video camera, Panasonic type NV-DX100EG was used. The exposure time was set to 1/8000 s. For tomographic reconstruction 400 frames were recorded, with the software Magix version 16, from each 10 ° direction. So 18 films, from position +90 ° to -80 °, had been taken for each operating point.

To determine the dimension of the measurement field, reference recordings were taken with a ruler placed horizontal and vertical on the burner in the measurement field. The location of the center axis was found with the rod driven out, visible in the operating field, used as a reference object.

A schematic of the test assembly is shown in Fig. 5.13 and the setup is shown in Fig. 5.14. The description of items are listed in Tab. 5.4.

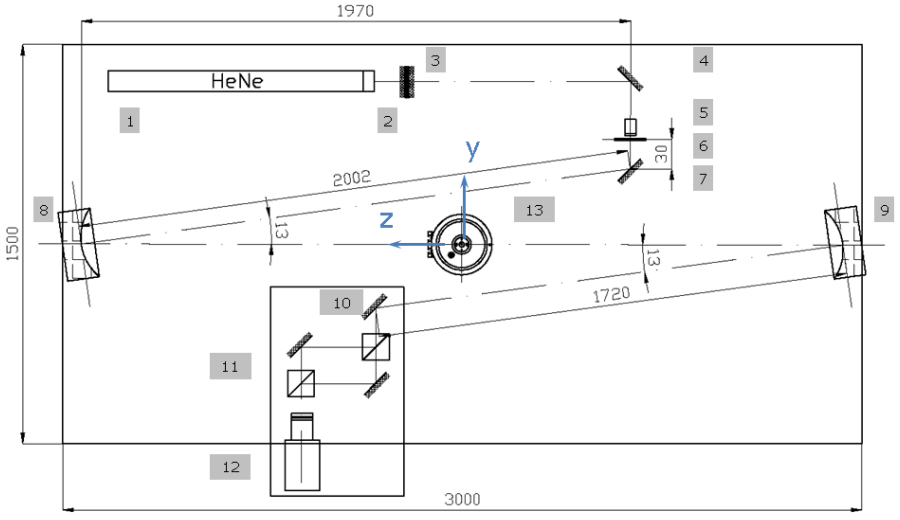

Figure 5.13: Layout for differential interferometry (bird's eye view)

Table 5.4: Component description of differential interferometry system

Pos.	Description
1	HeNe-Laser
2-4	plane mirror
5	collecting lens
6	pinhole aperture
7	plane mirror
8-9	parabolic mirror
10	plane mirror
11	interferometry unit
12	video camera – Panasonic NV-DX100EG
13	burner

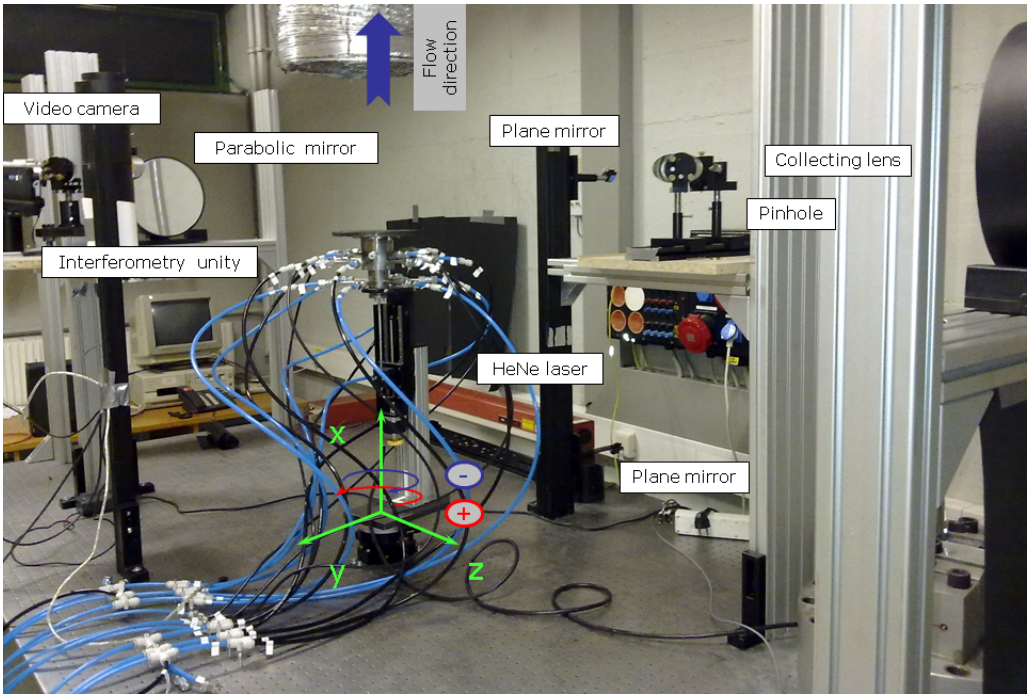

Figure 5.14: Setup differential interferometry, burner in position -80°

Fig. 5.15 shows the test assembly including fuel and air supply for the differential interferometry measurements. The measurements were performed under unconfined conditions. Tab. 5.5 shows the components of the test rig for these measurements.

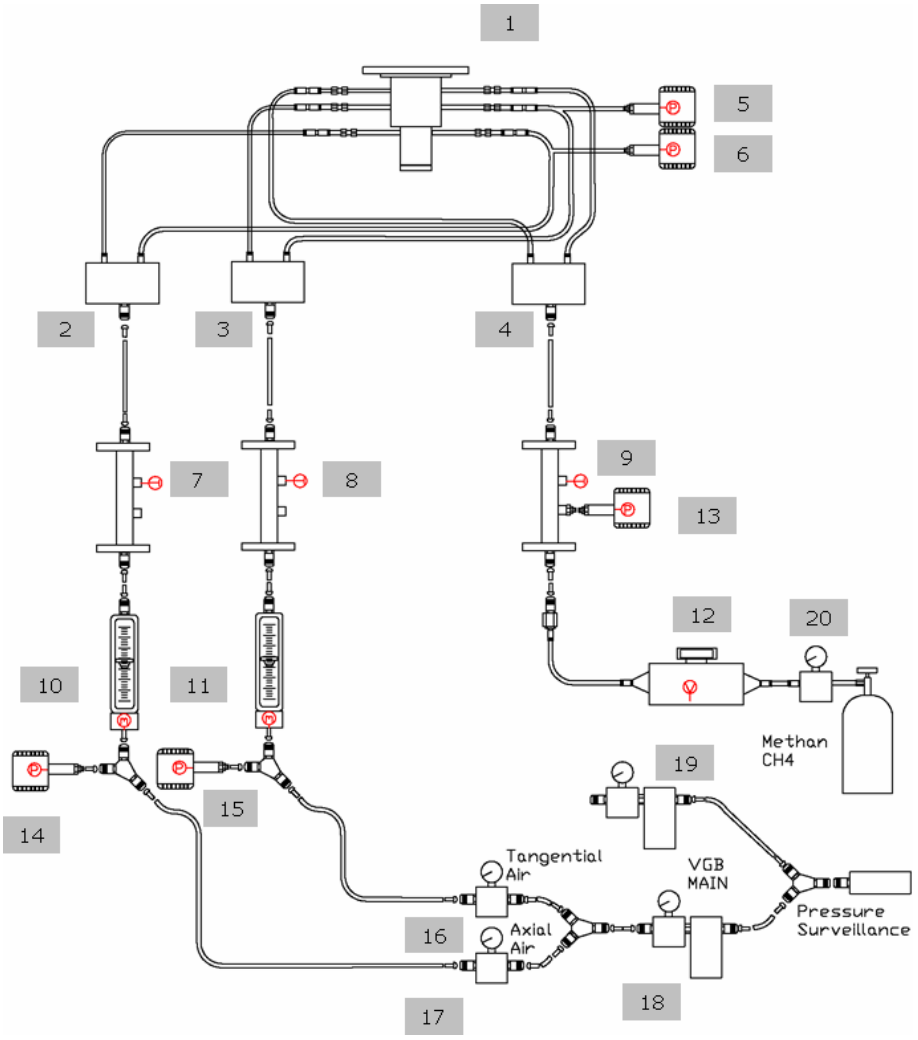

Figure 5.15: Test assembly with instrumentation for differential interferometry

Table 5.5: Component description of the test rig for differential interferometry

Pos.	Description
1	burner
2-4	distribution boxes
5-6	pressure transducers
7-9	temperature sensors
10-11	air mass flow meters
12	fuel mass flow meter
13-15	pressure transducers
16-19	control valves main air
20	control valve fuel

5.2.3 Measurement evaluation of differential interferometry

The recorded films were separated into their frames with a Matlab software routine and a scaling size of 512x512 pixel (Fig. 5.16a), which is necessary for the subsequent evaluation with software IDEA, because the fast Fourier transformation (FFT) demands a data set with exactly 2^n supporting points. To delete disturbances resulting from imperfection of the optic, like distortion of the wave front by lens defects, a reference image set without flame was evaluated next to operating records (Fig. 5.17).

The parallel interference fringes were modulated with the operating phase information $\Delta\Phi(x, y)$. In IDEA a fast 2D Fourier transformation identifies the spatial frequency spectrum (Fig. 5.16b). The zero order is placed in the center. The first order side lobe, including the relevant carrier fringe system modulated by $\Delta\Phi(x, y)$, is marked within the frequency spectrum. With filtering the relevant section the informative phase within the points of discontinuity of the arctan by $\pm\pi$ (jump discontinuity) is determined by processing back from the complex frequency function (inverse Fourier transform). The resulting Modulo 2π picture is shown in Fig. 5.16c. In a next step a special algorithm detects the discontinuity and the phase distribution with suppressed carrier (Fig. 5.16d). Subtraction of the reference picture without the flame yields the curve of the phase gradient, wich is proportional to the density gradient (Fig. 5.18).

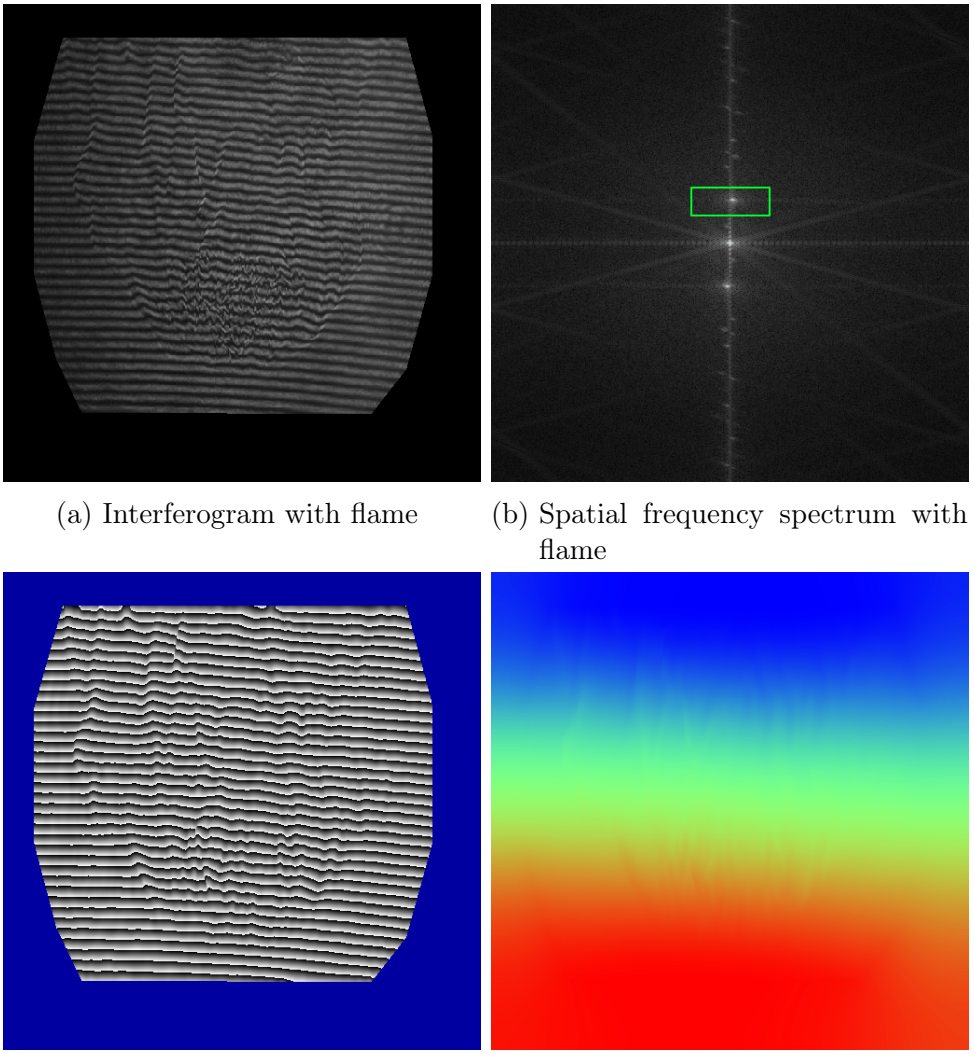

(a) Interferogram with flame

(b) Spatial frequency spectrum with flame

(c) Modulo 2π with flame

(d) Phase gradient distribution with flame

Figure 5.16: IDEA evaluation for records with the flame (a)-(d)

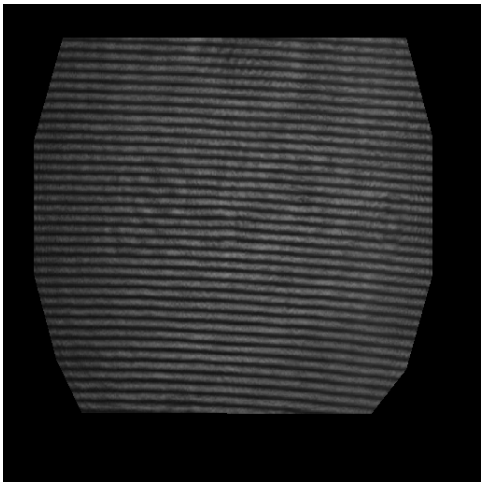

(a) Interferogram without flame

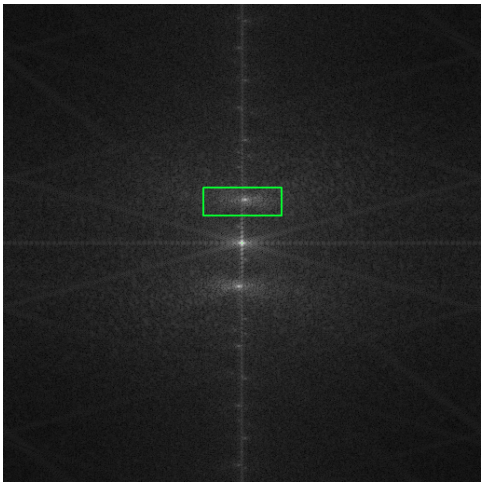

(b) Spatial frequency spectrum without flame

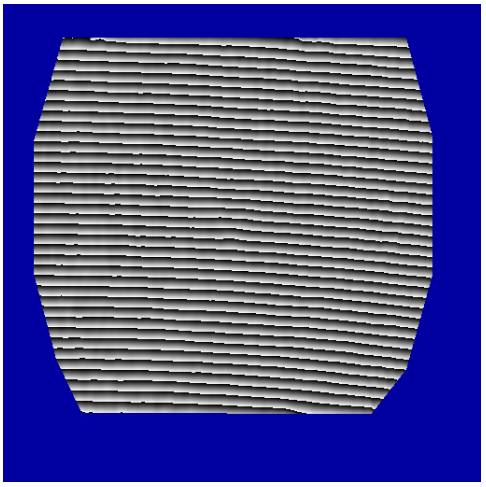

(c) Modulo 2π without flame

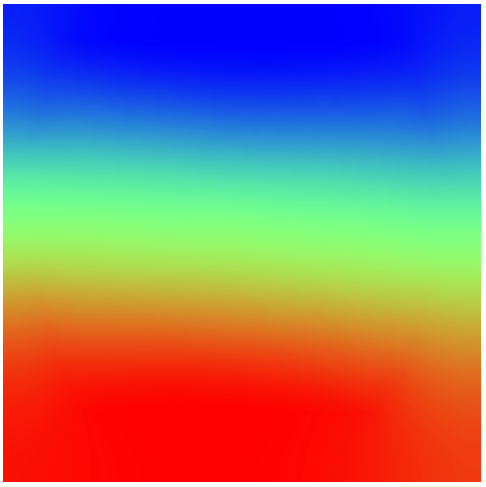

(d) Phase gradient distribution without flame

Figure 5.17: IDEA evaluation for records without the flame (a)-(d)

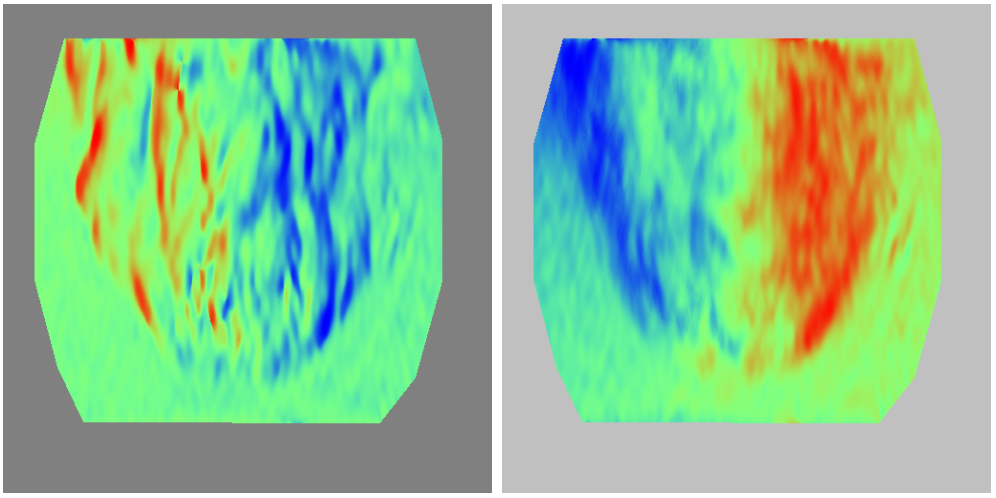

(a) Phase gradient distribution with tilt of one single frame

(b) Phase gradient distribution with tilt averaged over 400 frames

Figure 5.18: Phase gradient distribution with tilt

To determine the absolute density each row of a frame was integrated with the software program Matlab. The averaging was done for 400 frames. An appearing tilt could be eliminated by applying additional phase shifts in the software IDEA. In Matlab the tilt in each row, which resulted from defects in the optic was also corrected. With the 18 projections of the operating points a tomographic reconstruction was performed with software IDEA with selection of a relevant tomographic field. An interpolation was implemented to straighten the results. The density distribution was obtained from the phase information according to Eq. 5.7. Therefore, the required constants were determined according to the measurement conditions (shearing δ = 0,2299 mm, the wavelength λ = 632 nm and the Gladstone Dale constant K = 2,45*10exp-4 m^3/kg according to [29]). Fig. 5.19 shows a measured density distribution for a testing point, depicting surfaces of equal density (isosurfaces), for verification of the measurements. The measured density distribution corresponds to typical density distribution of a flame field. This shows that these measurement series provides a valid density distribution as aimed for. Further details are given in [3].

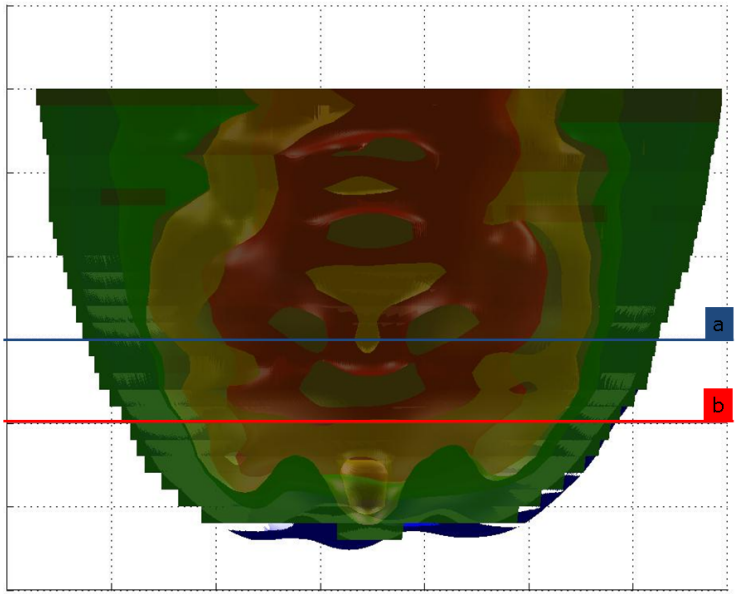

(a) Center Cut view of the flame field with density isosurfaces (blue = 0,7 kg/m^3, green = 0,38 kg/m^3, yellow = 0,28 kg/m^3, red = 0,15 kg/m^3)

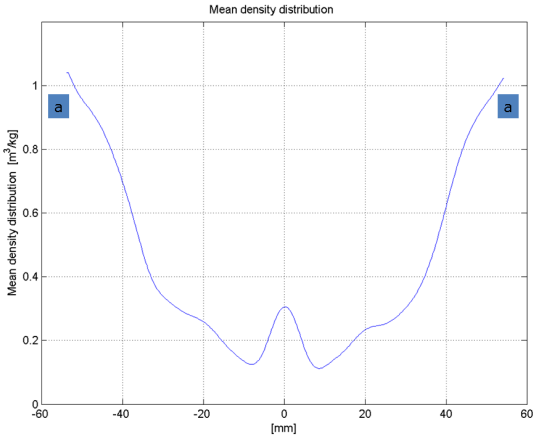

(b) Density distribution at height a (blue)

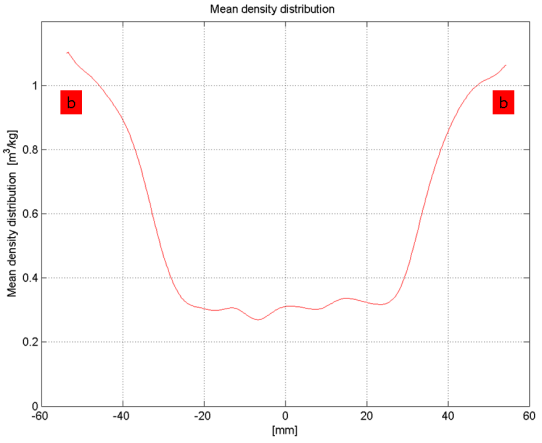

(c) Density distribution at height b (red)

Figure 5.19: Evaluation of the density distribution of a test point

5.3 Light emission

5.3.1 Fundamentals of light emission

Methane CH_4 reacts with oxygen O_2 to CO_2 and H_2O in a stoichiometric ratio $\varphi = 1$, representing an ideal combustion, see Eq. 5.8.

$$CH_4 + 2O_2 \longrightarrow CO_2 + 2H_2O \tag{5.8}$$

If the stoichiometric ratio deviates from $\varphi = 1$ byproducts arise, like Carbon monoxide (CO), Nitrates (NO_x) or soot, indicating incomplete combustion. From the reactants to the products a variety of transitional products emerge. Important transitional products of hydrocarbons(C_xH_y) are the CH^* radical, indicated by the characteristic blue intensity of the methane flame with a wavelength of 430 nm, the OH^* radical with a characteristic flame wavelength of 308 nm and the C_2^* radical, with a characteristic flame wavelength of 519 nm. ('*' symbolizes the unpaired electrons derived from the radical). In rich combustion the CH^* radical and the C_2^* radical (the characteristic green colour of the flame) are most common whereas in lean combustion the OH^* radical dominates [30]. The visible intensity of the flame is the electromagnetic radiation as a result of molecule transition to a lower energy state. The self absorption of the emitted radiation within the flame needs to be considered in quantitative intensity analysis.

The emission intensity of a molecule type is directly proportional to it's concentration.

An important aspect of intensity measurement is the detection of deviation of the intensity due to a periodic variation of heat release indicating density and pressure fluctuation. Such fluctuations show high frequency characteristic. The detecting camera requires appropriate setting of frames per second (fps) rate in order to quantify the fluctuations, indicative of instabilities in the flame.

The frequency spectrum of the detected fluctuation is evaluated with a Fourier analysis. The Fourier transformation of a signal is the correlation with the oscillation function $e^{-i2\pi ft}$. The function f(t) transformed to the frequency domain (Fourier domain) is defined as F(t). This transformation is reversible (Eq. 5.9).

$$G_t(f) = \int_{-\infty}^{\infty} g(t) \cdot e^{-i2\pi ft} dt \Leftrightarrow g(t) = \int_{-\infty}^{\infty} G_t(f) \cdot e^{i2\pi ft} df \tag{5.9}$$

The measurement provides a series of discrete values forming a digital time signal with a time period of Δt (supporting points). Therefore, a discrete Fourier transformation (DFT) needs to be applied. A mathematically optimized algorithm of discrete Fourier transformation is the commonly used fast Fourier transformation (FFT). Implemented in available software tools, such as in IDEA. This provides means of evaluating with filter functions.

In order to get local information, a tomographic reconstruction technique was used which is described in [31]. Thereby, the flame was captured from 18 directions, by rotating the burner in steps of 10 degrees. The method is schematically visualized in Fig. 5.20 and in Fig. 5.21.

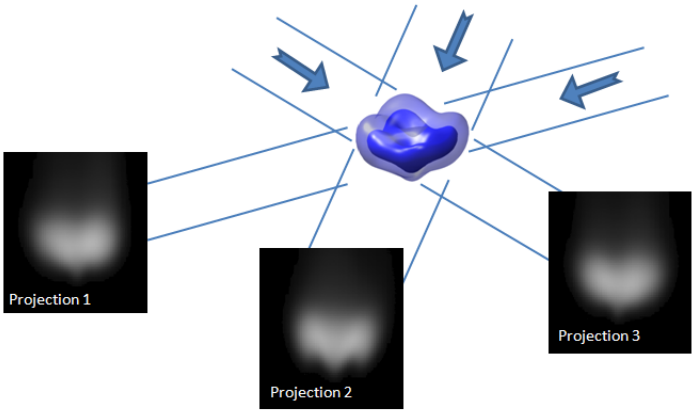

Figure 5.20: Projections of a flame [3]

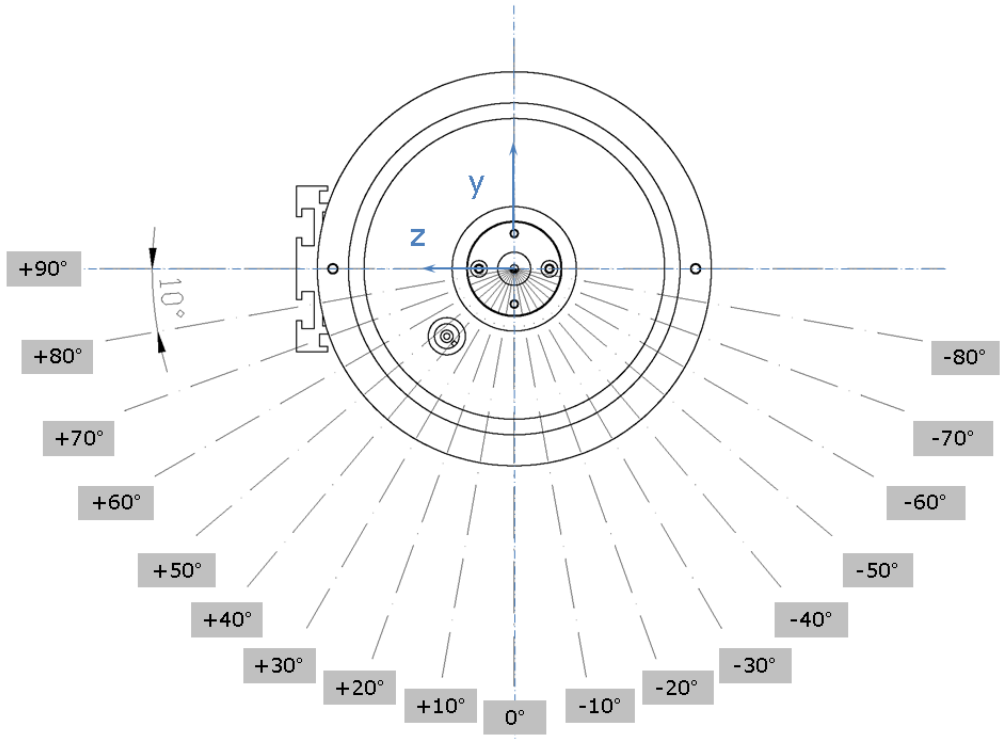

Figure 5.21: 18 projections for tomographic reconstruction

5.3.2 Setup for light emission

For the intensity records the video camera Panasonic type NV-DX100E was used. A schematic picture of the test assembly is shown in Fig. 5.22 The video camera was placed on a tripod in the distance of 1350 mm from the center of the burner flame. The height was set such that the cone shape of the burner flame could be fully detected with the video camera. A filter was added for selection of the CH^* emission. The reference for focussing was the top of the burner rod, which was driven out in positive x-axis. With the computer software magix version 16 the view of the top of the rod could be scaled up to 200 %. Focussing of the image was accomplished in iterative steps from both sides of the focus. For horizontal adjustment a tool with a straight edge was placed on the cover plate of the burner . With the comparison of a horizontal line the alignment of the video camera got checked with the aid of the computer software magix. By tilting the ruler the correct height of the video camera was verified. For evaluation reference pictures were made before every test cycle. With a ruler reference pictures with size dimensions for the horizontal and vertical axis were made. For the detection of the center axis the driven out burner rod was used as reference.

For the intensity test the emissions of the CH* radical, with a wavelength of 432 nm, in the flame were relevant. The blue filter from the firm Thorlabs type FGB25S (315-445 nm and 715-1095 nm) [32] faded out the non relative area of the flame. Hence, the blue filter was set right in front of the lens of the video camera. As

the sensor of the camera shows a nonlinear behaviour (Fig. D.1), all images were corrected with the characteristic of the sensor at the settings used. They can be found in Tab. 5.6

Table 5.6: Camera settings for light emission measurements

Description	Value
Exposure time	1/100 sec
Aperture	f/0.0
Gain	6 dB

For recording the video camera was set with 1/50 s exposure time and connected via firewire cable with the laptop. Because the flame was not symmetrical a video has been made with 100 frames from each 10 ° direction. The positive and negative sense of direction can be seen in Fig. 5.3 With the leveling unit the direction of the burner was set. So for each point 18 films from -90 ° to +90 ° were recorded.

The linear motor of the rod was actuated by means of the commercial software OWIS version 2.60. The linear motor had a gear ratio of 1 to 10000, which means for 1 mm 10000 moves were necessary.

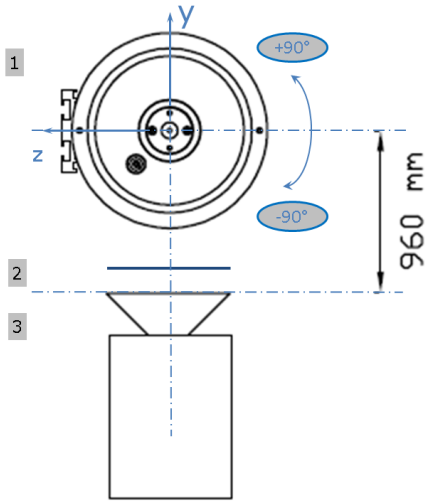

Figure 5.22: Layout for intensity measurements(bird's eye view)

Table 5.7: Component description of intensity system

Pos.	Description
1	burner
2	blue filter
3	camera

Fig. 5.23 shows the test assembly including fuel and air supply for the measurements of light emission. The measurements were performed under unconfined conditions. Tab. 5.8 shows the components of the test rig for these measurements.

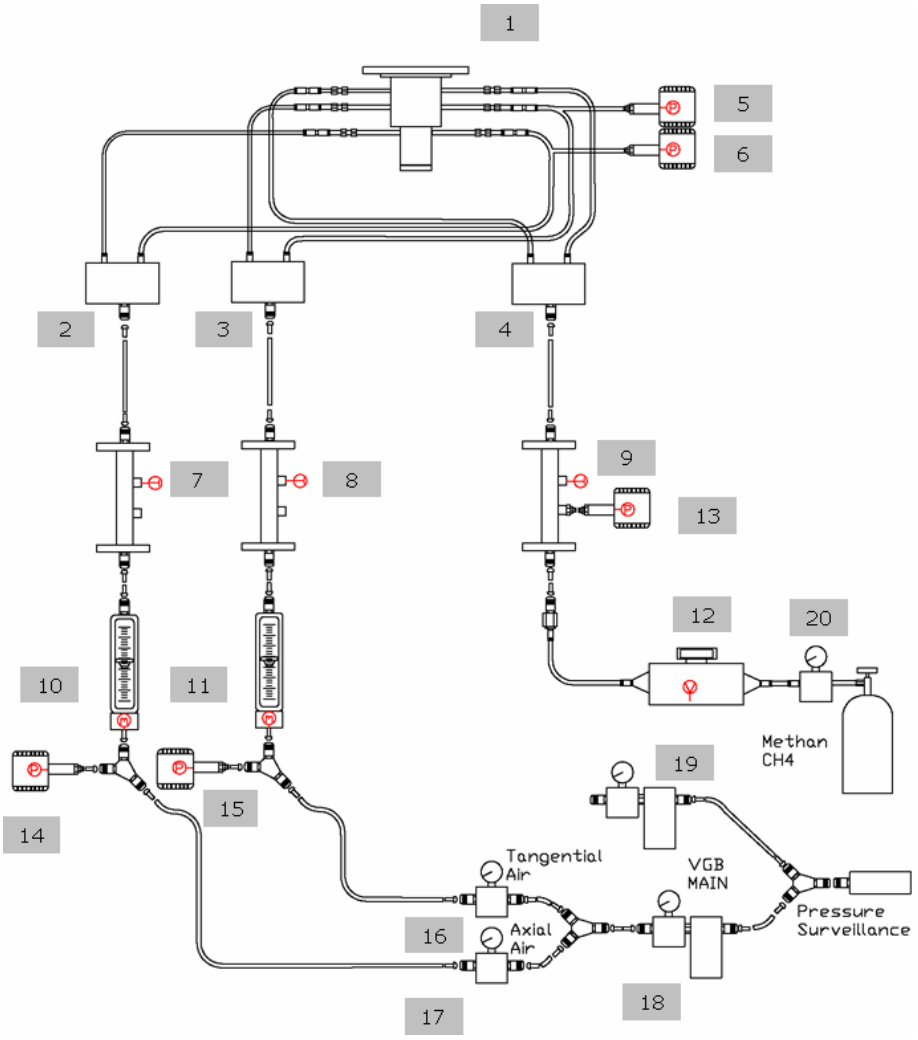

Figure 5.23: Test assembly with instrumentation for light emission

Table 5.8: Component description of the test rig for light emission

Pos.	Description
1	burner
2-4	distribution boxes
5-6	pressure transducers
7-9	temperature sensors
10-11	air mass flow meters
12	fuel mass flow meter
13-15	pressure transducers
16-19	control valves main air
20	control valve fuel

5.3.3 Measurement evaluation of light emission

With the same routine for the software Matlab the recorded films were separated into their frames with a scaling size of 512x512 pixel (required for the FFT routine of software IDEA) separated into the 3 basic colors (RGB). The blue color was representative for the CH^* radical, relevant for the flame evaluation. In a next step, also performed with the software Matlab, an average intensity value was determined. Parallel a Root Mean Square (RMS) average was accomplished (Fig. 5.24) representing the measure of fluctuations of the flame. In IDEA the tomographic reconstruction out of the 18 projections was performed for the following 3D graphics, again with the software Matlab.

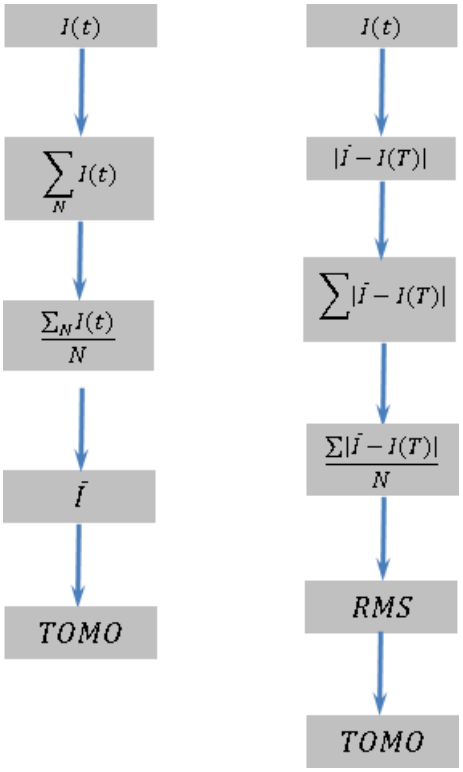

Figure 5.24: Evaluation of the raw frames to average value (left path) and RMS average (right path)

A resulting example is shown in Fig. 5.25. For further details see [3].

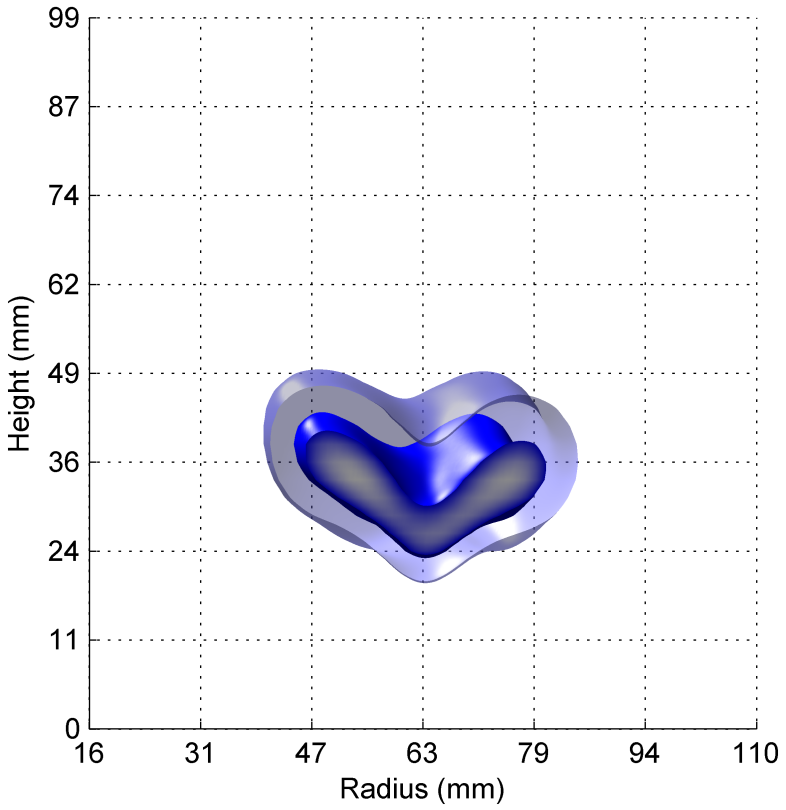

Figure 5.25: 3d isosurfaces of light intensity [3]

5.4 Particle image velocity

5.4.1 Fundamentals of particle image velocity

Particle Image velocity (PIV) is an optical measurement technique to detect the velocity field of a fluid flow. Small particles, called seeding particles, usually with a size of 1 to 5 μm are injected, following the flow. In an isothermal air flow oil particles are added. Non flammable metallic particles, like TiO_2 or Al_2O_3 are generally used for the velocity detection in a flame zone. In case of water flow the use of polyamide is common. These seeding particles are illuminated twice by consecutive pulses of a laser within a short time interval. The scattered light of the seeding particles is recorded by a camera with a CCD sensor, adjusted normal to the light plane, laser sheet (Fig. 5.27), and saved in two separate frames (Fig. 5.26). For the evaluation of the measurement data the saved images are sub-divided into smaller areas (interrogation areas), which are partially overlapping (mostly 50%). The PIV Software uses a cross correlation algorithm to obtain a local shift vector, indicating the flow direction, for each interrogation area. With the geometric scaling factor (camera image) and the time distance Δt the current velocity of the seeding

particle can be determined. The result is a velocity vector field for the inspected flow area [33].

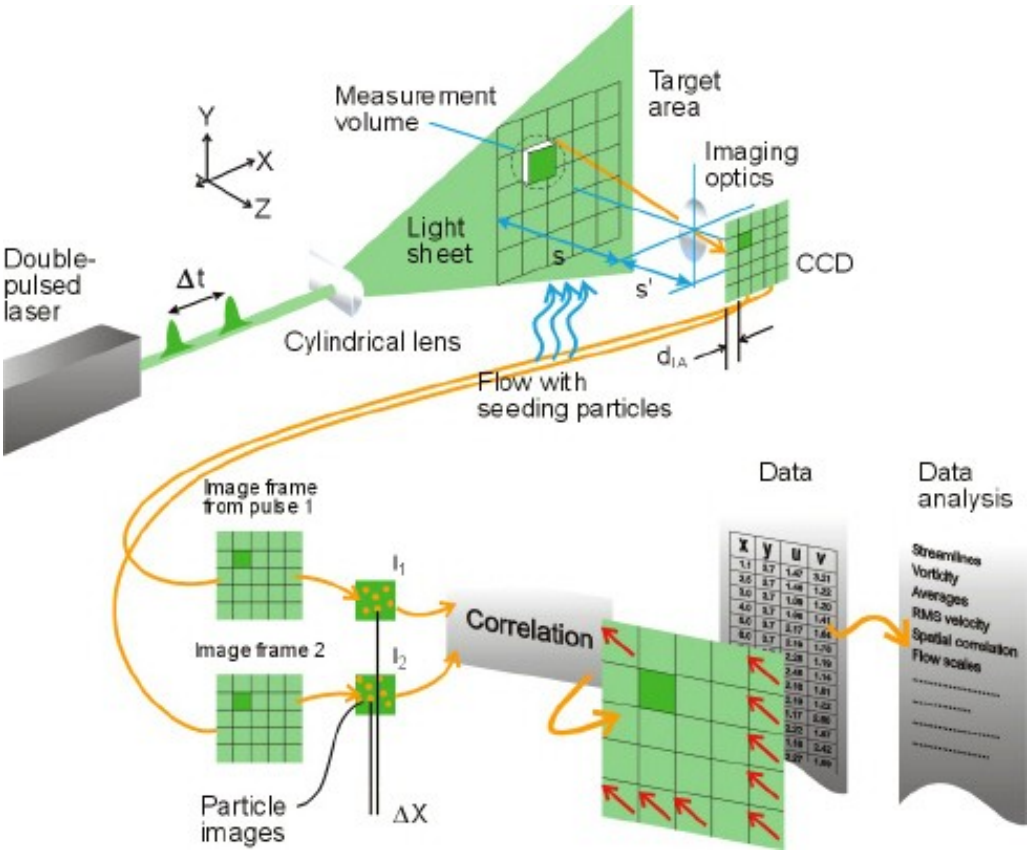

Figure 5.26: Layout for PIV measurement [34]

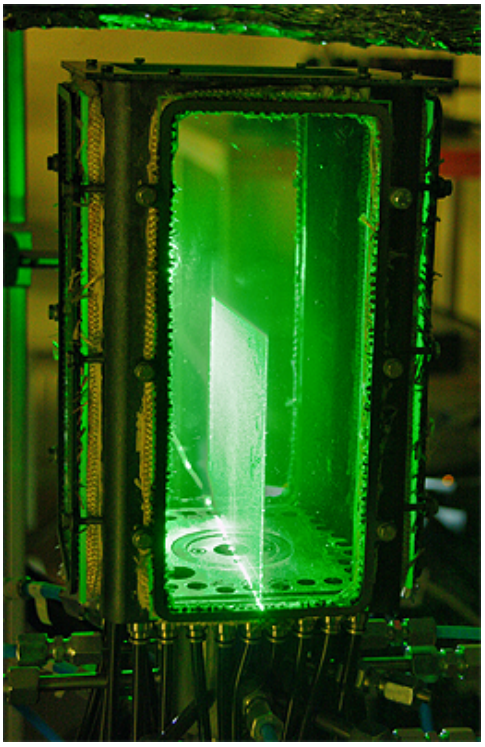

Figure 5.27: PIV laser sheet [3]

By extending the PIV measurement setup with a second PIV camera the determination of a three components (3C) velocity vector field can be achieved. The stereoscopic PIV is based on the same fundamental principle as human eye-sight. By recording two pictures with different perspective, a spatial interpretation is possible. Thereby, next to the in plane component also the out of plane component is detected with the stereoscopic PIV measurement (Fig. 5.28). Combining the resulting pair of 2-dimensional displacements $(\Delta x, \Delta y)$ with a calibrating polynomial (references obtained with a calibrating target positioned in different distances on the lightplane) the three true displacements $(\Delta X, \Delta Y, \Delta Z)$ are derived. The Scheimpflug condition has to be considered in mounting the PIV cameras. The Scheimpflug condition postulates that the object plane, the plane of the imaging lens and the image plane (CCD-plane) have to intersect in a common line for realizing a complete focus in the image plane for all off-axis camera angles [35]. The Scheimpflug condition is shown in Fig. 5.29.

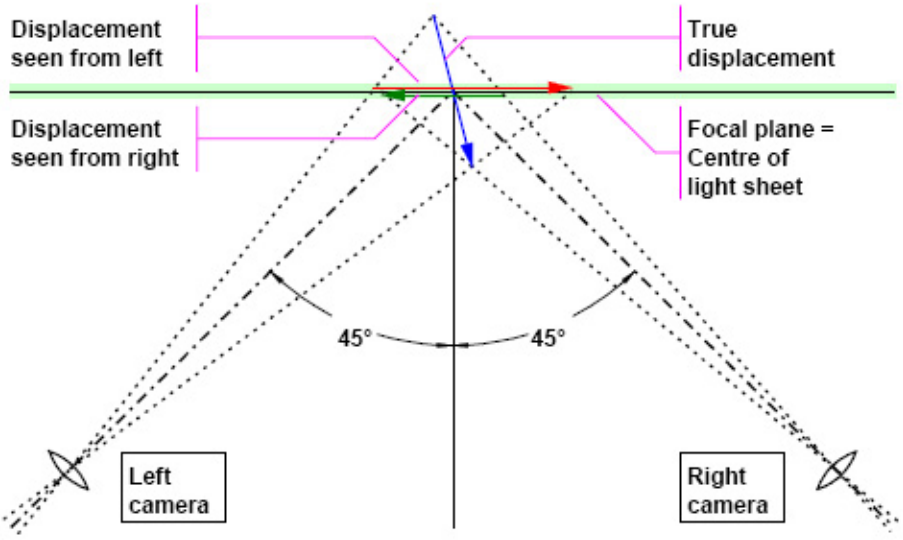

Figure 5.28: Fundamental of stereo PIV [35]

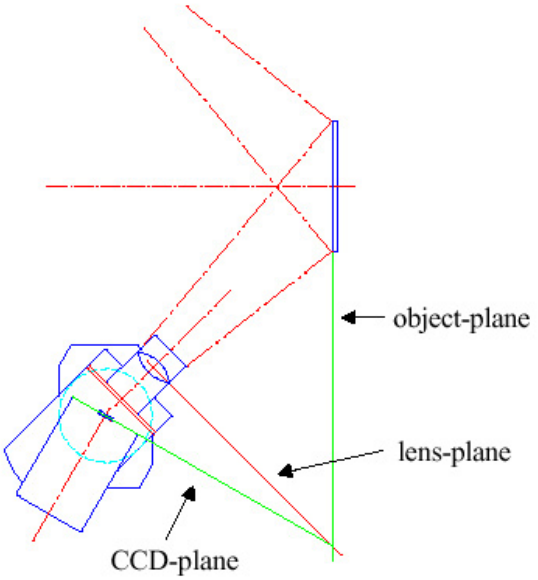

Figure 5.29: Scheimpflug condition for the PIV camera [35]

5.4.2 Setup for particle image velocity

As a light source a Nd:YAG laser(New Wave GEMINI, Sunnyvale, California) was employed. The light pulses, with a pulse duration from 3 to 5ns, a maximum repetition rate of 15 Hz, had a maximal energy of 120 mJ/pulse and a wavelength of 532 nm (green light). The time between the two laser pulses could be adjusted manually. A flexibel arm was connected to the optical head, including a cylindrical lens (focal length of 600 mm) arranged for generation of the light sheet (width of about 2 mm). For recording a DANTEC 80C60 HiSense camera with a Micro-NIKKOR

60/2.8 objective was employed. For the PIV visualization a camera from Canon type Toscana EOS 450D with a lens type Sigma DC was employed.

The data acquisition and the synchronization of laser and camera is controlled by the PIV processor (DANTEC FlowMap1500). The PIV processor is Connected via 100 MBit cable to the measurement Computer (DANTEC Flow Manager 4.60.28).

For the qualitative visualization and for the 2D PIV measurements Di-Ethyl-Hexyl-Sebacat (DEHS) was employed as seeding. An aerosolgenerator (Fig. 5.30) injects the seeding particles into the axial air flow before the entry of the burner (Fig. 4.2) for best distribution and coherence with the flow [36]. Furthermore, for the 3C PIV measurement the flame resistant TiO_2 (Data sheet of TiO2 on CD)was applied in the seeding generator type PivSolid 3 from PIVTEC (Fig. 5.31). The seeding generator is equipped with a regulator, pressure scales, a saftey valve and also a throttling valve for adjustment of the outlet pressure (optimal: half of the inlet pressure). The optimized mixing in the fluid bed of seeding and air is achieved in the range from 1,27 l to 0,6 l of seeding [37]. The seeding generator can operate in two modes: bypass and operation (Fig. 5.32).

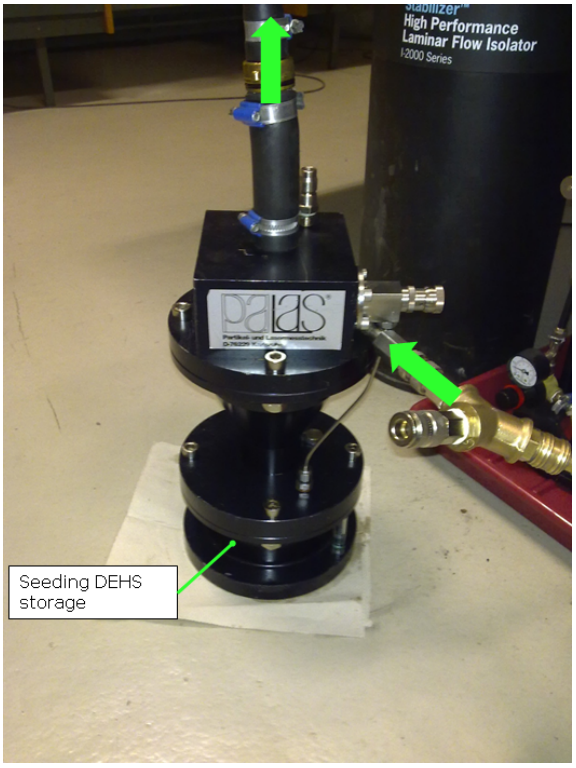

Figure 5.30: Seeding generator for DEHS from Palas [36] with flow directions indicated (green arrow)

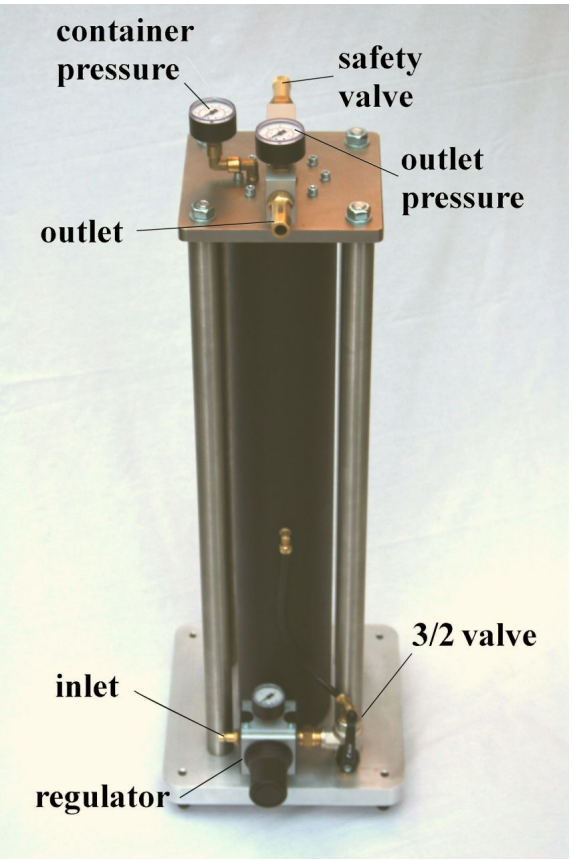

Figure 5.31: Seeding generator PivSolid 3 from PIVTEC for solid seeding particles [37]

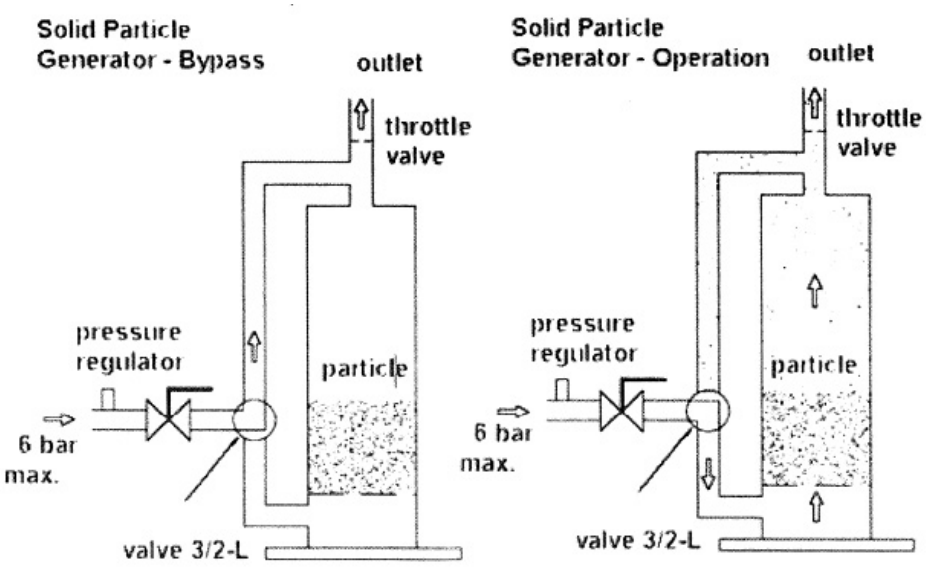

Figure 5.32: The two operation modes (bypass mode on the left side and operation mode on the right side) of the seeding generator PivSolid 3 from PIVTEC [37]

For the flow visualization a new modified baseplate (Fig. 5.33) was adjusted to the burner. The new baseplate provides 8 entry slots, arranged symmetrically to the z-axis (laser sheet) for a flow visualization of the full measurement field effected by providing seeding particles to the whole burner combustion zone including the surrounding area of the flame. The required air was supplied by the cooling air feed. Through a provided annular gap, between the baseplate and the injection zone of the burner the supported air reaches the combustion zone including the surrounding area. DEHS was employed for seeding in order to distinguish the inert zone from the flame zone (particles burnt).

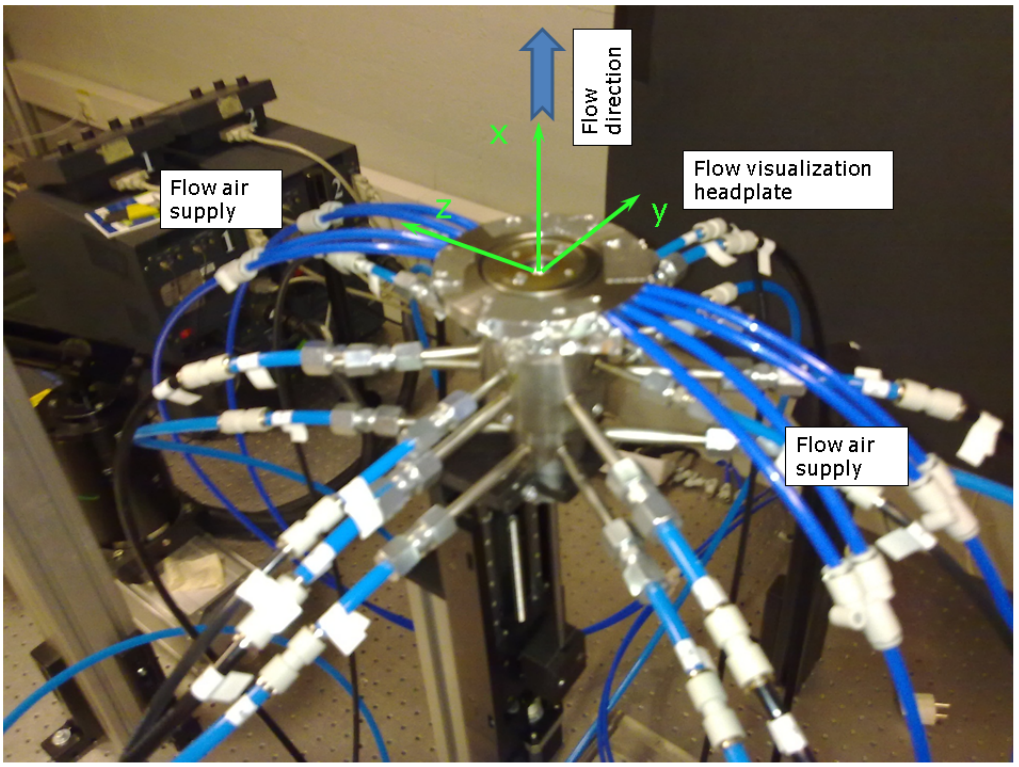

Figure 5.33: Modified headplate for flow visualization with 2D PIV

To obtain the calibrating polynomial a calibration target (Fig. 5.34) was required, consisting of black dots printed on white background in fixed distances. The calibration target, with a dimension of 100x100 mm, had a zero marker in the middle of the target representing the origin and 4 axis markers for the determination of the axis (Fig. 5.34).

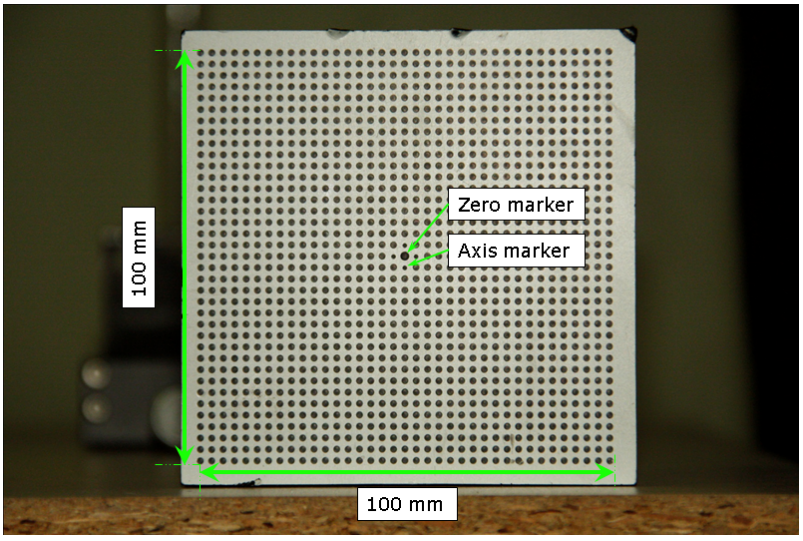

Figure 5.34: Calibration target for the PIV measurement

The calibration target must be aligned with the light sheet and positioned in the center of the burner and thereby the center of the flow field for the 2D PIV measurement. For the 3C PIV measurement two more additional reference positions were recorded for the determination of the out of plane component. A maximum overlapping view of the flow field is desired, since the overlapping field defines the measurement field. Beside the position of the calibration target in the center of the burner, reference recordings are performed also in the position +0.75 mm and -0.75 mm in y direction (Fig. 4.2). Records were taken in the single frame mode and the PIV cameras set to a exposure time of 100000 μs. Focussing on the calibration target was necessary for the dots on the target for the detection with the PIV software. A histogram, showing the two significant peaks from the signal representing dark and white pixel values. Hence, for each camera a separate calibration polynomial is calculated, applicable as a reference for the evaluation.

A vane anemometer determined the range of velocity of axial and tangential air flow with a value of about 15 m/s, a reference value for the setting of the time between bursts. For all measurements the time between bursts was set to 75 ns. A correct setting of this time period is demanded else a loss of pairs is the consequence. A loss of pair means the velocity of the fluids is to large for detection in the required interrogation area. The attenuation of the Nd:Yag laser was set to a value 960. The attenuator for the Nd:Yag laser output power is continuously adjustable from 0, the laser beam has a minimum of intensity, to 1000 for maximum intensity. The laser was controlled externally with the software of DANTEC from the measurement PC.

To minimize the measurement uncertainties of the turbulent flame 1200 frames were recorded, with the double frame mode for each operation point. 50 frames for detecting the light intensity of the flame (attenuation was set to zero) were recorded for subtracting the intensity of the flame from the background of the recorded frames in the evaluation.

A schematic of the test rig layouts for 2D PIV measurements is shown in Fig. 5.35 and for 3C PIV measurements in Fig. 5.36.

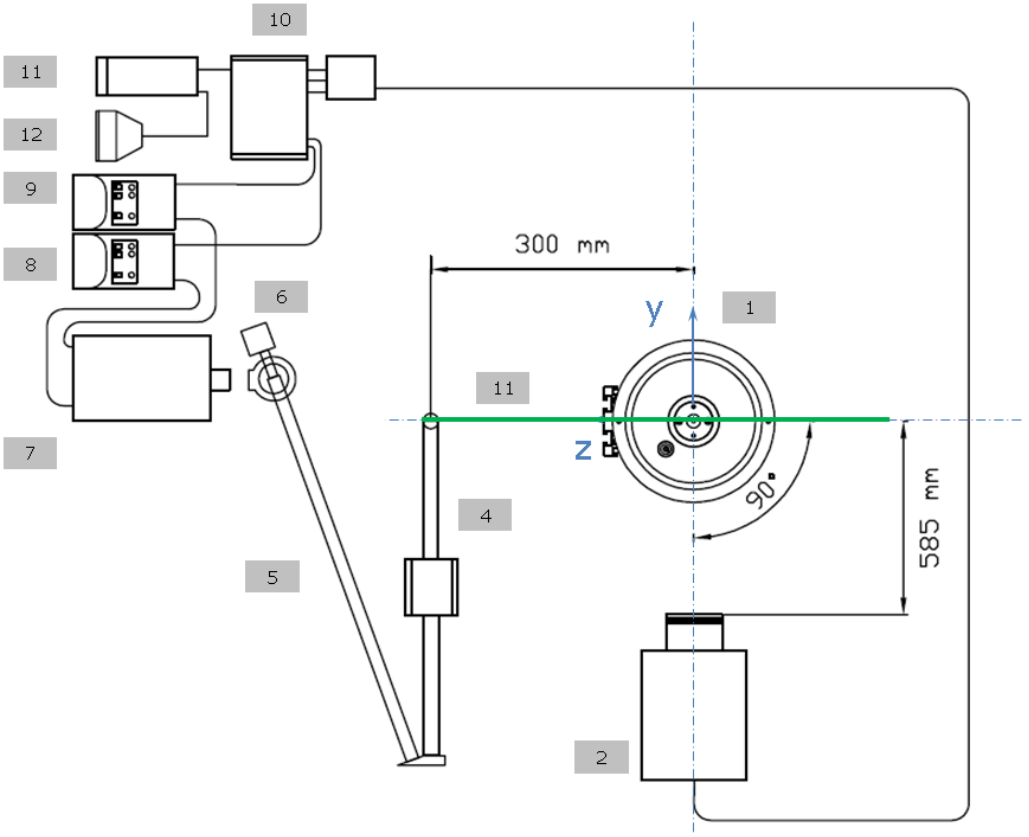

Figure 5.35: Layout for 2D-PIV measurements (bird's eye view)

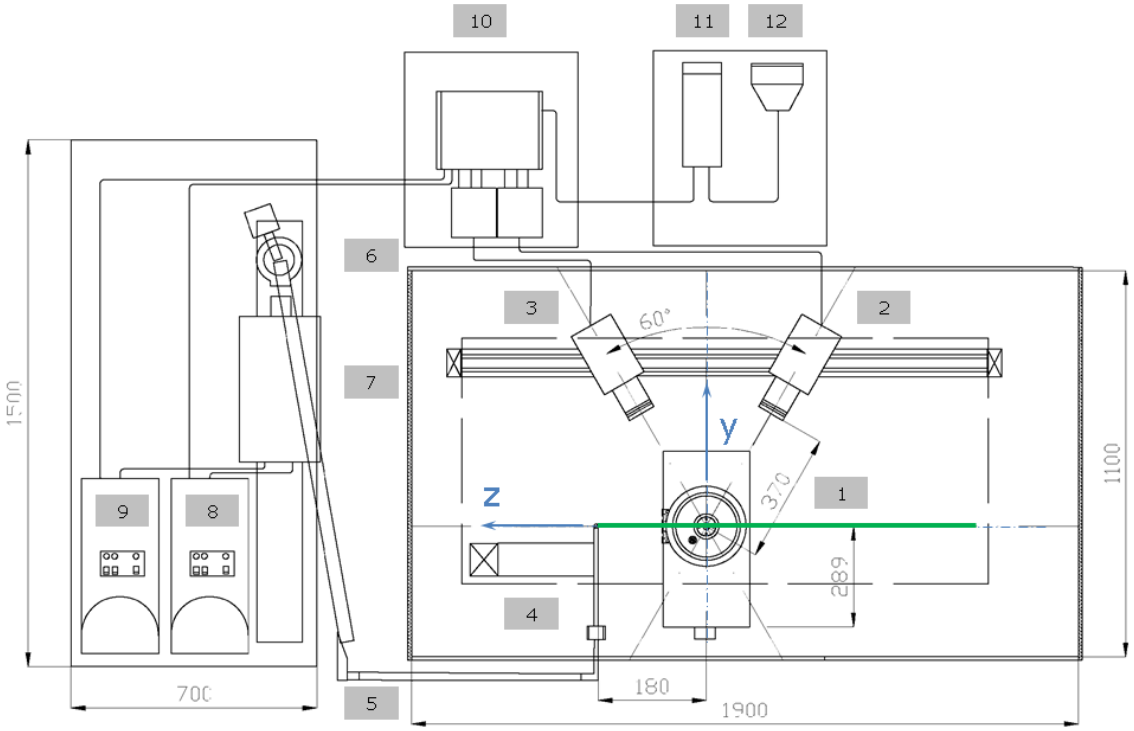

Figure 5.36: Layout for 3C-PIV measurements (bird's eye view)

Table 5.9: Component description of PIV system

Pos.	Description
1	burner
2-3	PIV camera
4	optical head
5	flexible arm
6	base mount
7	Nd:YAG laser
8-9	power supply
10	PIV processor
11	computer
12	monitor

The 3C PIV measurements with the solid seeding $Ti0_2$ were performed outdoor. Therefore the test rig had to be mobile providing a flexible arrangement and safety regulations were considered. The test rig was divided into several mobile test rig platforms to allow an optimal arrangement (Fig. 5.37). The components of the

3C PIV measurement test rig were the mobile test rig VGB, the mobile test rig PIV laser, the mobile test rig VGB control and the mobile test rig PIV control. The variable geometry burner was mounted on the mobile test rig VGB, including the PIV cameras and the optical head with the corresponding assembly platform (Fig. 5.38). The mobile test rig VGB was enclosed with removable sidewalls to provide isolation from environmental influence such as wind. The sidewalls were removable to allow an adjustment of the test rig components. The exhaust pipe was mounted in coaxial position above the variable geometry burner on the top of the mobile test rig VGB for stability and alignment of the flame. At the end of the exhaust a ventilator was put for an optimal exhaust of the emission including the seeding particles.

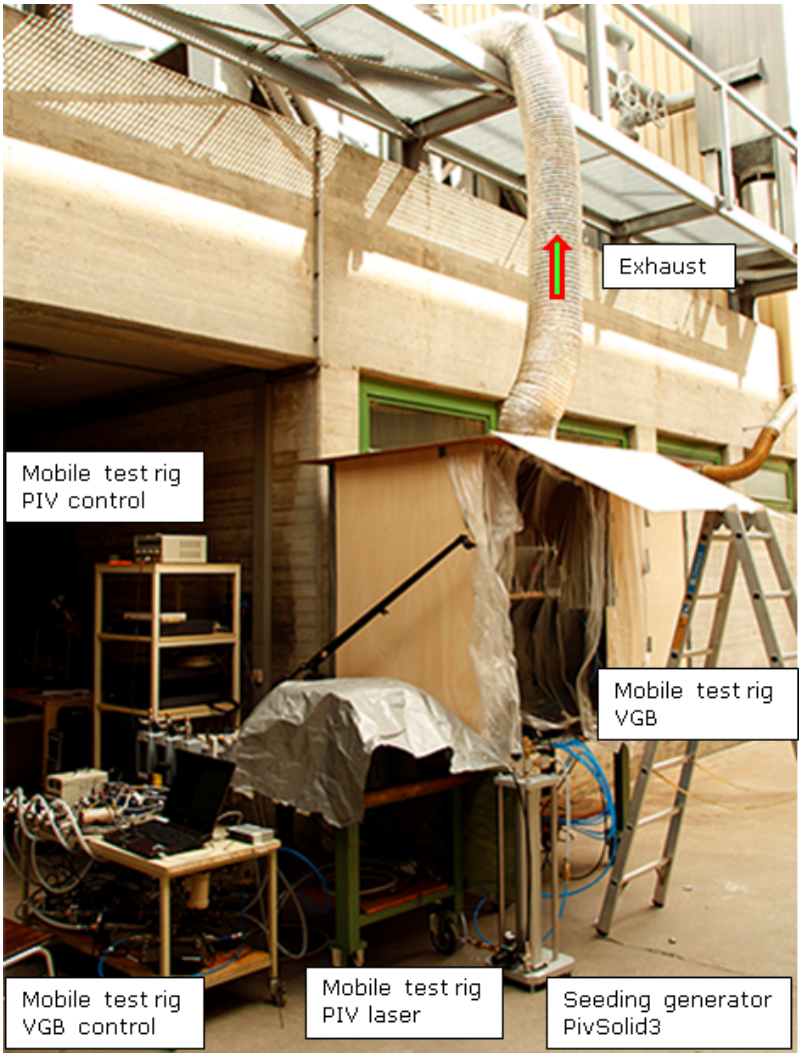

Figure 5.37: Assembly of the outdoor 3C PIV measurement with the mobile test rig components

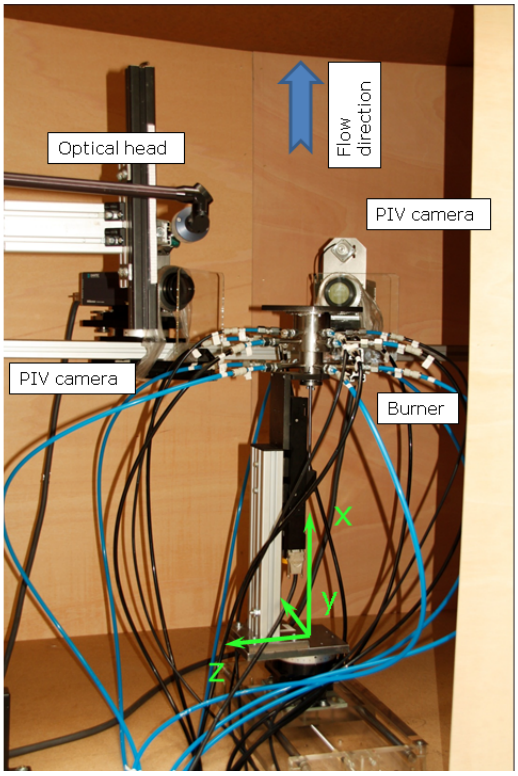

Figure 5.38: Assembly of the Mobile test rig VGB with the PIV cameras, optical head and the burner for the 3C-PIV measurement

Some variants of the test assembly were realized in scope of the PIV measurements. Fig. 5.39 shows the test assembly including fuel and air supply for 2D PIV measurements for the flow visualization with DEHS as seeding. The measurements were performed under unconfined conditions. For the quantitative 2D PIV measurement the cooling air supply was not necessary. Tab. 5.10 shows the components of the test rig for these measurements.

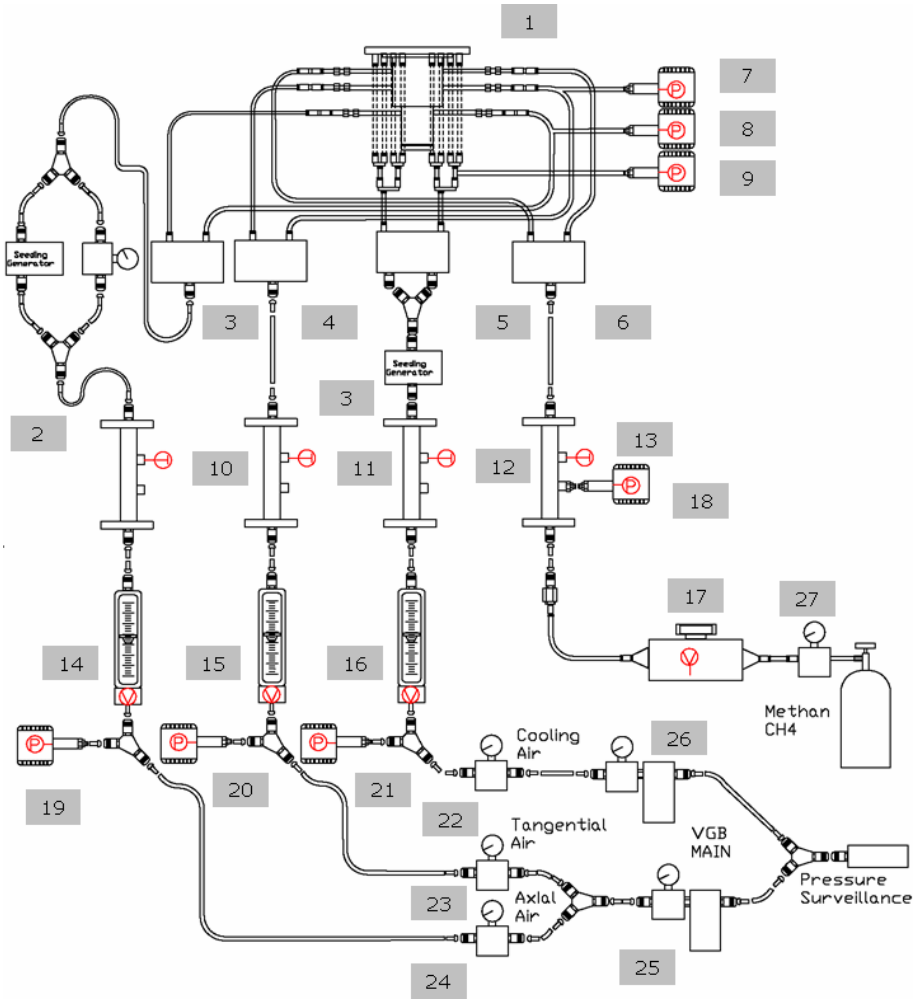

Figure 5.39: Test assembly with instrumentation for 2D PIV measurements for flow visualization with DEHS as seeding

Table 5.10: Component description of the test rig for 2D PIV measurements for flow visualization with DEHS as seeding

Pos.	Description
1	burner
2	seeding generator [36]
3-6	distribution boxes
7-9	pressure transducers
10-13	temperature sensors
14-16	air mass flow meters
17	fuel mass flow meter
18-21	pressure transducers
22-26	control valves main air
27	control valve fuel

Fig. 5.23 shows the test assembly for 3C PIV measurements with TiO_2 as seeding. The measurements were performed under unconfined conditions. Tab. 5.11 shows the components of the test rig including fuel and air supply for 3C PIV measurements with TiO_2.

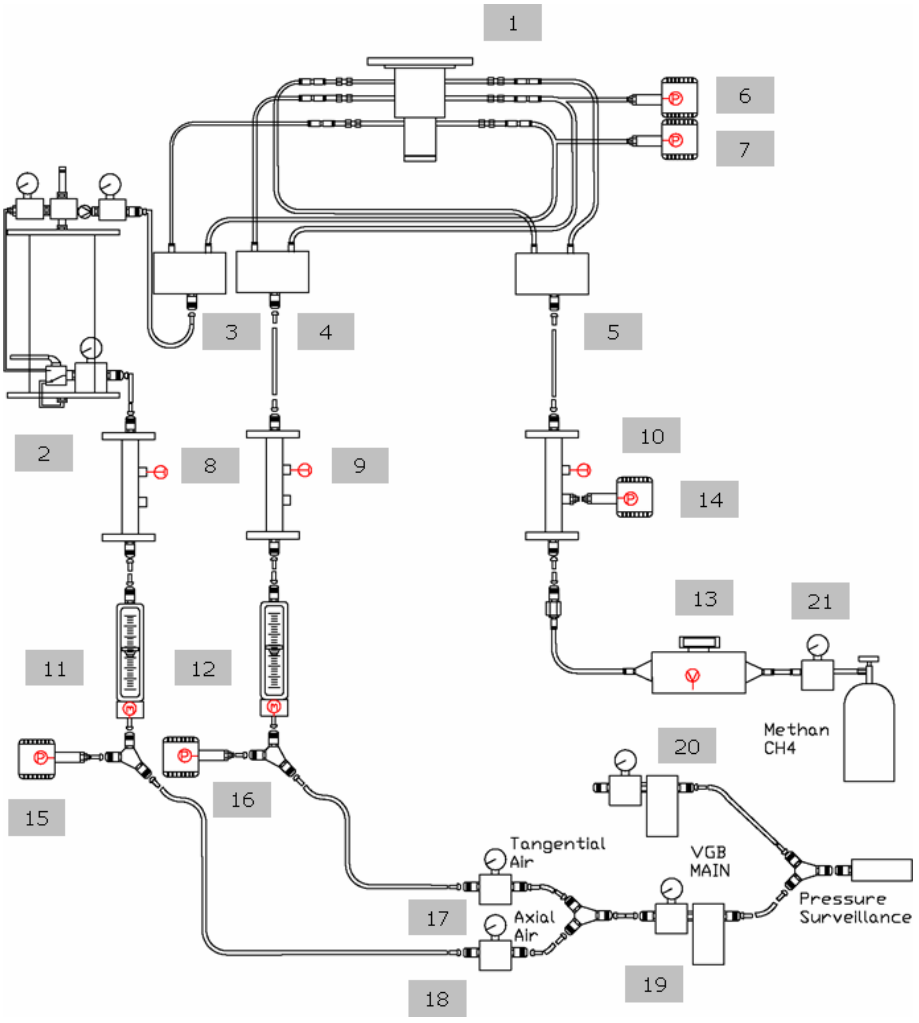

Figure 5.40: Test assembly with instrumentation for 3C PIV measurements with TiO_2 as seeding

Table 5.11: Component description of the test rig for 3C PIV measurements with TiO_2 as seeding

Pos.	Description
1	burner
2	seeding generator PIVTEC
3-5	distribution boxes
6-7	pressure transducers
8-10	temperature sensors
11-12	air mass flow meters
13	fuel mass flow meter
14-16	pressure transducers
17-20	control valves main air
21	control valve fuel

5.4.3 Measurement evaluation of particle image velocity

An overview of the implemented steps to detect the velocity vectors is shown in Fig. 5.41. The evaluation was performed with the software FlowManager 4.60.28. A mean value for the 50 frames showing the intensity of the flame was calculated and subtracted from each frame for the PIV measurement, to delete the non relevant intensity of the flame. A cross correlation with the value of 64x64 Pixel recorded vectors for each interrogation area out of the recorded images was calculated by a fast Fourier transformation (FFT)Algorithm [35]. Failure vectors (for example due to a field with low presence of seeding) were eliminated by validation criteria. The peak validation with a height ratio set to 1.2 for the first two correlation peaks, eliminated non defined correlations. The range validation excluded physically non relevant vectors, outside meaningful velocity range. Moving average validation compared neighbor vectors by criteria of mean average and standard deviation. The vector exceeding the acceptance tolerance were eliminated.

A resulting example is shown in Fig. 5.42 for flow visualization with 2D-PIV measurement and Fig. 5.43 for the detection of axial gas velocity obtained with 2D-PIV measurement. For further details see [3].

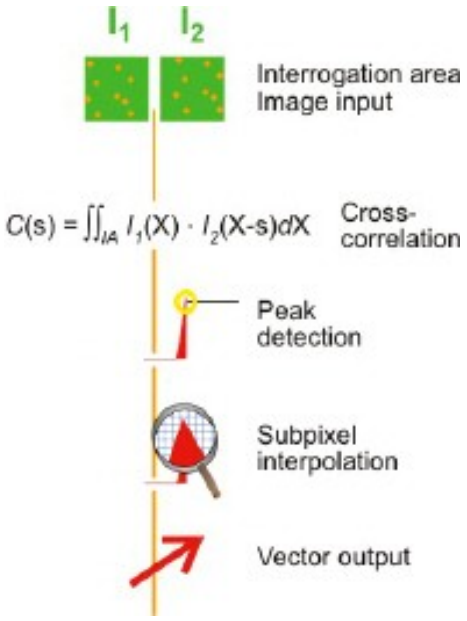

Figure 5.41: PIV Evaluation steps [35]

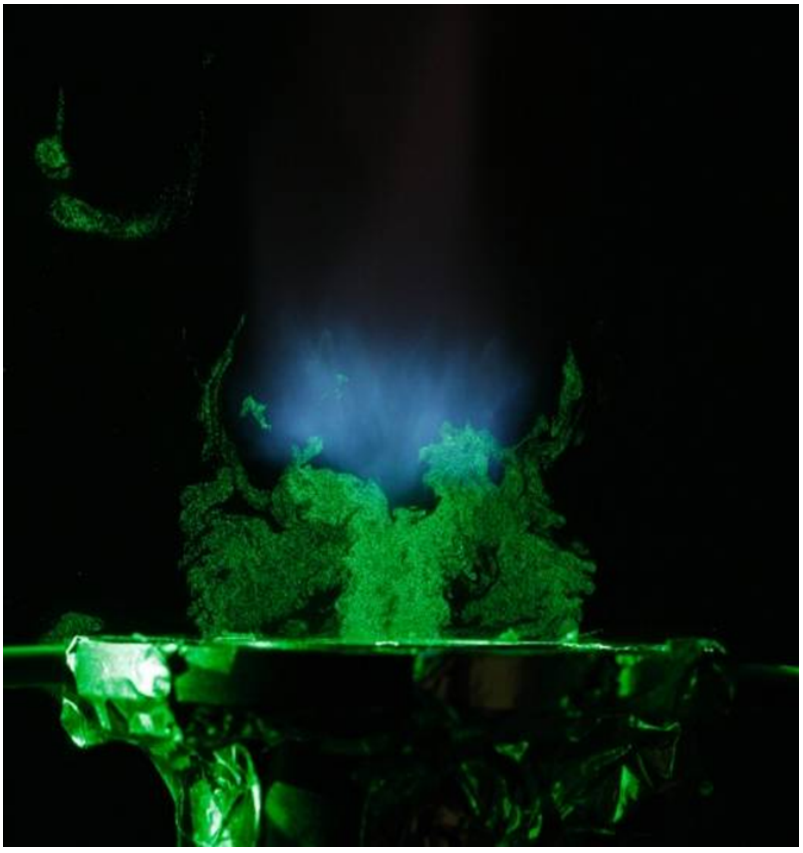

Figure 5.42: Visualization of the flame [3]

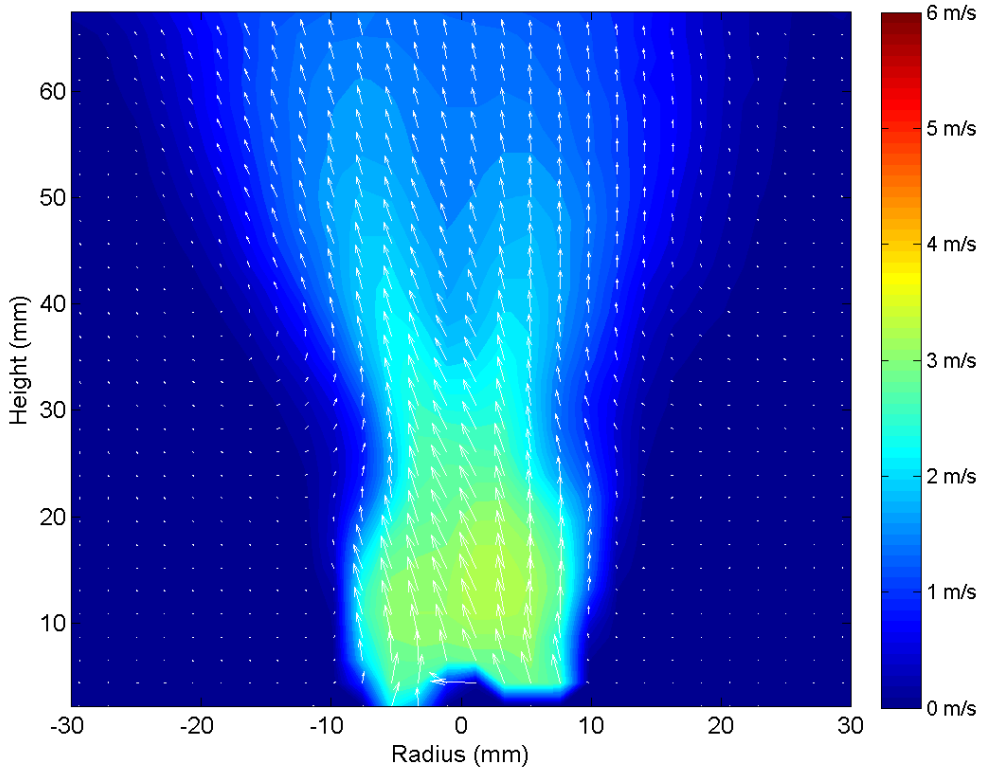

Figure 5.43: Axial gasvelocity measured with 2D-PIV [3]

Chapter 6

Summary

A modular burner test rig for a variable geometry burner was established for a 10 kW model burner with extensive investigations under atmospheric conditions. The test rig included the required operational environment for the burner with means for adjustment of the variable geometry parameters, optical measurement instrumentation for non-intrusive test arrangement as well as the necessary data acquisition and evaluation. For confined measurements a flame tube with optical inspection window was provided for the burner test characterization. The flame tube is furthermore prepared for the possible operation under elevated pressure which could be a next step in the investigation of the variable geometry burner. The modular test rig was provided with various non intrusive optical measurement techniques such as Schlieren visualization, which allows a qualitative analysis of flame characteristics, the differential interferometry for the detection of the density distribution and the particle image velocity (PIV) measurement for detecting the flow field in the flame zone. A tomographic reconstruction was performed of the recorded projections in order to obtain a reproduction of the flame in 3D representation to provide spatial measurement information. The data acquisition was additionally programmed in Labview 8.6 to ensure the operating conditions for the measurement points together with an adequate measurement storage. The instrumentation was described in detail. The software routines were programmed in a modular manner to provide adjustments for further applications.

Appendix A

Drawings of the flame tube

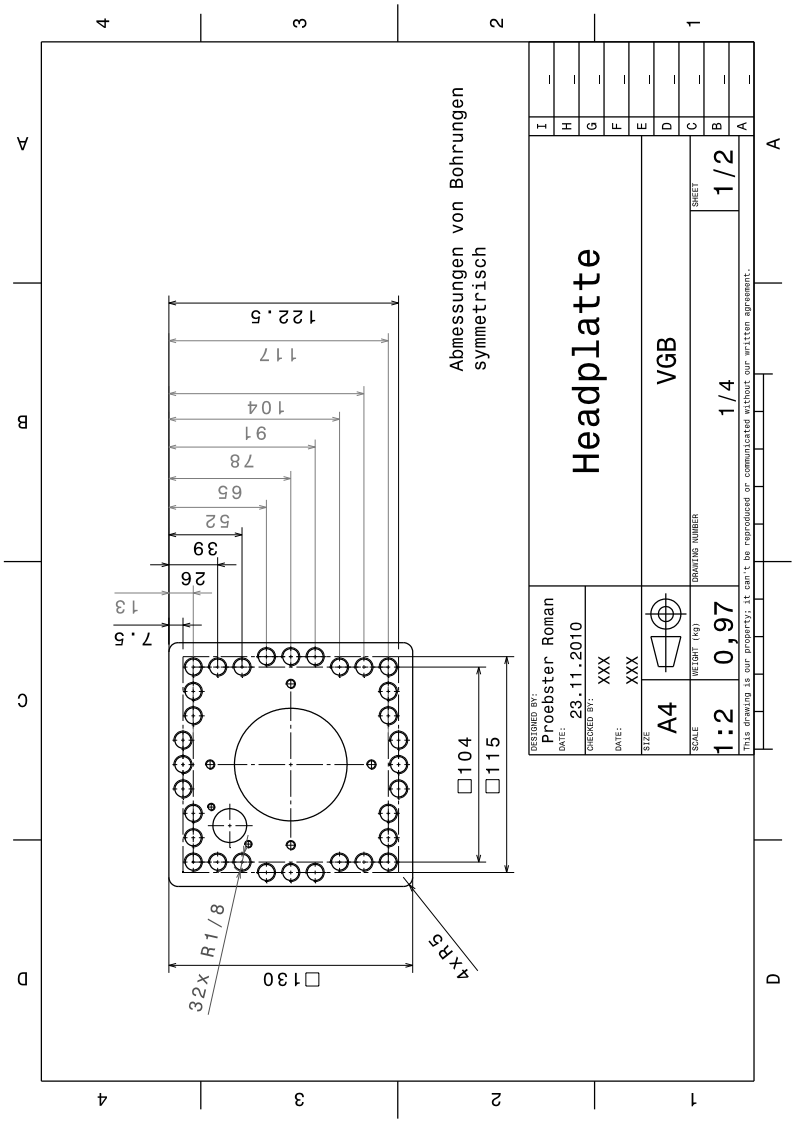

Figure A.1: Headplate 1/2

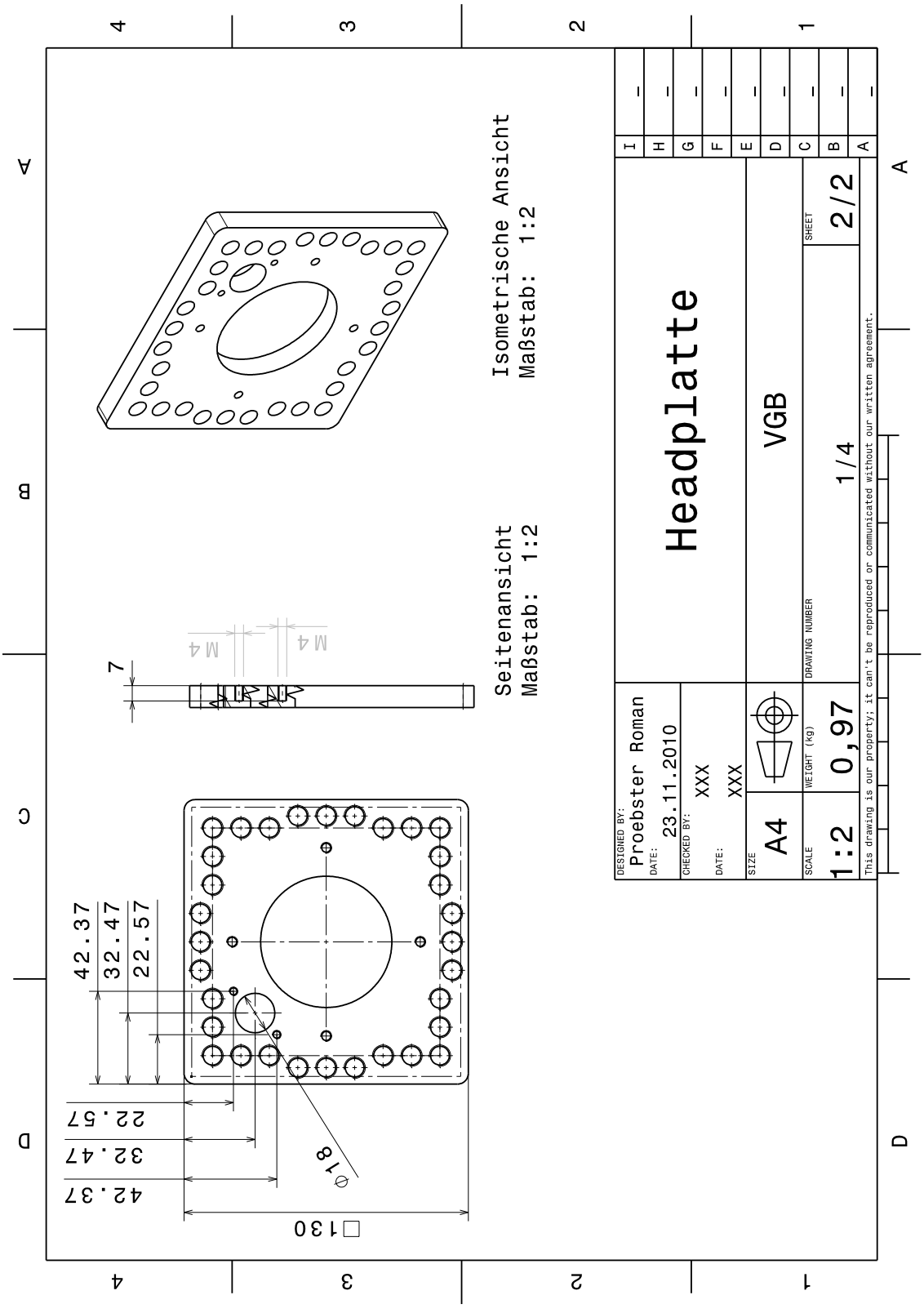

Figure A.2: Headplate 2/2

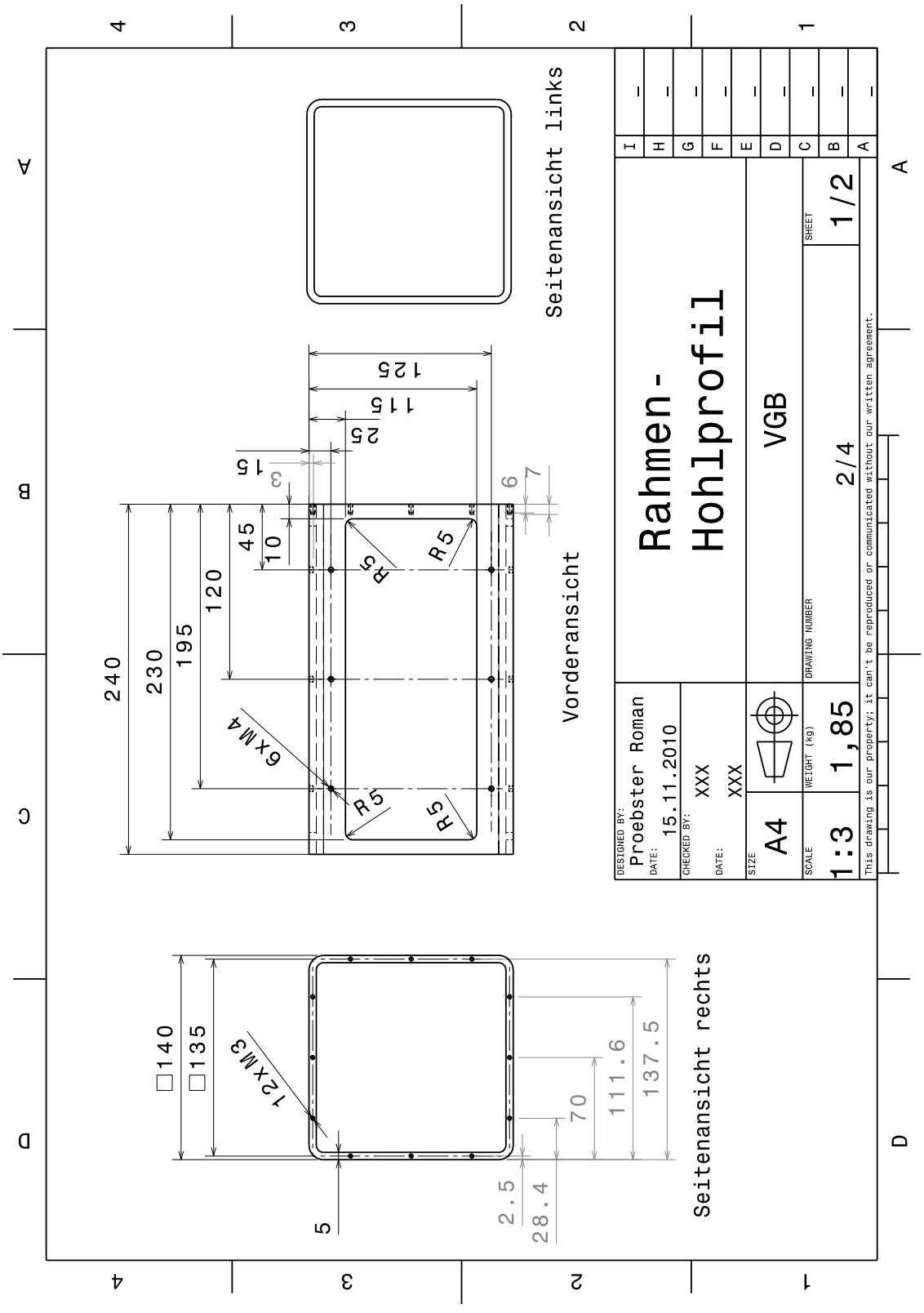

Figure A.3: Liner tube 1/2

Figure A.4: Liner tube 2/2

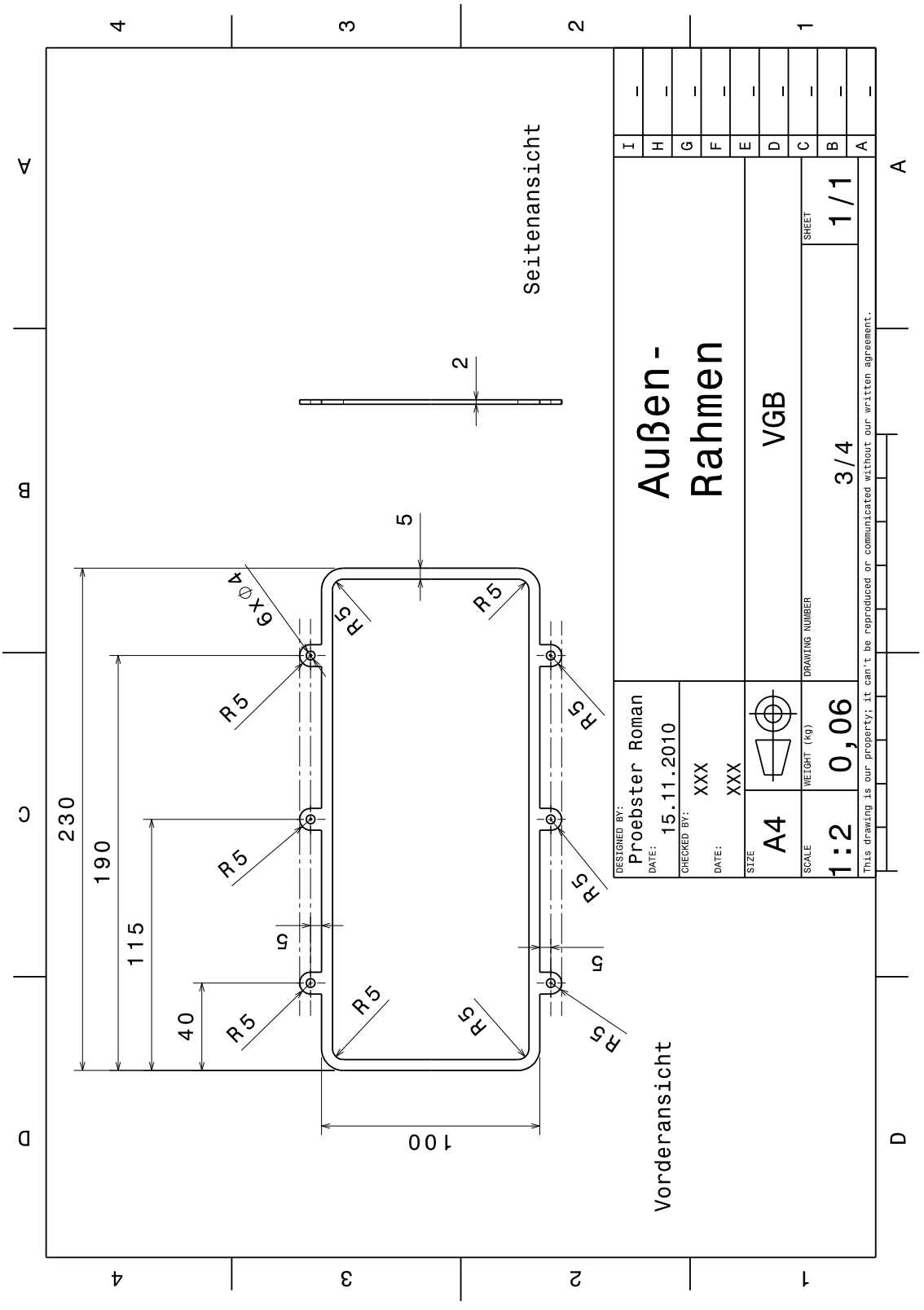

Figure A.5: Glas coverage

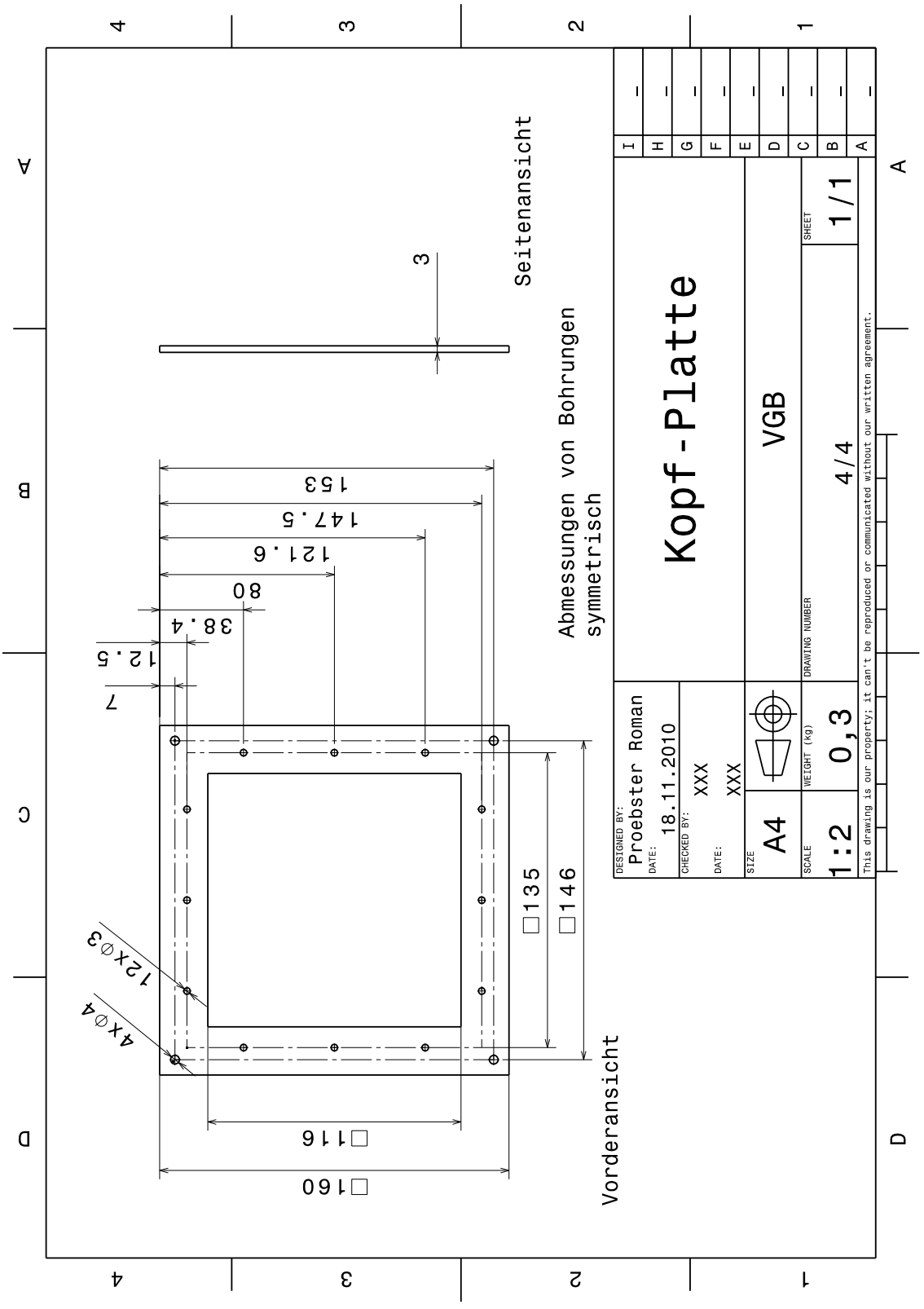

Figure A.6: Covering plate

Appendix B

Circuit layout of instrument interfaces

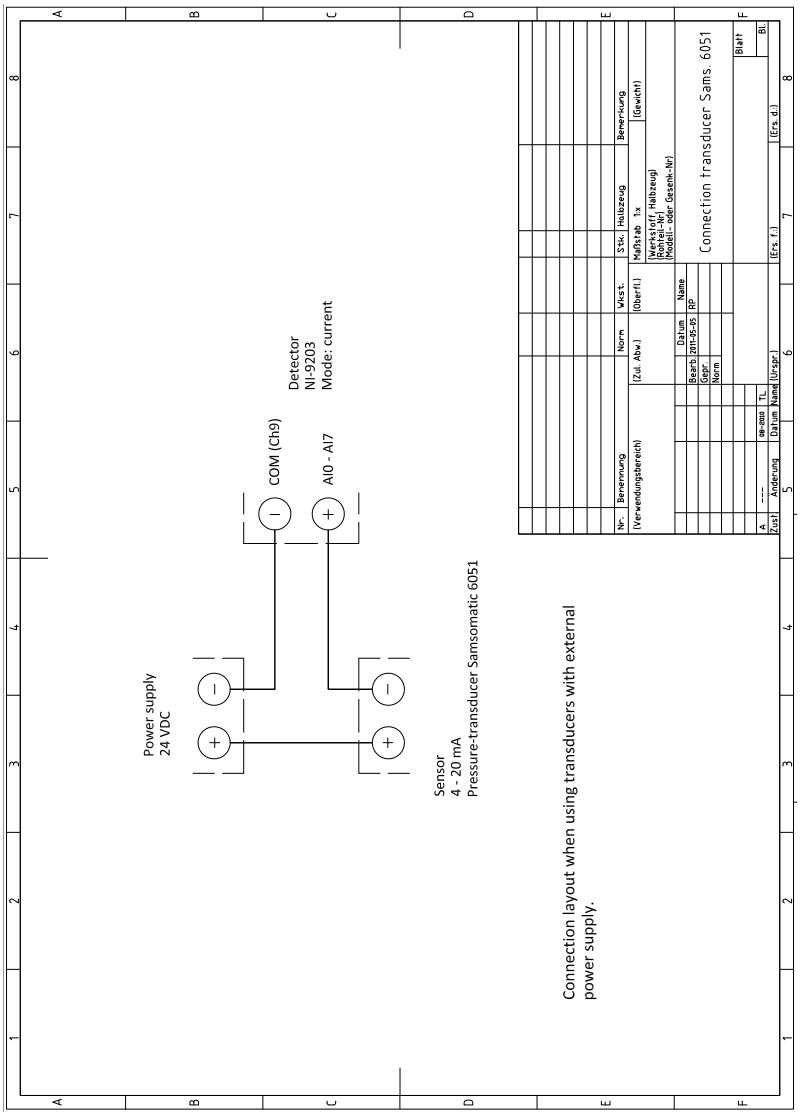

Figure B.1: Circuit layout connection of pressure transducer Samsonite 6051

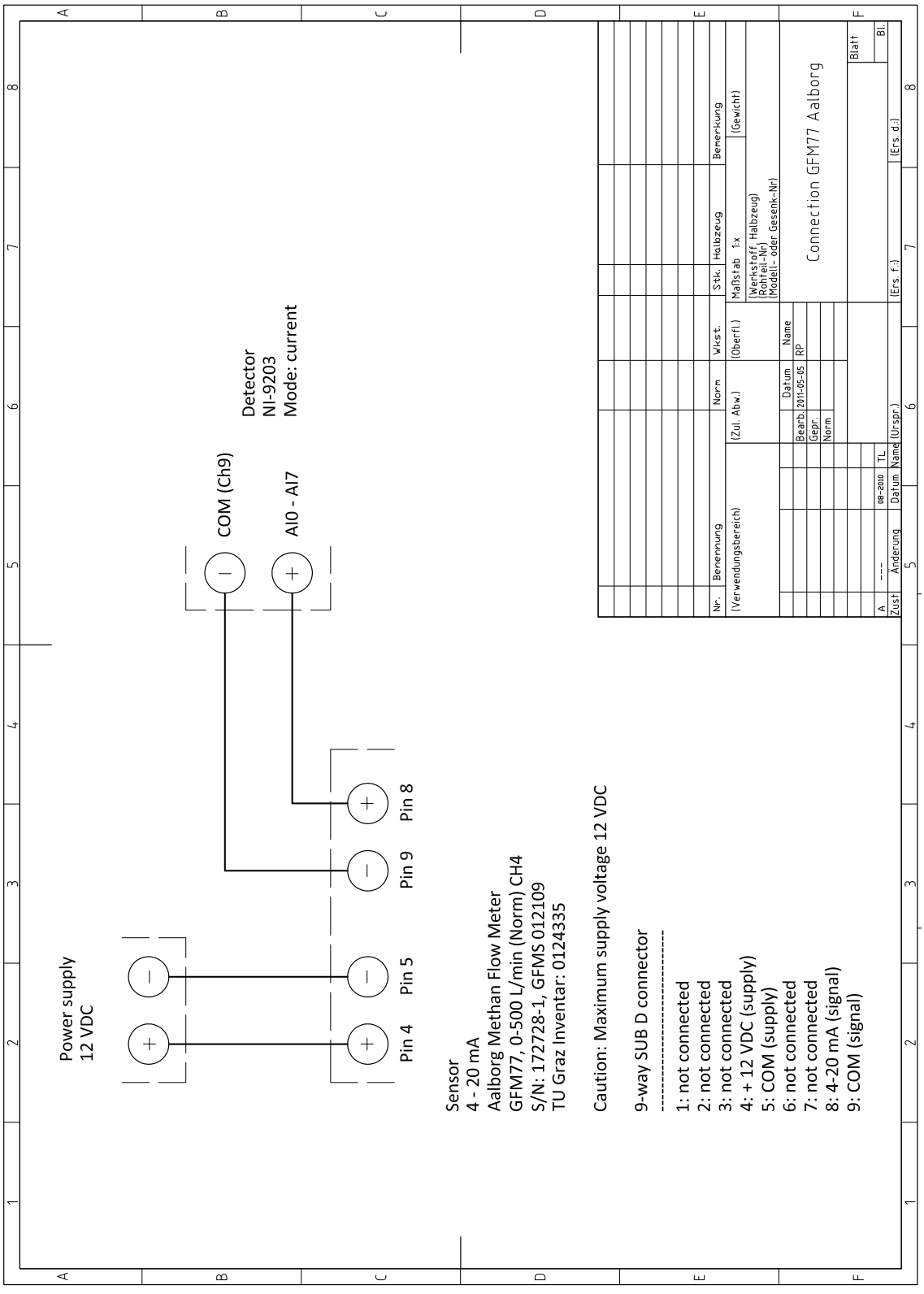

Figure B.2: Circuit layout connection of fuel mass flow meter GFM77 from Aalborg

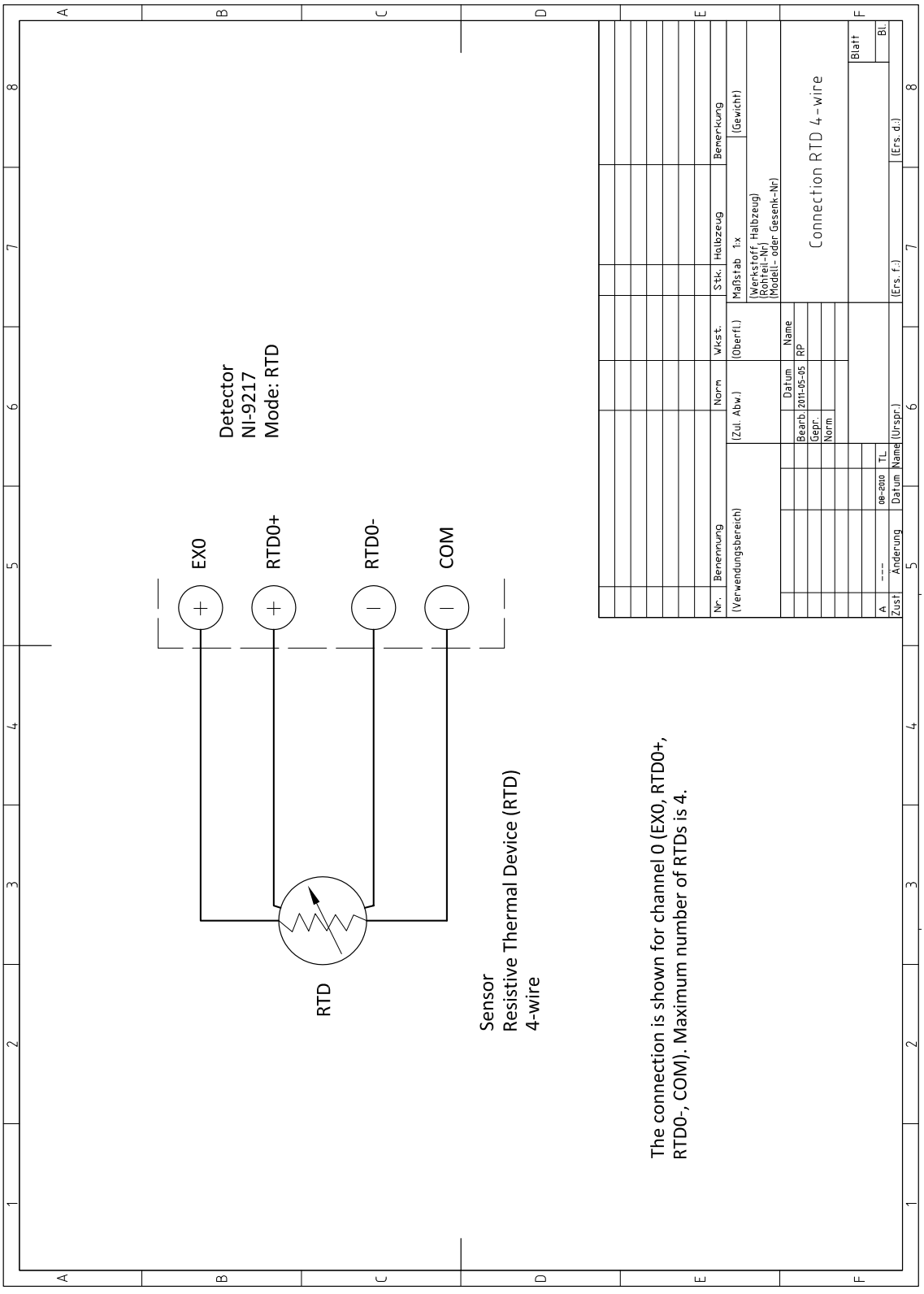

Figure B.3: Circuit layout connection of resistive thermal device (RTD) Pt100 4wire

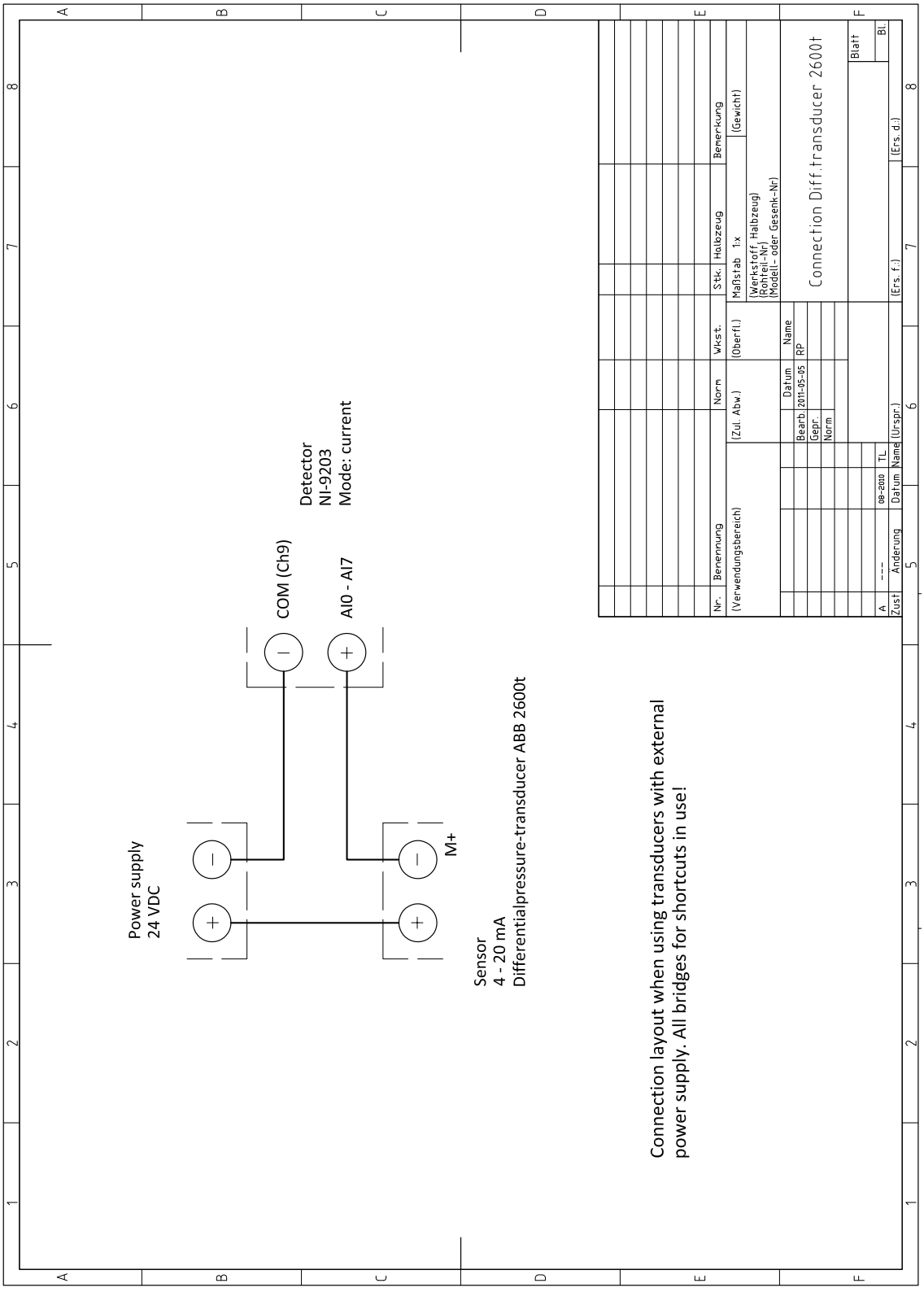

Figure B.4: Circuit layout connection of differential transducer 2600t

Appendix C

Data sheet of mass flow meter

UNIFLUX Schwebekörpermesser - Abmessungen und Montage

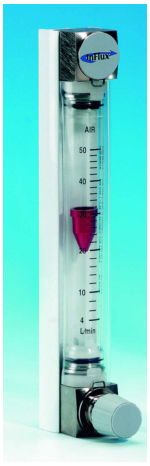

Ablesung:	Glas-Skale am oberen Rand des Schwebekegels
Lieferzustand:	kleine Durchsätze - komplett montiert betriebsbereit
Achtung:	schwere Kegel mit Transportsicherung !
	vor dem Einbau entfernen !
Tafelmontage:	mit 2 Stück M5- Gewindebolzen möglich
	max. Tafeldicke = 6 mm
max. Druck:	16 bar stossfrei
Temperatur:	-15 bis 120 C (Medium)
Werkstoffe:	Geräteträger: Messing vernickelt oder Edelstahl
	Messrohr: Borosilikatglas
	Messkegel: Edelstahl/Aluminium/Sonderwerkstoffe
	Dichtungen: Viton-O-Ring
Anschlüsse:	1/4" BSP Innengewinde
Messbereich:	Skalenwert bei eingeprägten Betriebsbedingungen
	z.B. L/min, N_2, 1 barg, 30 C
Filterfeinheit:	in Abhängigkeit der Messrohrgrösse Filter verwenden !

Bauform	Compact	Standard	Lang
a	133	210	250
b	108	184	226
c	65	121	121

Abmessungen in mm

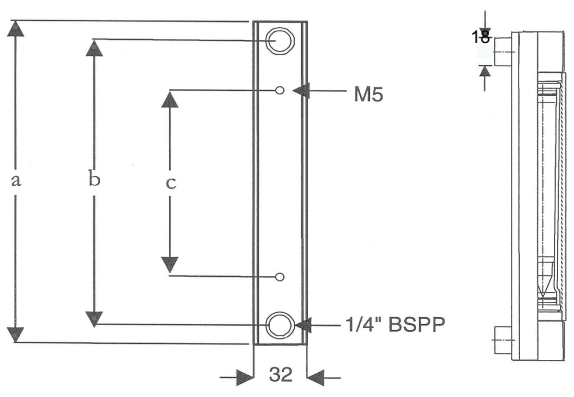

Figure C.1: Data sheet mass flow meter UNIFLUX

Appendix D

Characteristic curve of the video camera

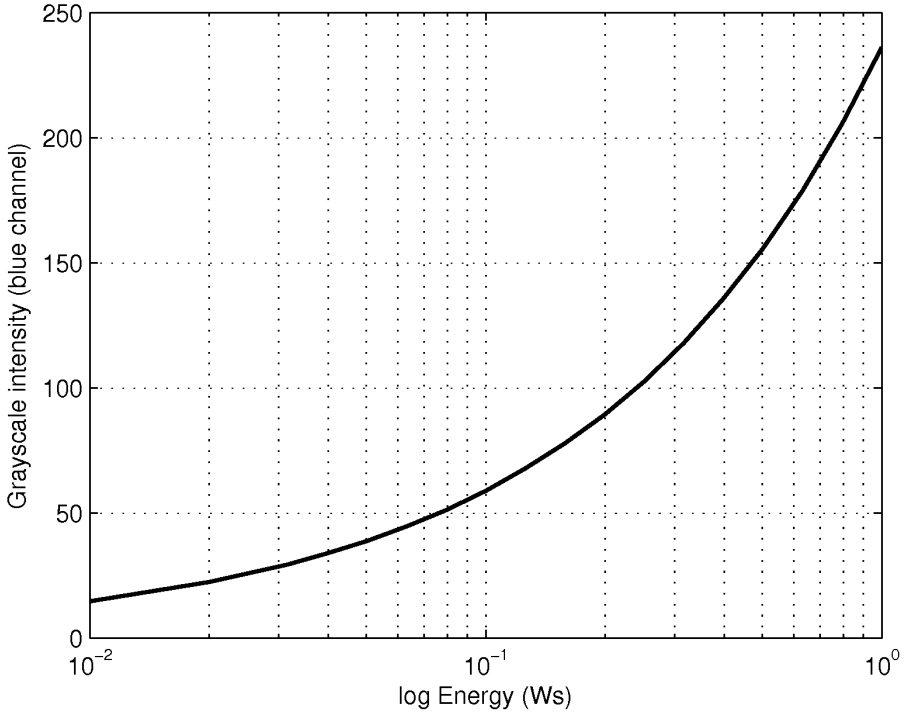

Figure D.1: Characteristic curve of the video camera [3]

List of Figures

List of Tables

Nomenclature

	Latin symbols	
$\dot{m}$	Mass flow rate	kg/s
$\dot{V}$	Volume mass flow rate	m^3/h
A	Cross section	m^2
c	Speed of light	m/s
C_xH_y	Hydrocarbons	
C_2^*	Carbon radical	
c_o	Speed of light	m/s
CH^*	Hydrocarbon radical	
CH_4	Methane	
CO	Carbon monoxide	
CO_2	Carbon dioxide	
H_2O	Hydro-Oxygen	
H_u	Lower heating value	MJ/kg
I	Laser intensity	$\frac{W}{m^2}$
$I_\lambda(T)$	specific spectral intensity	$\frac{W}{m^2 \mu m}$
n	refractive index	
NO_x	Nitrates	
O_2	Oxygen	
OH^*	Hydroxyl radical	
p	pressure	bar

R	Gas constant	$J/(kg \cdot K)$
$Ti0_2$	Titan-Dioxid	
w	Flow velocity	m/s
f	Focal length (mm)	
k	Gladstone Dale Coefficient	cm^3/g
L	Length	m
Ma	Machzahl	
S	Swirl Number	

Abbreviations

3C	Three component
A/A0	Area ratio
ACARE	Advisory council of aeronautic research in Europe
AFR	Air to fuel ratio (g/s_{air} / g/s_{fuel})
BOS	Background Oriented Schlieren method
CCD	Charge coupled device
D	Diameter (mm)
DC	Direct current
DEHS	Di-Ethyl-Hexyl-Sebacat
EP	European Patent Application
EU	European Union
FFT	Fast Fourier transformation
fps	frames per second
IDEA	Interferometrical data evaluation algorithms
LabVIEW	Laboratory Virtual Instrumentation Engineering Workbench
LCD	Liquid crystal display

LDI	Lean direct injection
LPP	Lean premixed prevaporized
Nd:YAG	Neodymium-doped yttrium aluminium garnet
NEWAC	New aero engine core concepts
NI	National Instruments
NPL	National Physical Laboratory
NTP	Normal temperature and pressure
OPR	Overall pressure ratio
PC	Personal computer
PERM	Partial evaporation and rapid mixing
PIV	Particle image velocity
ppm	Parts per million
RMS	Root mean square
S	Swirl Number
STP	Standard temperature and pressure
TOMO	Tomographic reconstruction
TTM	Institute for Thermal Turbomachinery and Machine Dynamics
US	United States
USB	Universal Serial Bus
VGB	Variable geometry burner
vi	virtual instruments

Greek symbols

Δ	Difference
η	Efficiency
κ	Adiabatic constant

λ	Wavelength	nm
ϕ	Equivalence ratio	
π	Pressure ratio	
ρ	Density	kg/m^3
φ	Stoichiometric ratio	

Subscripts

in	Inlet
max	Maximum
out	Outlet
ref	Reference
ax	Axial
cool	Cooling
cor	corrected
diff	differential
entry	entry burner
fuel	Fuel
red	Reduced
st	stoichiometric
tan	Tangential

Bibliography

[1] NEWAC. Media:NEWAC Overview . URL, http://www.newac.eu/uploads/media/NEWAC_Overview.pdf, 05 2011.

[2] NEWAC. Future innovative core configurations. URL, http://www.newac.eu/fileadmin/download_2010/19_Future_innovative_core_configurations.pdf, 05 2011.

[3] Thomas Leitgeb. *Validation of a Variable Geometry Burner Concept.* PhD thesis, Institute for Thermal Turbomachinery and Machine Dynamics at Graz University of Technology, Graz, 2011.

[4] Arthur H.Lefebvre. *Gas turbine combustion.* Taylor and Francis Group, New York, 2nd edition, 2006.

[5] Fabrice Giuliani. Gas turbine combustion, 2010. Skriptum zur Vorlesung aus Gas turbine combustion an der Technischen Universität Graz.

[6] Willy Bräunling. *Flugzeugtriebwerke.* Springer-Verlag, Berlin, Heidelberg, 2nd edition, 2001.

[7] CH Alstom. Brenner. DE 10050248A1, 10 2000.

[8] Dennis L.Overton. Variable geometry air-fuel injector. US 5664412, 09 1997.

[9] Maghon Hans. Premix burner for a gas turbine. EP 1524469A1, 04 2005.

[10] John M.Vaught. Variable-geometry air swirler. US 4044553, 08 1976.

[11] Arvin John R. Combustion apparatus with secondary air to vaporization chamber and concurrent variance of secondary air and dilution air in a reverse sense. US 3899881, 08 1975.

[12] Pillsbury Paul W. Combustion air control shutter. US 3490230, 01 1970.

[13] Jack Rogers Taylor. Variable-geometry air swirler. GB 2244551A, 12 1991.

[14] Bardey et al. Variable volume combustion chamber for a gas turbine. US 5211675, 5 1993.

[15] Air Liquide GmbH. Air Liquide's Gas Encyclopedia Methane. URL, http://alphagaz.airliquide.com/EuropeanCatalog/Products_Commercial/BE/LBE/PRODC_BE_LBE_Methane.pdf, 05 2011.

[16] OWIS. Position control PS 10). URL, http://www.owis-staufen.de/php/web8/pdf/pi_ps_10.pdf, 05 2011.

[17] SAMSOMATIC, GmbH. Pressure transducers. URL, http://www.samsomatic.de/pdf/t60510de.pdf, 03 2011. Kopie auf CD-ROM.

[18] Profos und Pfeifer. *Handbuch der industriellen Messtechnik*. R.Oldenburg Verlag München Wien 1994, München, 6nd edition, 1994.

[19] Aalborg Instruments and Controls, Inc. GFM Mass Flow Meters. URL, http://www.aalborg.com/images/file_to_download/en_Aalborg_EM201101_GFM.pdf, 03 2011. Kopie auf CD-ROM.

[20] McCrometer, Inc. V-Cone. URL, http://http://www.mccrometer.com/library/pdf/24517-16.pdf, 03 2011. Kopie auf CD-ROM.

[21] Dipl. Physiker Roland Kirchner. Die Berechnung von Korrekturfaktoren für Schwebekörperdurchflussmessgeräte bei geänderten Betriebsbedingungen, 05 2011. Kopie auf CD-ROM.

[22] National Instruments. NI-CompactDAQ-Chassis with 8 slots(NI cDAQ-9178). URL, http://sine.ni.com/nips/cds/view/p/lang/de/nid/207534, 05 2011.

[23] Franz Heitmeir. Thermische turbomaschinen grundlagen und vertiefung, 2010. Skriptum zur Vorlesung aus Thermische Turbomaschinen Grundlagen und Vertiefung an der Technischen Universität Graz.

[24] M. Dr.Klell. Höhere Thermodynamik, April 2010. Skriptum zur Vorlesung aus Höhere Thermodynamik an der Technischen Universität Graz.

[25] G.S. Settles. *Schlieren and Schadowgraph Techniques*. Springer-Verlag, New York, 1st edition, 2001.

[26] Heimel Martin. Untersuchung von Flammen und Flammenstabilitäten mittels optischer Messtechnik. Diplomarbeit am Institut für Thermische Turbomaschinen und Maschinendynamik, Technische Universität Graz.

[27] KeyandLaby by NPL National physical Laboratory. Refractive index of gases. URL, http://www.kayelaby.npl.co.uk/general_physics/2_5/2_5_7.html, 02 2011. Kopie auf CD-ROM.

[28] Woisetchläger J. Phillip H. Pretzler G. Fliesser W. Neger T. Hipp M., Reiterer P. Application of interferometric fringe evaluation spoftware at technical university graz. URL, http://www.optics.tugraz.at.

[29] Andreas Lang. *Unsteady Combustion Phenomena in Current and Future Aero Engines*. PhD thesis, Institute for Thermal Turbomachinery and Machine Dynamics at Graz University of Technology, Graz, 2011.

[30] Franz Joos. *Technische Verbrennung*. Springer-Verlag, Berlin, 1st edition, 2006.

[31] Herman, G.T. Image reconstruction from projections. Academic Press, 1980.

[32] Inat GmbH. Bluefilter Firm:Thorlabs Type:FGB25S. URL, http://www.thorlabs.de/NewGroupPage9.cfm?ObjectGroup_ID=3695&pn=FGB25, 01 2011. Kopie auf CD-ROM.

[33] Jürgen Kompenhans Markus Raffel, Christian E.Willert. *Particle Image Velocimetry*. Springer-Verlag, Berlin, 1st edition, 1998.

[34] Dantec Dynamics A/S. PIV layout. URL, http://www.dantecdynamics.com/Default.aspx?ID=1049, 05 2011. Kopie auf CD-ROM.

[35] Dantec Dynamics A/S. 3D-PIV Installation and User's guide, 02 2000. Kopie auf CD-ROM.

[36] Palas GmbH. Aerosolgenerator type AGF. URL, http://www.palas.de/de/product/agf, 05 2011.

[37] PIVTEC. Solid Particle Seeding Generators. URL, http://www.pivtec.com/solid_seed.html#solidspeed_specs, 05 2011.